ROG

A NEUTRON REFLECTOMETER AT IRI

V.-O. de Haan

Reflectometer voor oppervlakte- en grenslaagonderzoek

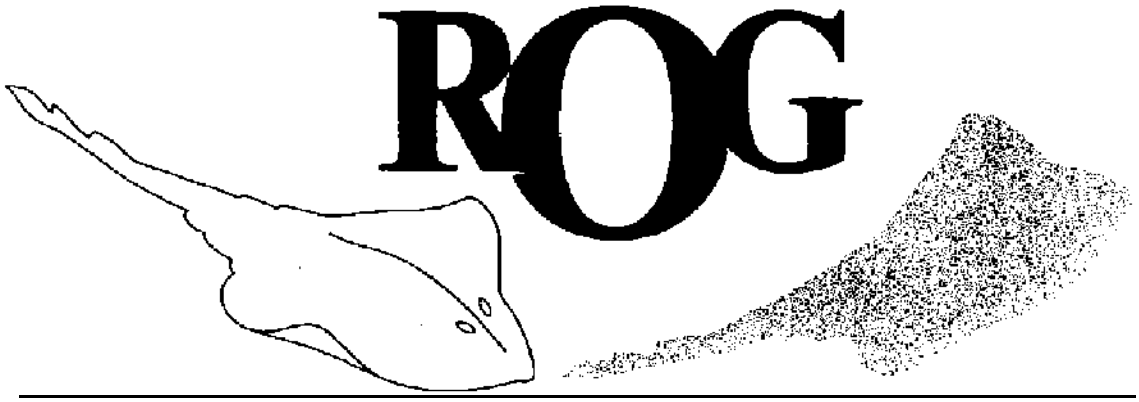

Reflectometer for surface and interfacial studies

Interfacultair Reactor Instituut
Technische Universiteit Delft / Delft University of Technology

April 1995

ROG
a neutron reflectometer at IRI

V.-O. de Haan

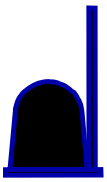

Interfacultair Reactor Instituut
Technische Universiteit Delft / Delft University of Technology

April 1995

Cover photograph: A ray reflecting at an interface boundary. ROG is the Dutch name for a ray. Designed by Ad A. van Well.

CIP-DATA KONINKLIJKE BIBLIOTHEEK, DEN HAAG

Haan, V.-O. de

ROG a neutron reflectometer at IRI / V.-O. de Haan. -
Delft : Interfaculty Reactor Institute, Delft University
of Technology. - I11.
Thesis Technische Universiteit Delft. - With ref.
ISBN 90-73861-23-3
NUGI 812
Subject headings : neutrons ; reflectometry /
position-sensitive detectors / polymers ; adsorption.

ROG
a neutron reflectometer at IRI

PROEFSCHRIFT

ter verkrijging van de graad van doctor aan de Technische Universiteit Delft,
op gezag van de Rector Magnificus Prof. ir. K.F. Wakker,
in het openbaar te verdedigen ten overstaan van een commissie,
door het College van Dekanen aangewezen,
op maandag 24 april 1995 te 16:00 uur door

Victor-Otto DE HAAN

natuurkundig ingenieur
geboren te Dordrecht

Dit proefschrift is goedgekeurd door de promotor: Prof. dr. ir. L.A. de Graaf

Dr. ir. A.A. van Well heeft als begeleider in belangrijke mate aan het totstandkomen van het proefschrift bijgedragen.

Samenstelling promotiecommissie:
Prof. dr. ir. L.A. de Graaf
Prof. dr. ir. C.W.W. van Eijk
Prof. dr. J.F. van der Veen
Prof. dr. G.J. Fleer
Prof. dr. J.J.M. Braat
Dr. ir. A.A. van Well
Dr. G.P. Felcher

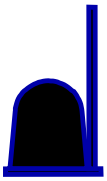

The research described in this thesis was performed within the Department of Radiation Physics of the Interfacultair Reactor Instituut, Delft University of Technology, Mekelweg 15, 2629 JB Delft, The Netherlands.
Financial support was obtained from the Research Stimulation Fund of the Delft University of Technology, known as 'commissie Beek'.

To my parents,

to Annemarie,

with love

Contents

List of Fundamental Constants **iii**

Preface **v**

1 Introduction **1**

2 Principle of neutron reflection **5**
2.1 Introduction 5
2.2 Quantum mechanical description of reflection 6
2.3 Reflection at a perfect interface 10
2.4 Reflection from a multilayer 13
2.5 Reflection from a single layer 15
2.6 Roughness of interfaces 16
2.7 Inverse problem 18
2.8 Retrieval of phase information 19

3 Description **25**
3.1 Introduction 25
3.2 Principle and global set-up 26
3.3 Stacked neutron guide 29
3.4 Short frame 32
3.5 Beam definition 33
3.6 Sample compartment 43
3.7 Detection 43
3.8 Translations and rotations 44

4 Position sensitive detector **45**
4.1 Introduction 45
4.2 Influence of shaping amplifier 46
4.3 Influence of background radiation 48
4.4 Position determination 53
4.5 Spatial resolution 54
4.6 Lower, middle and upper discrimination levels 60
4.7 Conclusions 62

5 Data handling **63**
5.1 Introduction 63
5.2 Corrections and calibrations 65
5.3 Fit procedure 75
5.4 Genetic algorithms 76
5.5 Parameter correlations 79

6 Adsorption of diblock copolymers at the air-water interface **81**
6.1 Introduction 81
6.2 Theory of terminally-attached polymers 82
6.3 Sample preparation and model 82
6.4 Surface-pressure measurements 84
6.5 Neutron reflectivity measurements 87
6.6 Discussion and conclusions 89

7 Concluding remarks **93**

A Flight path determination **99**

B Falling neutrons in reflectometers **103**

C Comparison reflectometers at a continuous neutron source **107**

Summary **114**

Samenvatting (Summary in Dutch) **116**

Acknowledgements **117**

List of Publications **120**

Curriculum Vitae **121**

List of Fundamental Constants

symbol	description	quantity[†]	unit
N_a	Avogadro constant	$6.0221367(36) \times 10^{23}$	mol^{-1}
k	Boltzmann constant	$1.380658(12) \times 10^{-23}$	JK^{-1}
g_r	gyro magnetic ration neutron	$-1.91304275(45)$	
m_n	neutron mass	$1.6749286(10) \times 10^{-27}$	kg
μ_N	nuclear magneton	$5.0507866(17) \times 10^{-27}$	JT^{-1}
μ_o	permeability of vacuum	$4\pi \times 10^{-7}$	NA^{-2}
h	Planck constant	$6.6260755(40) \times 10^{-34}$	Js
$\hbar$	Planck constant divided by 2π	$1.05457266(63) \times 10^{-34}$	Js

[†]Source: Physics Today, August 1993.

Preface

In 1987 at the Interfacultair Reactor Instituut of the Delft University of Technology the idea arose to build a neutron reflectometer to investigate surfaces and interfaces. This field was becoming more important and there were many groups dedicating their time to the investigation of surfaces, interfaces and thin layers. Also, neutron reflectometry was a new technical development to which a scientific contribution could be made.

For measurements with a neutron reflectometer the signal-to-noise ratio is very important. The neutron beam intensity compared to the background count-rate due to gamma radiation and fast neutrons should be as large as possible. The development of the stacked neutron guide, which has a good signal-to-noise ratio, gave the possibility to build a reflectometer with a performance comparable to reflectometers at other sources.

A feasibility study of the possibilities of useful measurements with a neutron reflectometer at the Hoger Onderwijs Reactor of IRI was completed in 1988. This study was affirmative. It was decided that a neutron reflectometer was going to be built at IRI and a project group was formed. The name of the reflectometer is ROG, acronym of 'Reflectometer voor oppervlakte- en grenslaagonderzoek', Dutch for 'Reflectometer for surface and interfacial studies'.

A substantial part (Dfl 1.1 million) of the project was financed by the Delft University of Technology via the 'Research Stimulation Fund' known as the 'commissie Beek'. The sponsoring included two Ph.D. students for four years. This thesis reflects the efforts of one of them.

The definition study was completed in 1990. After some 'hot' discussions about the method to determine the wavelength of the neutrons used, it was decided that the time-of-flight method should be used rather than the use of the Larmor method or monochromatic neutrons.

1991 was dedicated to the design of the mechanics, electronics and software. A substantial part of the mechanics, electronics and software had to be developed. Especially the development of the electronics for the position-sensitive detector was an achievement.

1992 was used to construct the main parts and in the first months of 1993 ROG was installed...

Chapter 1

Introduction

In the beginning was the Word,
and the Word was with God,
and the Word was God.
He was in the beginning with God;
all things were made through him,
and without him was not anything made that was made.

In him was life,
and the life was the light of men.

The light shines in the darkness,
and the darkness has not overcome it.

John 1:1-5

In the last few years there has been a significant effort in the academic and industrial communities to characterize the behavior of atoms and molecules at surfaces and interfaces. A host of new techniques have been devised. Direct imaging techniques, like electron microscopy, scanning tunneling microscopy and scanning force microscopy, give the local structure at the surface only. Reflection techniques, like ellipsometry, neutron or X-ray reflection are complementary and give global information on the structure of the surface or interface over some depth into the material. Furthermore the latter are non-destructive techniques and can be used in situ (the sample is not destroyed by the measurement).

Neutrons have a wave-like character and therefore can be reflected or refracted similar to light or X-rays. The reflectivity depends on the wavelength of the neutrons, the angle of incidence and the nuclear (and magnetic) structure normal to the interface. In 1981 Hayter et al. [1] proposed a new measuring technique (today known as the neutron reflection technique) based on these qualities of the neutron. Since then neutron reflectometers were built at several reactors (for

instance at Saclay, Berlin, Jülich [2], Brookhaven [3]) and pulsed neutron sources (for instance at ISIS [4], Argonne [5], [6]).

The objective of (neutron) reflectivity measurements is the determination of the nuclear (and/or magnetic) structure of samples perpendicular to their surface, the so-called depth profile. Although neutron and X-ray reflectivity measurements are very similar, there are important differences, determined by the different source intensities and reflectivity sensitivities.

The theoretical description of the reflectivity for both techniques is similar. Both reflectivities depend on the scattering-length depth profile of the sample. This depth profile is a function of the direction perpendicular to the interface or surface of the sample. It is determined by the product of the atomic density and the scattering power of the atoms. For an X-ray reflectivity measurement it depends on the electron density given by the atomic number of the constituent elements. For a neutron reflectivity measurement it depends on the scattering length of the constituent atoms, which can be largely different for adjacent elements or isotopes. This offers the possibility of contrast enhancement by isotopic substitution, yielding more detailed information about the structure of the surface or interface. An important example is deuterium substitution, highlighting the structure where many hydrogen atoms are present. This is used in chapter 6 where heavy water was used instead of light water to enhance the reflectivity. Because the neutron has a magnetic moment, it is also sensitive to the magnetic structure of the material. With neutrons magnetic super lattices and other magnetic structures can be measured.

The depth profile can be measured a few hundred nanometers into the sample with a resolution of approximately 1 nm. The penetration depth for X-rays is smaller than for neutrons, due to the absorption of the X-rays in the material. This results in a less extended measurable range of the depth profile for X-rays. This also limits the possibility of X-ray reflection to surfaces, because for buried interfaces the incoming beam would be absorbed. The information about the local structure at the surface or interface is lost, due to the averaging of these techniques.

The source intensity of an X-ray reflection instrument is much larger (1000 times) than that of a neutron reflection instrument. This accounts for the better resolution of X-ray reflectivity measurements, due to the lower reflectivities measurable. The relatively small source intensity with neutron reflectivity experiments indulges the need for large optically-flat samples (some 4 to 20 cm^2) and relatively long measuring times (up to 1 day) for one measurement.

Only where the sample conditions favour a neutron reflection experiment over an X-ray reflection experiment one should use neutrons, because of the relatively long measuring times, accuracy and costs (a standard neutron source is much more expensive than a standard X-ray source, although investments and running costs of the last generation synchrotron and neutron sources are not too different).

Neutron reflection experiments have already been used to investigate many systems ranging from soft condensed materials to magnetic tapes. A recent

overview can be found in [7], [8].

Although neutron reflectivity is an established technique, there are still some unsolved problems regarding the interpretation of neutron reflectivity data. A principal problem is the inversion of the reflectivity data into the depth profile. In a normal reflection experiment only the amplitude of the reflection coefficient is measured. If the phase information were available, it would be possible to calculate the depth profile. Because of the lack of phase information, this is in principle impossible. Knowledge of the sample and physical restrictions (like the maximal possible scattering length density as occurring in nature) provide extra information and most of the time only one depth profile will correspond to the data. If these restrictions are not known or not sufficiently, it is not possible to give a unique depth profile. In chapter 2 it is shown that with a carefully designed experiment it is possible to retrieve the phase information of an unknown layer, from which in principal a unique depth profile can be calculated. Another problem is the lateral structure of the sample at the interface or surface. Normally the reflectivity is measured in the specular direction. This means that the angle of incidence is equal to the angle of reflection. The lateral structure gives rise to off-specular reflection and a reduction in the specular reflectivity. This reduction depends on the lateral height-height correlation function of the surface. Although an exact description goes beyond the scope of this thesis, an introduction to this subject is given in chapter 2.

Chapter 3 describes the ins and outs of ROG, the Delft neutron reflectometer. Special features, indispensable for the performance, are highlighted.

ROG has the possibility to measure the off-specular reflectivity, giving information about the lateral structure of the sample. Therefore a position-sensitive detector is applied. The basic electronics, the calibration measurements and the method used to reduce the background countrate due to gamma radiation are described in chapter 4.

The data handling in chapter 5 describes the correction procedures for the measured reflectivity data, calibration measurements and fit procedures. To invert the measured reflectivity data to a scattering-length depth profile model, a fit procedure is needed. Due to the high non-linearity and the non-unique character of the calculations involved, simple fit procedures using gradient methods are only useful to apply if a solution is (almost) known. A more robust way to find a good set of parameters for a fit is to apply Genetic Algorithms. These and correlations between fit parameters of the model are also discussed.

A report of an investigation of the adsorption of diblock copolymers at the air-water interface is given in chapter 6. Here it is shown that neutron reflectivity measurements give quantitative information about the volume-fraction profile of a polymer at the interface. From these measurements it is concluded that the self-consistent field theory is able to describe the adsorption within the statistics of the measurement.

Chapter 2

Principle of neutron reflection

That men may know wisdom and instruction,
understand words of insight,
receive instructions in wise dealing,
righteousness, justice, and equity;

that prudence may be given to the simple,
knowledge and discretion to the youth -

the wise man also may hear and increase in learning,
and the man of understanding acquire skill,
to understand a proverb and a figure,
the words of the wise and their riddles.

Proverbs 1:2-6

2.1 Introduction

Neutrons interact with materials in several ways. Some interactions can transfer energy from or to the neutron. Other interactions leave the energy of the neutron unchanged but affect its momentum. Two descriptions of the effects of the interaction of a neutron with a material, where the energy of the neutron is unchanged, are known as Bragg and specular reflection. Both descriptions are based on the dynamical theory of scattering [9]. This theory describes the scattering of absolute-coherent neutron waves, i.e. the scattered waves interfere with the incident wave. In general, waves can only interfere if they have the same frequency, so that the scattering considered here is elastic (no energy transfer). The major difference between the two descriptions is the way the neutrons are influenced by the atoms of the material. Bragg reflection is due to the interference of the scattered neutron wave from atoms of a material at discrete positions in space. Specular reflection is due to the interference of the scattered neutron wave from atoms of a material averaged out over space.

In general, when small momentum transfers (less than 1 nm^{-1}) are considered, the interaction of the neutron with the material is spread out over a large distance in space, due to the quantum mechanical character of the neutron and material. The individual contributions of the atoms to the interaction are averaged over this distance. This interaction can be described by an effective potential, determined by the averaging out of the individual contributions of the atoms. Structural information within the order of the averaging distance is lost. The averaging distance is of the same order as the inverse of the momentum transfer of the neutron to the material.

The theory of specular reflection is based on non-relativistic quantum mechanics, so the classical Schrödinger equation can be used. It describes the scattering of neutrons in the specular direction (the angles between the incident beam and sample plane and the reflected beam and sample plane are the same). A more sophisticated and extensive description can be found in [10]. Scattering in the off-specular direction (for instance evanescent-wave scattering or roughness scattering) is not covered by this description.

In the next sections a method is given to calculate the reflectivity of the neutrons given a certain scattering-length density, which is proportional to the average potential. This method is firstly applied to a perfect interface between two media. Then, the method is extended to multiple perfect interfaces, creating a multilayer. Furthermore an example is discussed to get some idea about the quantities involved. After that the theory is extended to include rough interfaces. Finally the inverse problem is discussed and a method to retrieve the phase of the reflectance.

2.2 Quantum mechanical description of reflection

In non-relativistic quantum mechanics, the motion of a particle of mass m and energy E in a stationary potential V is determined by the Schrödinger equation for the probability amplitude Ψ,

$$-\frac{\hbar^2}{2m}\nabla^2\Psi + V\Psi = E\Psi \quad . \tag{2.1}$$

Here $\hbar$ is the Planck constant divided by 2π. The wavenumber k is defined as

$$k^2 = \frac{4\pi^2}{\lambda^2} = \frac{2m}{\hbar^2}(E - V) = k_o^2 - \Gamma \quad , \tag{2.2}$$

where λ is the De Broglie wavelength of the particle and $\hbar^2k^2/2m$ its kinetic energy. Γ is a measure for the potential and k_o is the wavenumber in vacuum. Now eq. (2.1) becomes

$$\nabla^2\Psi + k^2\Psi = 0 \quad . \tag{2.3}$$

The interaction potential of a neutron with a material, also known as the 'optical potential', V is given by [9]

$$V = \frac{\hbar^2}{m_n} 2\pi < N(b_c - ib_a) > \quad , \tag{2.4}$$

where m_n is the neutron mass, N the atomic-number density, b_c the coherent-scattering length averaged for all isotopes the material contains and b_a a measure for the absorption and incoherent scattering of the neutrons in the material. Absorption of neutrons is taken into account by the negative imaginary part of V [11]. When neutrons are scattered incoherently, the coherent neutron intensity is reduced. This can be taken into account by increasing the negative imaginary part of V, similar to the way the absorption is taken into account.

In general if a material is magnetic an extra term for the potential energy is introduced, given by [12]

$$g_r \mu_N \mu_o \hat{\sigma}.\vec{B} \quad , \tag{2.5}$$

where g_r is the gyromagnetic ratio of the neutron (-1.9130), μ_o the permeability of vacuum, μ_N the nuclear Bohr magneton, $\hat{\sigma}$ the Pauli spin matrix and $\vec{B}$ the magnetic induction acting on the neutron.

If the direction of the magnetic moment of the neutron is parallel (+) or antiparallel (−) to the magnetic induction it can be shown that the scattering length becomes

$$b_c = b_n \pm b_m \frac{B}{B_s} \quad , \tag{2.6}$$

where b_n is the nuclear-scattering length, b_m the magnetic-scattering length and B_s the magnetic induction of the material in saturation. The magnetic-scattering length is calculated by [12]

$$b_m = \mu \frac{g_r m_n \mu_N \mu_o}{2\pi\hbar^2} \quad , \tag{2.7}$$

where μ is the magnetic moment per atom. Here, the magnetic moment of the atoms is assumed to be parallel or anti-parallel to the neutron spin.

$\Gamma = 2m_n V/\hbar^2$ is called the scattering-length density and can be interpreted as the potential in 'wavevector-squared units'. It can be calculated by

$$\begin{aligned} \Gamma &= \Gamma_n \pm \Gamma_m - i\Gamma_a \quad , \\ \Gamma_n &= 4\pi < N b_n > \quad , \\ \Gamma_m &= 4\pi < N b_m B/B_s > \quad , \\ \Gamma_a &= 2\pi < N(\sigma_{abs}(\lambda) + \sigma_{inc})/\lambda > \quad . \end{aligned} \tag{2.8}$$

Here $\sigma_{abs}(\lambda)$ is the neutron-absorption cross section and proportional to λ for a $1/v$-absorber, σ_{inc} the incoherent-neutron cross section and constant for most

practical cases. Note that Γ_a is independent of the wavelength for a $1/v$-absorber, when the incoherent scattering is negligible. For some materials the real and imaginary parts of Γ are given in table 2.1.

Material	Γ_n 10^{-3} nm^{-2}	Γ_m 10^{-3} nm^{-2}	Γ_a 10^{-6} nm^{-2}
Al	2.614(5)	-	< 0.1
Ar[1]	0.512(3)	-	< 0.1
^{36}Ar[1]	6.67(4)	-	0.39(4)
Au	5.54(5)	-	20.00(3)
B	8.68(8)	-	350(4)
^{10}B	-0.16(50)	-	1890(20)
C, graphite	9.42(4)	-	< 0.1
C, diamond	14.70(6)	-	< 0.1
Cd	2.83(3)	-	408(8)
Co	2.84(4)	5.2(1)	13.3(2)
Fe	10.07(3)	6.2(1)	0.88(4)
Gd	2.5(2)[2]	-	5258(13)[2]
Ni	11.8(2)	1.8(1)	3.1(2)
^{58}Ni	16.5(2)	1.8(1)	1.5(1)
N_2 [3]	4.087(8)	-	< 0.1
Si[4]	2.6037(6)	-	< 0.1
Ti	-2.45(1)	-	1.8(1)
SiO_2, cristobalite	4.60(2)	-	< 0.1
SiO_2, lechatelierite	4.34(2)	-	< 0.1
SiO_2, tridymite	4.48(2)	-	< 0.1
SiO_2, quartz	5.25(7)	-	< 0.1
H_2O	-0.7024(26)	-	9.40(1)
D_2O	7.993(6)	-	0.26(1)

[1] Liquid Ar at triplepoint (83.78 K; 0.687 bar).
[2] Strongly wavelength dependent.
[3] Liquid N_2 at 77.35 K; 1 bar.
[4] Single crystal at 295.7 K; 1 bar.

Table 2.1: *Real nuclear (Γ_n) and saturated magnetic (Γ_m) parts and (negative) imaginary (Γ_a) parts of the scattering-length density for some materials at 293 K and 1 bar for a neutron wavelength of 0.18 nm.*

Eq. (2.1) can be separated, if a potential or scattering-length density independent of x and y, as defined in fig. 2.1, is considered

$$\Psi(x, y, z) = \Phi_x(x)\Phi_y(y)\Phi_z(z) \quad , \tag{2.9}$$

and the solution of eq. (2.3) is

$$\begin{aligned} \Phi_x(x) &= \alpha_x \mathrm{e}^{ik_x x} + \beta_x \mathrm{e}^{-ik_x x} \quad , \\ \Phi_y(y) &= \alpha_y \mathrm{e}^{ik_y y} + \beta_y \mathrm{e}^{-ik_y y} \quad , \\ \frac{d^2\Phi_z}{dz^2} &+ k_z^2 \Phi_z(z) = 0 \quad , \\ k_z^2 &= k_o^2 - k_x^2 - k_y^2 - \Gamma(z) \quad . \end{aligned} \tag{2.10}$$

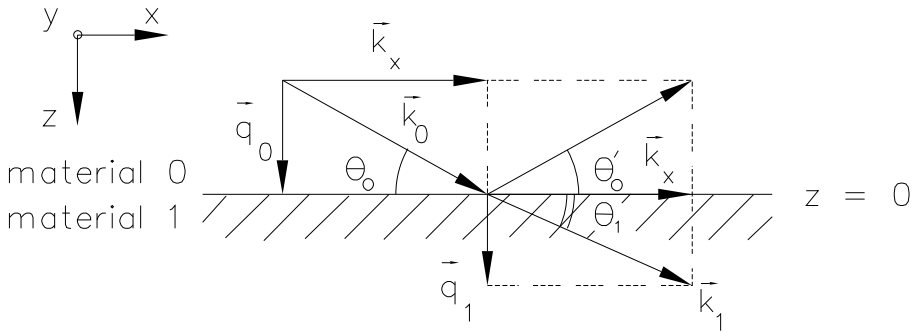

Figure 2.1: *Plane wave impinging on a surface boundary.*

Consider a plane wave with wavevector $\vec{k}$, with k_x, k_y and k_z components in the x, y and z direction respectively. The plane wave is travelling in the x, z plane ($k_y = 0$) in the $+x$ direction ($\beta_x = 0$) as shown in fig. 2.1. Eq. (2.10) reduces to (the subscript z of $\Phi_z(z)$ will be omitted in the following)

$$\begin{aligned} \frac{d^2\Phi}{dz^2} &+ \{q^2 - \Gamma(z)\}\Phi(z) = 0 \quad , \\ q^2 &= k_o^2 - k_x^2 \quad . \end{aligned} \tag{2.11}$$

q is the perpendicular component of the wavevector in vacuum ($\Gamma(z) = 0$), and can be determined by measuring the angle of reflection θ_0 and the wavelength of the neutrons

$$q^2 = (2\pi \frac{\sin\theta_0}{\lambda})^2 + \Gamma_0 \quad , \tag{2.12}$$

where Γ_0 is the scattering-length density of the medium the impinging wave is travelling through. For air or vacuum $\Gamma_0 = 0$.

In general it is very difficult or impossible to solve eq. (2.11). Most of the time not the wavefunction at all z is interesting, but its limiting values for $z \to \pm\infty$. For a particle beam impinging upon a surface, the reflection amplitude or reflectance r and the transmission amplitude t are defined in terms of the solution of eq. (2.11) [10]

$$\Phi(z) = \tau(z)(\mathrm{e}^{i\zeta(z)} + \rho(z)\mathrm{e}^{-i\zeta(z)}) \quad , \tag{2.13}$$

with

$$\begin{aligned}
\frac{d\zeta}{dz} &= \sqrt{q^2 - \Gamma(z)} \quad , \\
\lim_{z\to+\infty} \tau(z) &= t \quad , \\
\lim_{z\to-\infty} \tau(z) &= 1 \quad , \\
\lim_{z\to+\infty} \rho(z) &= 0 \quad , \\
\lim_{z\to-\infty} \rho(z) &= r \quad .
\end{aligned}$$

Then the reflectance $\rho(z)$ is given by

$$\frac{d\rho}{dz} = -\frac{1}{4}\frac{1}{q^2 - \Gamma(z)}\frac{d\Gamma}{dz}(\mathrm{e}^{2i\zeta(z)} - \rho(z)^2\mathrm{e}^{-2i\zeta(z)}) \quad . \tag{2.14}$$

Note that by substitution of $\rho(z) = \mathrm{e}^{2i\zeta}(i\sqrt{q^2 - \Gamma(z)} + g(z))/(i\sqrt{q^2 - \Gamma(z)} - g(z))$ this equation reduces to a 'simple' Ricatti-type differential equation

$$\frac{dg}{dz} = g(z)^2 + q^2 - \Gamma(z) \quad , \tag{2.15}$$

which follows directly from eq. (2.11) assuming $g(z) = -\Phi(z)^{-1}d\Phi/dz$.

From eq. (2.14) it can easily be shown that in the Born approximation (large q and small r) the reflectance is closely related to the Fourier transform of the derivative of the scattering-length-density profile

$$r \approx \frac{1}{4q^2}\int_{-\infty}^{+\infty} \mathrm{e}^{2iqz}\frac{d\Gamma}{dz}dz \quad . \tag{2.16}$$

Some special cases are discussed below.

2.3 Reflection at a perfect interface

Eq. (2.11) can be applied at a surface boundary between two materials or between vacuum and a material. The interface is perfectly flat and the material(s) are isotropic and homogeneous. The scattering-length-density profile, $\Gamma(z)$ of this interface is given by

$$\begin{aligned}
z < 0 \quad \Gamma(z) &= \Gamma_0 \quad , \\
z \geq 0 \quad \Gamma(z) &= \Gamma_1 \quad .
\end{aligned} \tag{2.17}$$

$\Phi(z)$ follows from the solution of eq. (2.11)

$$\begin{aligned}
z < 0 \quad \Phi(z) &= \Phi_0(z) = \alpha_0\mathrm{e}^{iq_0z} + \beta_0\mathrm{e}^{-iq_0z} \quad , \\
z \geq 0 \quad \Phi(z) &= \Phi_1(z) = \alpha_1\mathrm{e}^{iq_1z} + \beta_1\mathrm{e}^{-iq_1z} \quad ,
\end{aligned} \tag{2.18}$$

where $q_i^2 = q^2 - \Gamma_i$ for i is 0 or 1. The physical meaning of the probability amplitude restricts its shape, hence $\Psi(z)$ and $\nabla\Psi(z)$ have to be continuous and finite. These conditions are met by imposing boundary conditions on eq. (2.18)

$$\frac{d\Phi_0}{dz} \mid_{z=0} = \frac{d\Phi_1}{dz} \mid_{z=0} \quad \text{and} \quad \Phi_0(z) \mid_{z=0} = \Phi_1(z) \mid_{z=0} \quad . \tag{2.19}$$

These conditions give

$$\begin{pmatrix} \alpha_1 \\ \beta_1 \end{pmatrix} = \frac{1}{2} \begin{pmatrix} 1+\epsilon_0 & 1-\epsilon_0 \\ 1-\epsilon_0 & 1+\epsilon_0 \end{pmatrix} \begin{pmatrix} \alpha_0 \\ \beta_0 \end{pmatrix} \quad , \tag{2.20}$$

where $\epsilon_0 = q_0/q_1$.
From eq. (2.10) k_x is the same in both media. If the angles of incidence, reflection and refraction are θ_0, θ_0' and θ_1 (see fig. 2.1), the laws of reflection and refraction follow from the invariance of k_x

$$k_0 \cos(\theta_0) = k_0 \cos(\theta_0') = k_1 \cos(\theta_1) \quad . \tag{2.21}$$

This can be compared to Snell's Law, if the index of refraction is defined by

$$n_i = \frac{k_i}{k} = \sqrt{1 - \frac{V_i}{E}} = \sqrt{1 - \frac{\Gamma_i}{k^2}} \quad . \tag{2.22}$$

For a particle beam impinging upon a surface, the reflection and transmission amplitudes (r and t) are defined in terms of the solution of eq. (2.11)

$$\begin{aligned} \alpha_0 = 1 \quad \beta_0 = r \quad , \\ \alpha_1 = t \quad \beta_1 = 0 \quad , \end{aligned} \tag{2.23}$$

yielding with eq. (2.20)

$$r = \frac{\epsilon_0 - 1}{\epsilon_0 + 1} \quad \text{and} \quad t = \frac{2\epsilon_0}{\epsilon_0 + 1} \quad . \tag{2.24}$$

The reflectivity is given by $R = |r|^2$ and is determined by ϵ_0, which depends on the scattering-length densities Γ_0 and Γ_1. Four different possibilities for the potential can be distinguished. These are elucidated in the next sections. In all cases:

$$R = \left| \frac{q_1 - q_0}{q_1 + q_0} \right|^2 , \tag{2.25}$$

where $q_i = \sqrt{q^2 - \Gamma_i}$. In these examples we consider for simplicity non magnetic materials ($b_m = 0$), and vacuum-material surface boundaries only ($\Gamma_0 = 0$ and $\Gamma_1 = \Gamma$).

- **Positive real Γ:** If neutrons are not absorbed in the material $b_a = 0$ and $\Gamma = 4\pi N b_c$, so Γ is positive when b_c is positive. In this case, the reflectivity as a function of q is given by the Fresnel reflectivity

$$R = R_F = \left| \frac{q_1 - q}{q_1 + q} \right|^2 , \tag{2.26}$$

where $q_1 = \sqrt{q^2 - \Gamma}$. In fig. 2.2 the full line represents the reflectivity as function of $q/\sqrt{|\Gamma|}$. Total reflection occurs for $q \leq q_c = \sqrt{\Gamma}$. The tail at large q decreases as $\Gamma^2(2q)^{-4}$.

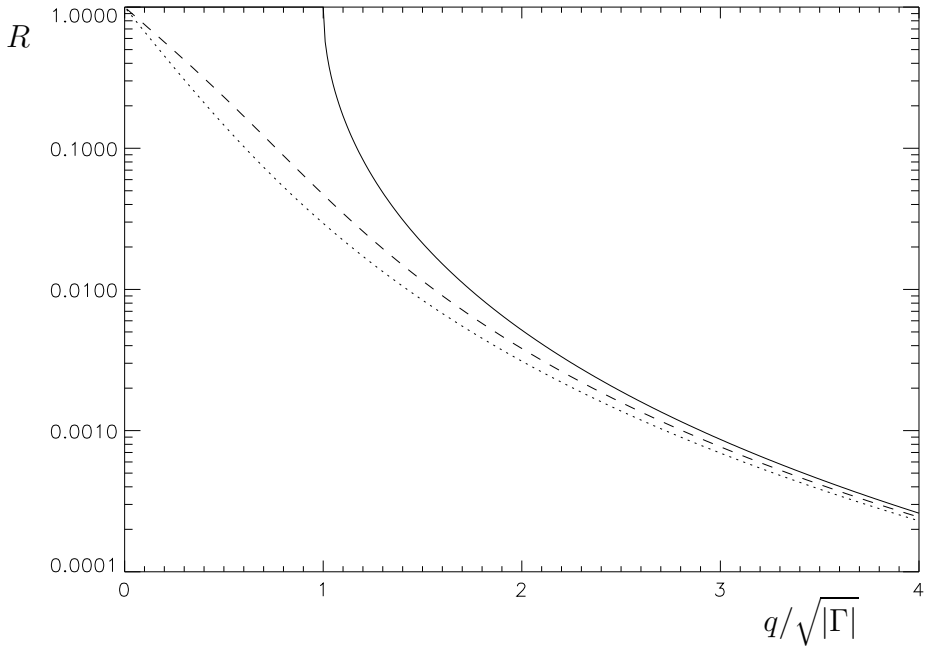

Figure 2.2: *Reflection from a vacuum to material surface boundary. Full line: Fresnel reflection curve; Dotted line: The material has a negative potential; Dashed line: The material has a negative imaginary potential.*

- **Negative real Γ:** If neutrons are not absorbed in the material $b_a = 0$ and $\Gamma = 4\pi N b_c$, so Γ is negative when b_c is negative. In this case, the reflection as function of q is given by 'metallic' reflection

$$R = R_M = \left(\frac{q_1 - q}{q_1 + q} \right)^2 . \tag{2.27}$$

In fig. 2.2 the dotted line represents the reflection as function of $q/\sqrt{|\Gamma|}$. Total reflection only occurs for $q = 0$.

- **Negative imaginary Γ:** If the real part of Γ is 0 neutrons can not be scattered by the real part of the potential. Neutrons are absorbed in the

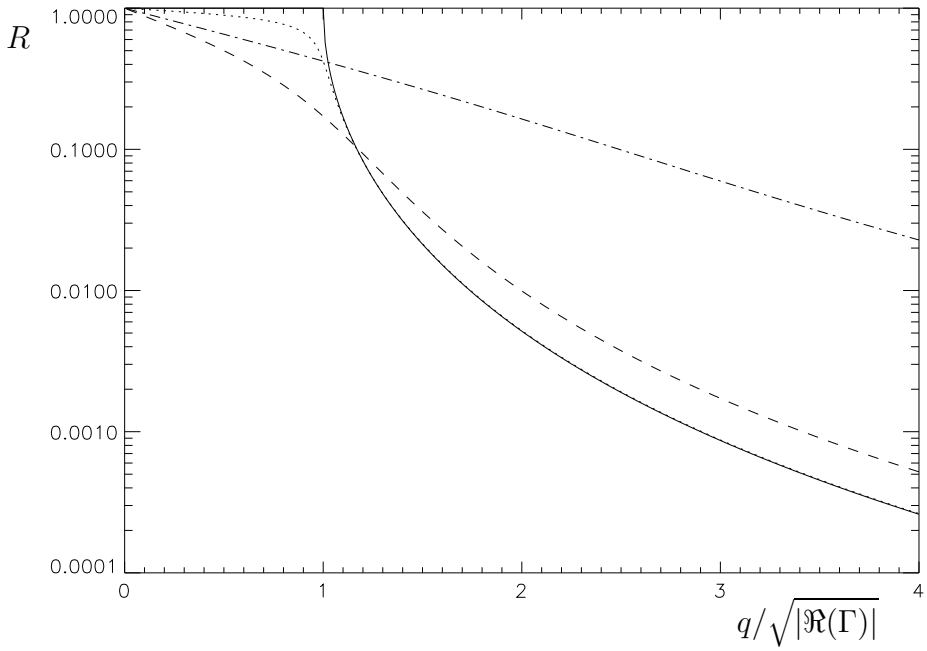

Figure 2.3: *Reflection from a vacuum to material surface boundary. The material has a complex potential. Full line:* $\Gamma_a/\Gamma_n = 0$*; Dotted line:* $\Gamma_a/\Gamma_n = 0.1$*; Dashed line:* $\Gamma_a/\Gamma_n = 1$*; Dashed-dotted line:* $\Gamma_a/\Gamma_n = 10$*.*

material but can also be reflected from the material. Reflection occurs due to the imaginary part of the potential. In fig. 2.2 the dashed line represents the reflection as a function of $q/\sqrt{|\Gamma|}$. Total reflection only occurs for $q = 0$.

- **Complex Γ:** When neutrons are absorbed in the material $\Gamma_a \neq 0$, so the potential is complex. Hence, reflection occurs due to the real and imaginary parts of the potential. In fig. 2.3 the reflection is shown for various Γ_a/Γ_n values as a function of $q/\sqrt{|\Re(\Gamma)|}$, where $\Re(\Gamma)$ is the real part of Γ.

2.4 Reflection from a multilayer

Extension of eq. (2.11) to a non-constant $\Gamma(z)$ yields solutions more difficult or impossible to find analytically. To estimate the reflection of particle waves at such depth profiles, these profiles are considered to be constructed from thin layers of constant potential (see fig. 2.4). Solutions in the form of eq. (2.18) are found at each transition:

$$z_i \leq z \leq z_{i+1} \quad \Phi(z) = \alpha_i \mathrm{e}^{iq_i(z-z_i)} + \beta_i \mathrm{e}^{-iq_i(z-z_i)} \quad . \tag{2.28}$$

By imposing at each interface the conditions that the wave function and its first derivate should be continuous, as expressed in eq. (2.19), the relations between

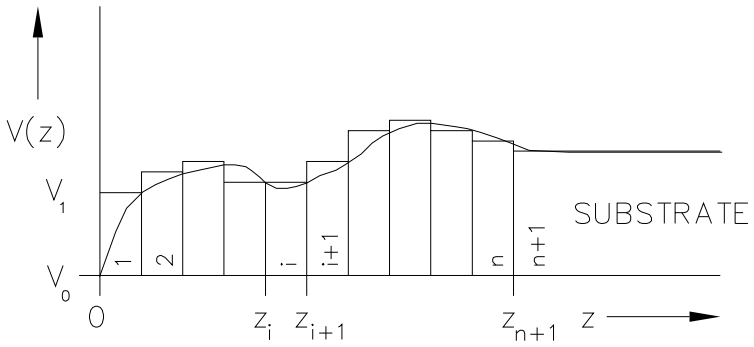

Figure 2.4: *An arbitrary potential barrier, divided in n layers.*

the parameters of layer i and $i+1$ become

$$\begin{aligned} \begin{pmatrix} \alpha_{i+1} \\ \beta_{i+1} \end{pmatrix} &= M_i \begin{pmatrix} \alpha_i \\ \beta_i \end{pmatrix} \quad , \\ M_i &= \tfrac{1}{2} \begin{pmatrix} 1+\epsilon_i & 1-\epsilon_i \\ 1-\epsilon_i & 1+\epsilon_i \end{pmatrix} \begin{pmatrix} \mathrm{e}^{iq_i d_i} & 0 \\ 0 & \mathrm{e}^{-iq_i d_i} \end{pmatrix} \quad , \end{aligned} \tag{2.29}$$

where $\epsilon_i = q_i/q_{i+1}$. The second matrix at the right-hand side of the equation shifts the $z = 0$ position over d_i, the thickness of layer i. d_0 is zero and if i is greater than 0, d_i is given by $z_{i+1} - z_i$. For the total multilayer with n layers is found

$$\begin{pmatrix} \alpha_{n+1} \\ \beta_{n+1} \end{pmatrix} = M_n M_{n-1} \cdots M_1 M_0 \begin{pmatrix} \alpha_0 \\ \beta_0 \end{pmatrix} = M \begin{pmatrix} \alpha_0 \\ \beta_0 \end{pmatrix} \quad . \tag{2.30}$$

As in eq. (2.23) the reflection and transmission amplitudes are defined by

$$\begin{aligned} \alpha_0 = 1 \qquad \beta_0 = r \quad , \\ \alpha_{n+1} = t \quad \beta_{n+1} = 0 \quad , \end{aligned} \tag{2.31}$$

so

$$\begin{pmatrix} t \\ 0 \end{pmatrix} = M \begin{pmatrix} 1 \\ r \end{pmatrix} = \begin{pmatrix} m_{11} & m_{12} \\ m_{21} & m_{22} \end{pmatrix} \begin{pmatrix} 1 \\ r \end{pmatrix} \quad . \tag{2.32}$$

Hence, for the reflectance and the reflectivity is found

$$r(q) = -\frac{m_{21}}{m_{22}} \quad \text{and} \quad R(q) = |r(q)|^2 \quad . \tag{2.33}$$

From eq. (2.29) it can easily be shown that it is possible to calculate the reflectance from recursion relations of the reflectance, $r_i = \beta_i/\alpha_i$ in each layer i

$$r_i = \mathrm{e}^{2iq_i d_i} \frac{r_i^F + r_{i+1}}{1 + r_i^F r_{i+1}} \quad , \tag{2.34}$$

where $r_i^F = (\epsilon_i - 1)(\epsilon_i + 1)^{-1}$, the Fresnel reflectance from material i to $i+1$ and $r_{n+1} = 0$. This relation can also be deduced from eq. (2.14) by assuming

that $\zeta(z)$ is constant at the interface and is similar to the recursion relations derived by Parrat [13] for X-ray and by Fokkema and Ziolkowski [14] for seismic reflection. The advantage of recursion relations is that per layer fewer calculations are needed than for the matrix method. However, for extended repetitions of the same structure in a multilayer it is faster to use the matrix calculations.

2.5 Reflection from a single layer

The reflectivity of a single layer with a thickness d and scattering-length density Γ_l on a substrate with scattering-length density Γ_s can be calculated with eq. (2.34)

$$R = \left| \frac{r_0^F + r_1^F \mathrm{e}^{2iq_l d}}{1 + r_0^F r_1^F \mathrm{e}^{2iq_l d}} \right|^2 \quad , \tag{2.35}$$

where q_l is $\sqrt{q^2 - \Gamma_l}$, r_0^F the Fresnel reflectance from air to layer and r_1^F from layer to substrate. An example is shown in fig. 2.5. The lines represent the reflectivity from a 50 nm thick layer of Ni on top of a glass (SiO_2) substrate (full), the reflectivity from the bare glass substrate (dotted) and the reflectivity from a bare Ni substrate (dashed). The periodic structure is due to the interference of neutrons reflecting from the top and bottom of the Ni layer. For large q this period becomes $\Delta q = \pi/d$. In the Born approximation the reflectivity is

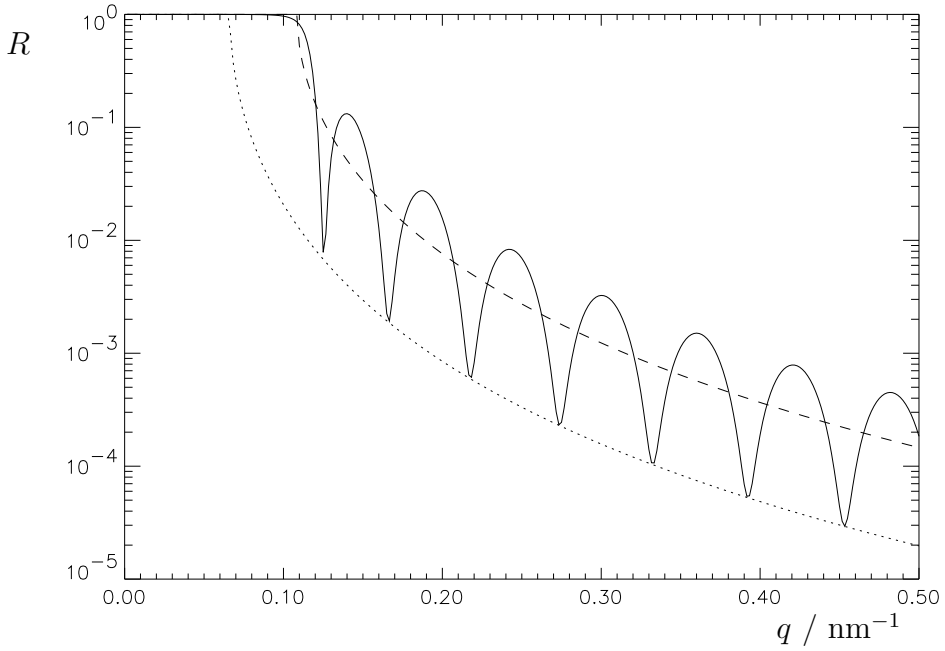

Figure 2.5: *Reflectivity profiles of a single 50 nm thick Ni layer on a glass (SiO_2) substrate (full line), a bare glass substrate (dotted line) and a bare Ni substrate (dashed line).*

calculated according to eq. (2.16) resulting in

$$R \approx \frac{\Gamma_l^2 + (\Gamma_l - \Gamma_s)^2 - 2\Gamma_l(\Gamma_l - \Gamma_s)\cos(2qd)}{16q^4} \quad . \tag{2.36}$$

In fig. 2.6 this reflectivity is shown as the dotted line. The amplitude of the oscillation is calculated more accurately than its phase. Hence, the Born approximation is only valid for $q >> \sqrt{\Gamma_l} \approx 0.11$ nm^{-1}. From eq. (2.35) it can be

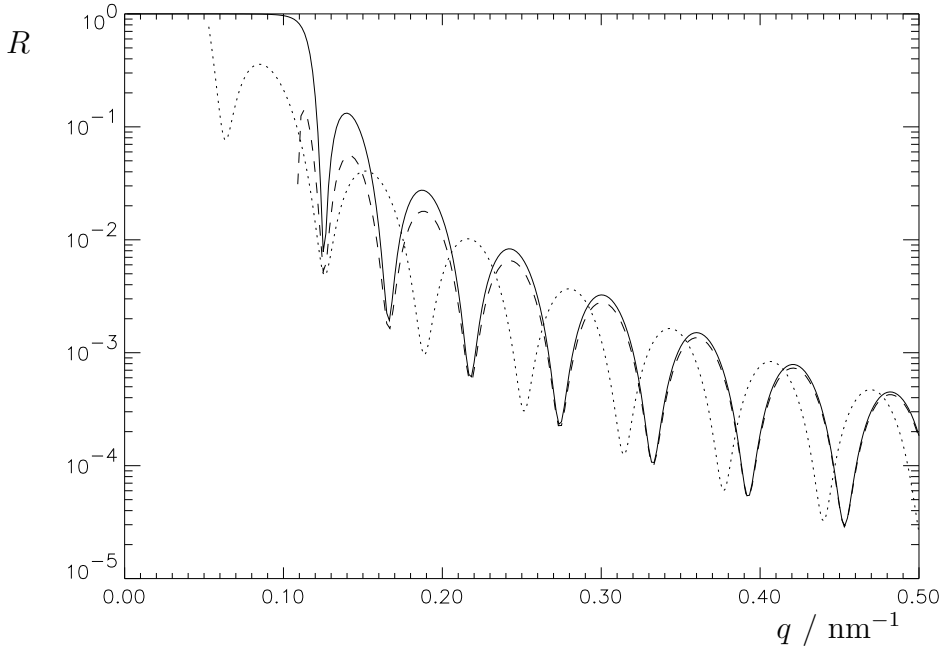

Figure 2.6: *Comparison of the reflectivities of the exact calculations (full line) with the Born approximation (dotted line) and an other approximation as described in the text (dashed line).*

shown that a better approximation is found, when in the argument of the cosine of eq. (2.36) q is replaced by q_l. The result is shown in fig. 2.6 as the dashed line. Only for $q \lesssim 2\sqrt{\Gamma_l}$ the deviations are pronounced. More examples are discussed in the literature [18].

2.6 Roughness of interfaces

In general it is very difficult to describe the reflectivity from a rough interface. Several models suggested in the literature [15]-[18] describe the measured reflectivities with reasonable results. The deviation of the reflectivity from the reflectivity of a perfect interface depends on the height-height correlation function of the roughness. The description of this effect goes beyond the scope of this chapter and can be found elsewhere [19].

Névot and Croce [17] describe the reflectivity at rough interfaces as (destructive) interference of all (non-related) wave functions created by different positions of the interface. They use comparison identities [10] relating r and $\tilde{r}$, which are reflectivities from different scattering-length-density profiles ($\Gamma(z)$ and $\tilde{\Gamma}(z)$) with the same limiting values for $z \to \pm\infty$

$$\lim_{z\to+\infty} \Gamma(z) = \tilde{\Gamma}(z) = \Gamma_1 \quad , \quad \lim_{z\to-\infty} \Gamma(z) = \tilde{\Gamma}(z) = \Gamma_0 \quad . \tag{2.37}$$

It can be shown that

$$\tilde{r} - r = \frac{1}{2iq_0} \int_{-\infty}^{+\infty} (\tilde{\Gamma}(z) - \Gamma(z)) \tilde{\phi}(z) \phi(z) dz \quad , \tag{2.38}$$

with $q_0 = \sqrt{q^2 - \Gamma_0}$ and $\tilde{\phi}(z)$ and $\phi(z)$ are the corresponding wave functions. For a distribution of sharp interfaces the right-hand side of eq. (2.38) should be averaged over all different contributions. Assume $\tilde{\Gamma}(z) = \Gamma_0 + (\Gamma_1 - \Gamma_0)u(z)$ where $u(z)$ is the Heavyside step function. $\Gamma(z) = \Gamma_0 + (\Gamma_1 - \Gamma_0)u(z - z_d)$ is distributed around $z = 0$ according to a Gaussian distribution

$$w(z_d) = \frac{1}{\sqrt{2\pi}\sigma} \mathrm{e}(-\frac{z_d^2}{2\sigma^2}) \quad , \tag{2.39}$$

where σ is a measure for the roughness of the interface. For r is found

$$r - \tilde{r} \approx \frac{\Gamma_0 - \Gamma_1}{2iq_0} \int_{-\infty}^{+\infty} w(z_d) \{ \int_0^{z_d} \mathrm{e}^{iq_1 z} (\mathrm{e}^{iq_0 z} + r\mathrm{e}^{-iq_0 z}) dz \} dz_d \quad , \tag{2.40}$$

with $q_1 = \sqrt{q^2 - \Gamma_1}$. The approximation is introduced since for $\phi(z)$ the average value was taken. It results in a reduction of the reflectance by a kind of Debye-Waller factor

$$r = \tilde{r}\mathrm{e}^{-2q_0 q_1 \sigma^2} \quad , \tag{2.41}$$

This result was generalized by Cowley and Ryan [20] for a multilayer, with non-conformal roughness at the interfaces. Instead of using the Fresnel reflectance in eq. (2.34) one should use the modified reflectance

$$r_i^M = r_i^F \mathrm{e}^{-2q_i q_{i+1} \sigma_{i+1}^2} \quad , \tag{2.42}$$

where σ_i is a measure of the roughness of the interface at z_i (see fig. 2.4). The condition for which this equation holds is that σ_i should be small compared to the layer thickness d_i.

Sometimes the roughness is described as a graded interface, where the scattering-length density around z_i varies according to $w(z - z_i)$

$$\frac{d\Gamma}{dz} = (\Gamma_{i+1} - \Gamma_i) w(z - z_i) \quad . \tag{2.43}$$

According to Névot and Croce this gives the same result as eq. (2.42). In the Born approximation eq. (2.16) directly leads to

$$r_i^M = r_i^F \mathrm{e}^{-2q^2\sigma_{i+1}^2} \quad . \tag{2.44}$$

For neutrons eqs. (2.42) and (2.44) give approximately the same results for the reflectance.

With a correct value of the roughness parameter, the measurements of the reflectivity agree with theory. However, because of the two different interpretations of the roughness parameter as mentioned above, its physical interpretation is not a-priori clear. Which interpretation is used depends on the sample and details of the measurement. Additional measurements could give extra information. With a graded interface, reflection can only occur in the specular direction, while for a distribution of sharp interfaces off-specular reflection can also occur. Hence, the transmission amplitude of a graded interface will be larger than that of a distribution of interfaces. De Boer [21] shows that, when using the second order distorted wave approximation, the reflectance of a rough interface varies between the results of eq. (2.42) and eq. (2.44) and depends on the height-height correlation function of the surface. If this function is given by

$$C(\vec{u}) = \sigma^2 \mathrm{e}^{-(u/\xi)^2} \quad , \tag{2.45}$$

where $\vec{u}$ is a vector in the (x, y)-plane and ξ the correlation length, then eq. (2.42) holds if $q^2\xi/k_o \ll 1$ and eq. (2.44) holds if $q^2\xi/k_o \gg 1$ and $q^2\sigma^2 \ll 1$. There is a crossover for $q^2\xi/k_o = \theta_0\xi q = 1$, so when ξ is of the order of 1 μm. In general ξ is large when off-specular reflection occurs. More details about, and examples of, off-specular reflection can be found in the literature [21], [19].

2.7 Inverse problem

From the measured reflectivity profile, the scattering-length-density profile must be determined. First, from the reflectivity the reflection amplitude or reflectance must be determined, which is a problem because of the loss of phase information. Then, the inversion calculation of the reflectance to the scattering-length-density profile must be performed. The inversion calculation of the reflectance can be done using Gel'fand-Levitan integral equation [22]. The calculation however is difficult and tedious and assumes that the phase information is available. In the literature methods to retrieve the phase from the reflectivity measurement are discussed [23]. For one reflectivity curve these methods yield many solutions for the phase, stressing the non-uniqueness of the solutions. To decide which solution should be used, extra information must be available. This information could be the knowledge of the experimentalist about the structure and physics of the sample and can be deduced from either the construction of the sample or other complementary depth profiling techniques [24]. Another way to get more

information about the sample is the use of contrast variations by for instance isotopic substitution [25].

For non-magnetic samples it is also possible to use polarized neutron reflectivity measurements to get extra information. Sivia and Pynn [26] and Majkrzak et al. [27] discuss the possibility to invert neutron reflectivity data using polarized neutrons and a magnetized substrate. Their method is based on eq. (2.16), and therefore only holds for small reflectivities.

A way to determine a unique scattering-length-density profile is to measure both the amplitude and the phase of the reflectance. In the next section a method is discussed, which demonstrates the possibility to retrieve in principle the phase information by measuring the reflectivity of an unknown layer, through a layer of which the scattering length density can be manipulated in a known way. From three measurements of the reflectivity of this system for different known scattering-length densities of the layers, both the amplitude and the phase of the reflectance of the unknown layer can be calculated.

However, because it is very difficult to retrieve or measure the phase information, mostly model fitting procedures are used to 'invert' the reflectivity profile. Models describing the structure of the sample are used to calculate a reflectivity profile. With least-square fitting procedures or other techniques such as Genetic Algorithms the parameters of the model are fitted to the measured data. The result is a parameterized scattering-length-density profile. Model-fitting procedures are discussed in chapter 5. Other methods are discussed by Sivia et al. [28] and Zhou and Chen [29].

2.8 Retrieval of phase information[†]

In conventional neutron reflection experiments the intensity reflected from an unknown layered structure is used to recover the depth profile by trial and error, often with ambiguous or non-unique results. Straightforward determination of the profile is instead possible by means of the Gel'fand-Levitan equation if both phase and amplitude of the reflectance were known. The recovery of the phase information was sought by adding to the unknown layered structure a known ferromagnetic layer. Most transparent results are obtained in a geometry, where the unknown sample is deposited onto a ferromagnetic film on a convenient substrate. The ferromagnetic layer is magnetized by an external magnetic field in a direction along the sample plane and subsequently perpendicular to it. The neutrons, polarized either parallel or opposite to the magnetic field are sent on the sample from the substrate side. In this way three measurements can be made, with different (and known) scattering-length densities of the ferromagnetic layer.

[†]This section will be published as: 'On the Retrieval of phase information in Neutron Reflectivity', V.O. de Haan, A.A. van Well, S. Adenwalla and G.P. Felcher, Phys. Rev. B (submitted).

The reflectivity obtained from each measurement can be represented by a circle in the (complex) reflectance plane. The intersections of these circles provide the reflectance.

Suppose the film on top of a substrate consists of two parts, with characteristic matrixes G and H. This is shown schematically in fig. 2.7.

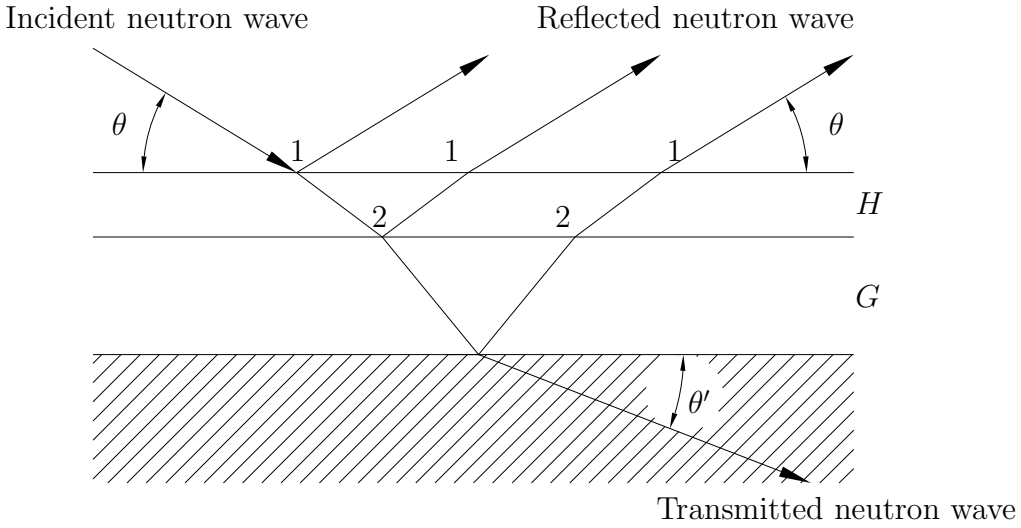

Figure 2.7: *Sketch of a neutron reflection experiment.*

Part H is on top of G, so the incident neutrons first pass H then G. The reflection and transmission amplitudes are found using eq. (2.32)

$$\begin{pmatrix} t \\ 0 \end{pmatrix} = M \begin{pmatrix} 1 \\ r \end{pmatrix} = GH \begin{pmatrix} 1 \\ r \end{pmatrix} \ . \tag{2.46}$$

The reflectance, r can be calculated with eq. (2.33)

$$r = -\frac{m_{21}}{m_{22}} = -\frac{h_{11} r_g - h_{21}}{h_{12} r_g - h_{22}} \ , \tag{2.47}$$

where $r_g = -g_{21}/g_{22}$. Two possibilities can be considered.

First, consider H unknown and G known. The phase of $r_h = -h_{21}/h_{22}$ can not be determined because there are too many unknown variables. If the neutrons first pass the unknown film, it is not possible to retrieve the phase information for every q point independently without extra information about H.

Second, consider G unknown and H known. For r_g is found

$$|r_g - r_c|^2 = r_r^2 \ , \tag{2.48}$$

where r_c and r_r are constants

$$\begin{aligned} r_r &= R^{1/2} \frac{|h_{11} h_{22} - h_{12} h_{21}|}{R\,|h_{12}|^2 - |h_{11}|^2} \ , \\ r_c &= \frac{R h_{22} h_{12}^* - h_{21} h_{11}^*}{R\,|h_{12}|^2 - |h_{11}|^2} \ . \end{aligned} \tag{2.49}$$

Eq. (2.48) represents a circle in the complex plane with centerpoint r_c and radius r_r both determined by H and the measured reflectivity $R = |r|^2$ only. Because h_{11}, h_{21}, h_{12} and h_{22} are known, both the amplitude and the phase of r_g can be uniquely determined from three measurements of R for three different values of H. Two circles, representing two different measurements, intercept at two points (at least 1) because of the physics involved. This leaves two possibilities (at least 1) for r_g. A third measurement gives the possibility to decide.

The reason why the first possibility does not work and the second does can be understood by examining eq. (2.34). The reflectance in a layer is determined by the reflectance of the layers below the layer in combination with the layer itself. Hence, the reflectance in this layer does not depend on the phase or amplitude of the neutron wave above it, but only on the structure of the layers below it and itself. In the first possibility the reflectance at point 2 (see fig. 2.7) of the sample is known. The unknown layer changes the reflectance in some unknown way. If the known layer is changed the reflectance at point 2 also changes. The unknown layer changes the reflectance in some other unknown way, hence preventing the calculation of the phase. In the second possibility the reflectance at point 2 of the sample is not known, but does not change when the structure of the upper layers is changed. The reflectance at point 1 can be calculated from the reflectance at point 2 using the structure of the known layers. If the structure of the known layers is changed the reflectance at point 1 varies in a predictable way depending on the reflectance at point 2, hence giving the possibility to calculate its phase.

The second possibility can be realized using a magnetic layer on top of a silicon wafer. The unknown layer is deposited on top of this. The neutrons hit the unknown layer coming from the substrate through the known (magnetic) layer. The reflected neutrons again go through the silicon substrate. The scattering-length density of the magnetic layer depends on the direction of the neutron spin with respect to the magnetic induction of the sample (see section 2.2). In the calculations presented here the magnetic layer was a 10 nm thick cobalt layer. For the unknown layer a 50 nm thick gold layer was used. The roughness at the gold-air interface was taken 1 nm. Three measurements were simulated using matrix calculations: the reflectivity for a non-magnetized sample and the reflectivity for plus and minus spins from a fully magnetized sample. These measurements are shown as the dotted, full and dashed line of fig. 2.8 respectively. These measurements are used to calculate the amplitude and phase of the reflectance. Here the matrix elements of H were calculated, assuming there is an infinitely small layer between the known and unknown layer with a zero scattering length density. In this way the reflectance of the unknown layer deposited on a substrate with zero scattering-length density is calculated as the mutual intersection of the three circles. The physics involved makes sure that they have one and only one mutual intersection. The results are shown as asterisks in fig. 2.9 and 2.10 respectively. The lines are model calculations using matrix calculations. Clearly the retrieval calculations do not differ from the model calculations. For small q the retrieval calculations can not be performed due to the fact that the incident

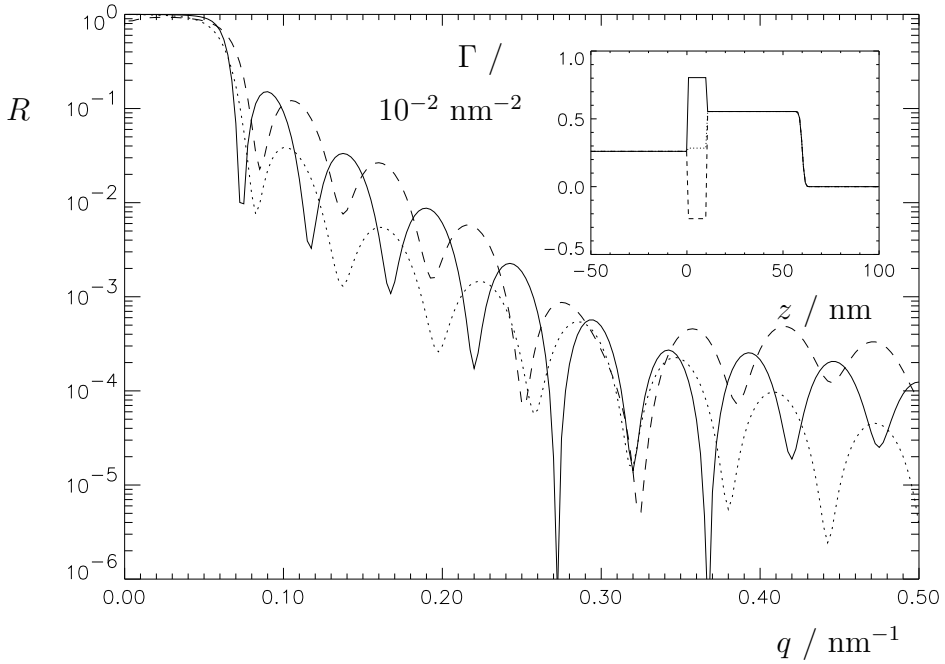

Figure 2.8: *Reflectivity of a sample consisting of a silicon substrate with a 10 nm thick cobalt layer and a 50 nm thick gold layer for three different magnetizations of the cobalt layer: non-magnetized (dotted line); plus (full line) and minus (dashed line) spins for a fully magnetized sample. The inset gives the scattering-length-density profiles for the three different measurements.*

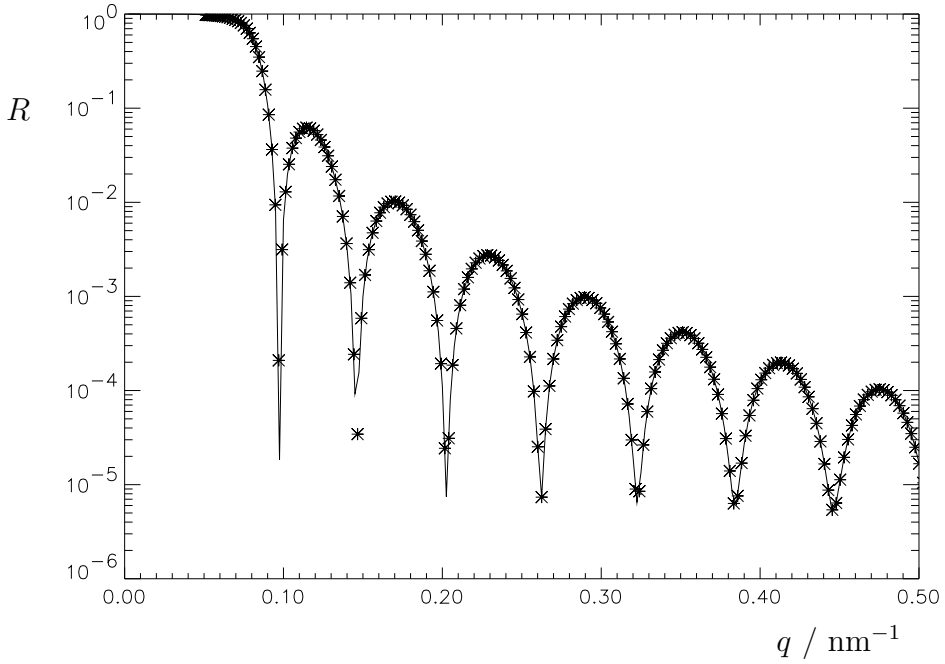

Figure 2.9: *Reflectivity of the gold layer, calculated from the simulated measurements of fig. 2.8 (asterisks) and using matrix calculations (line).*

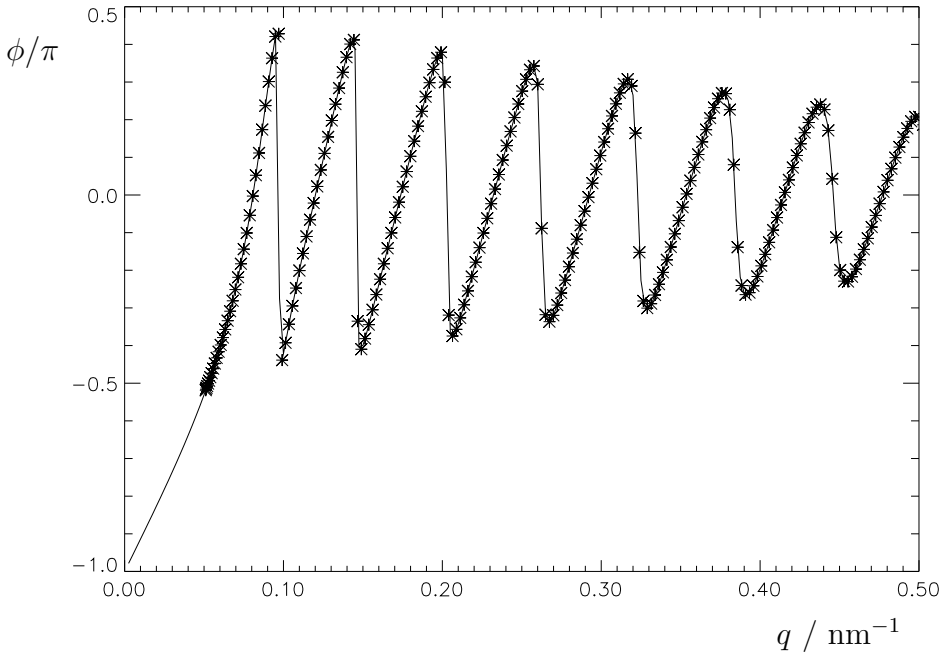

Figure 2.10: *Phase of the reflectance of the gold layer, ϕ calculated from the simulated measurements of fig. 2.8 (asterisks) and using matrix calculations (line).*

neutrons travel through silicon and the smallest q reachable is determined by the square root of the scattering-length density of silicon (0.051 nm^{-1}). An important aspect of the calculation is that it is performed for every q-value independently. No correlation between the calculated reflectances is introduced. Hence with these ideal measurements it is possible to retrieve both the amplitude and the phase of the reflectance.

In practice this technique is complicated by the influence of statistics and resolution. It is possible that these effects, if large enough, mess up the calculation of the mutual intersection of the circles. However, with sufficient statistics and resolution, this technique promises to be powerful in retrieving the scattering-length-density profile of non-magnetic samples.

Chapter 3

Description[†]

... And thou, fresh piece of excellent witchcraft,
who of force must know the royal fool thou copest with ...

W. Shakespeare

3.1 Introduction

The objective of a reflectivity experiment is to determine the scattering-length-density profile of a sample. This profile is determined by the inversion of a measured reflectivity curve from that sample. A reflectivity curve is the reflectivity as a function of q, the component of the wavevector perpendicular to the surface of the sample. Eq. (2.12) gives

$$q = \frac{2\pi \sin\theta}{\lambda} \quad , \tag{3.1}$$

where θ is the angle of incidence and λ the neutron wavelength. Both by changing λ or θ it is possible to vary q. The reflectivity is determined by measuring the incident- and reflected-beam intensities. The incident neutron intensity is measured by a monitor. After reflection from the sample the neutrons are detected in either a single or a position-sensitive detector.

The design of ROG is based on the following starting points:

- An optimum intensity/resolution performance with regard to the available neutron source and measuring time. In general an increase in resolution

[†]This chapter is published in a modified form as: 'ROG, the new neutron reflectometer at IRI, Delft', A.A. van Well, V.O. de Haan and H. Fredrikze, Physica B **198** (1994) 217 and 'ROG, the neutron reflectometer at IRI, Delft', V.O. de Haan, J. de Blois, P. van der Ende, H. Fredrikze, A. van der Graaf, M.N. Schipper, A.A. van Well and J. van der Zanden, Nucl. Instrum. Methods in Phys. Res. A (accepted).

decreases the intensity of the neutron beam and hence the accuracy due to counting statistics. Matching all resolution contributions will give the best performance. For instance, a special chopper was designed to match the wavelength resolution contribution to the geometrical resolution contribution.

- The possibility to measure the reflectivity curve of liquid samples is facilitated by a horizontal sample geometry.
- The possibility to measure the magnetic depth profile of a sample for which polarized neutrons are needed.
- The possibility to measure off-specular reflection for which a position-sensitive detector is used.
- The possibility to change the instrumental settings or sample conditions continuously and reproducibly during a measurement series demands complete computer control.

The realization of these starting points are elucidated in the next sections.

3.2 Principle and global set-up

ROG has been installed at the stacked neutron guide (SNG) [30] in beamtube L2 of the 2 MW swimming-pool reactor HOR of IRI at Delft University of Technology. From this guide a continuous neutron beam emerges with a very small fraction of unwanted (gamma and fast-neutron) radiation. This is of crucial importance for ROG, because the background countrate should be as small as possible, as the minimum reflectivity measurable by ROG is directly determined by the background countrate.

As the scattering-length densities of all materials are very small, the interesting q region is below 5 nm^{-1}. The available neutron wavelength range is between 0.07 and 1.5 nm, so θ should be less than 0.1 radians, usually θ varies between 5 and 15 $\times 10^{-3}$ radians. Therefore, a neutron beam is needed that allows measurements at small angles with reasonable intensity and resolution. Two horizontal-slit diaphragms, placed at a large distance from each other, create a narrow incident beam that can reflect from a sample under small incident angles. The spread in the angle of reflection and the intensity of the incident beam are determined by the heights of and the distance between the diaphragms. The relation between them is given in section 3.5.1. This relation shows that a large distance between the diaphragms is favourable with regard to the incident beam intensity when the spread in reflection angle is kept constant.

A choice was made to measure at a constant angle and to vary the wavelength, because in this way the geometry does not change during the measurement. Moreover, it is easier to measure liquid samples. To measure wavelength-dependent

intensities, the time-of-flight (TOF) method is used. This method uses a pulsed neutron beam created by a chopper. The wavelength of a neutron is determined by measuring the time of flight between chopper and detector, t_{TOF}. Because the length of the flight path between the chopper and the detector, L_{TOF} is known, the velocity of the neutron, v and hence its wavelength, λ can be calculated from

$$v = \frac{L_{TOF}}{t_{TOF}} \quad \text{and} \quad \lambda = \frac{h}{m_n L_{TOF}} t_{TOF} \quad , \tag{3.2}$$

where h is the Planck constant and m_n the neutron mass. The monitor and detectors are coupled to multi-channel analyzers. In every channel of the analyzer neutrons are counted which arrive at the monitor or detector in the corresponding time window. The time scale of the analyzer is started by a reference pulse of the chopper. The time windows of the analyzer are adjusted by the user. Commonly it is argued that at a continuous source the monochromatic method, where the wavelength of the neutron is kept constant and the reflection angle is changed, is favourable over the time-of-flight method considering the measuring times, because of the loss of intensity due to the chopper in the beam. However, with an optimally designed reflectometer the measuring times of both methods are comparable, which is elucidated in appendix C.

From eq. (3.1) it follows that the resolution of the instrument is given by two terms:

$$(\frac{\sigma_q}{q})^2 = (\frac{\sigma_\theta}{\theta})^2 + (\frac{\sigma_\lambda}{\lambda})^2 \quad , \tag{3.3}$$

where σ denotes the standard deviation of the parameter. To obtain an optimum resolution-intensity performance both contributions should match. The geometrical resolution contribution, σ_θ/θ is determined by the geometry of the diaphragms and the macroscopic flatness of the sample surface. Therefore it does not depend on the wavelength of the neutrons. This implies that σ_λ/λ should preferentially be constant too. According to eq. (3.2)

$$(\frac{\sigma_\lambda}{\lambda})^2 = (\frac{\sigma_{t_{TOF}}}{t_{TOF}})^2 + (\frac{\sigma_{L_{TOF}}}{L_{TOF}})^2 \quad , \tag{3.4}$$

where $\sigma_{L_{TOF}}$ is the uncertainty in L_{TOF} due to different flight paths and is relatively small. $\sigma_{t_{TOF}}$ is due to the pulse width and the detection time uncertainty and given by

$$\sigma^2_{t_{TOF}} = \frac{1}{12}(\Delta t_c^2 + \Delta t_i^2 + \Delta t_g^2) \quad . \tag{3.5}$$

Here, Δt_c is the burst time of the chopper, Δt_i the channel width of the corresponding channel of the TOF analyzer and Δt_g, due to the finite height of the diaphragms, is usually negligible. To obtain a constant σ_λ/λ both Δt_c and Δt_i should be proportional to λ. Δt_i can be adjusted by an appropriate choice of the time windows of the multi-channel analyzers. Δt_c is proportional to λ due to the use of a double-disk chopper (see section 3.4.3).

The average transmission of the chopper increases linearly with the pulse frequency, f. Due to duty-cycle overlap the maximum frequency is limited by

the used wavelength range of the neutrons. Duty-cycle overlap is the effect that slow neutrons arrive at the detector at the same time as the faster neutrons of the next pulse. This effect becomes more important when the pulse frequency is increased, but can be avoided by limitation of the accepted wavelength range according to

$$f = \left(\frac{m}{h} L_{TOF}(\lambda_{\max} - \lambda_{\min})\right)^{-1} \quad , \tag{3.6}$$

where $\lambda_{\max}$ and $\lambda_{\min}$ determine the wavelength range and f the pulse frequency. The wavelength range is limited by reflection of the beam at a super mirror and transmission through a frame-overlap mirror. The lower limit is determined by reflection of the beam at the super mirror, with reflection angle γ. Fast neutrons can not be reflected at this super mirror. The upper limit is determined by reflecting slow neutrons out of the beam by the frame-overlap mirror. Again, fast neutrons can not be reflected at this mirror. Hence, the minimum and maximum wavelength in the neutron spectrum can be adjusted by changing the reflection angle at the super mirror and frame-overlap mirror respectively.

For magnetic materials the reflectivity depends on the direction of the spin of the neutrons compared with the magnetic induction at the sample (see section 2.2). For these measurements a polarized beam is needed, which can be created by the super mirror. A spin flipper is used to flip the neutron spin from parallel to the magnetic induction into anti-parallel. To avoid depolarization by stray fields, a magnetic guide field is present along the flight path from super mirror to sample.

Neutron guides, consisting of two vertical glass plates coated with ^{58}Ni, are installed to avoid spreading of the beam in horizontal direction. To obtain accurate and reproducible experimental settings most translations and rotations are equipped with computer-controlled motors and position encoders.

The flexibility of the instrument facilitates measurements in 3 different modes:

A The beam is reflected (and possibly polarized) downwards by the super mirror and upwards from the top side of the sample (fig. 3.1a).

B The beam is reflected (and possibly polarized) upwards by the super mirror and downwards from the bottom side of the sample (fig. 3.1b).

C The beam is not reflected by the super mirror and is reflected upwards from the top side of the sample (fig. 3.1c).

In fig. 3.2 a schematic overview of ROG is shown. Because all components should be aligned along the (straight) beam, they were all attached to a frame that can be adjusted in height and angle. When the super mirror is used to create a polarized neutron beam, it also deflects the beam. The components before the super mirror should be aligned along the incoming beam and the ones after the super mirror should be aligned along the deflected beam. Therefore the coarse collimator, monitor 1 and chopper were attached to a separate short frame. This

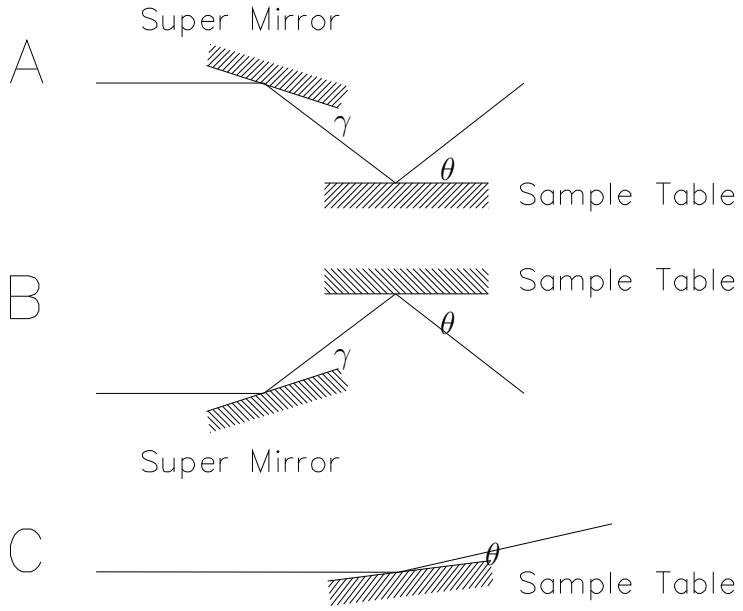

Figure 3.1: *Sketch of the path of the neutron beam in different modes. γ is the angle between beam and super mirror; θ the reflection angle.*

is also favorable to suppress the chopper's vibrations due to the rotation of the chopper blades with angular frequencies up to 20000 rpm. These vibrations could influence the reflectivity measurement of liquid samples.

The long frame supports all other components, which are mounted on the frame in three different compartments: beam definition, sample and detection compartment. The beam definition compartment is used to create a narrow well-defined (not) polarized neutron beam and to limit the available neutron wavelength range. The sample compartment is used to control the sample environment. The detection compartment is used to support shielding diaphragm, detectors and beamstop. The three compartments can be independently filled with argon gas having a pressure of 1 atm to suppress intensity loss and small-angle scattering. Height and angle of the long frame can be adjusted computer controlled. This makes it possible to select a different part of the beam emerging from the stacked neutron guide and to control the reflection angle, when a liquid sample is used.

In the next sections the neutron source and the different parts of ROG are described in more detail. For every part the important effects on the reflectivity measurement are shown. Tests and calibration measurements are also discussed.

3.3 Stacked neutron guide

The SNG contains 2 beam channels, one of which is inclined downwards by 0.0133 radians. This creates the possibility to measure liquid samples at small wavelengths, because the neutron beam does not have to be deflected. Each beam

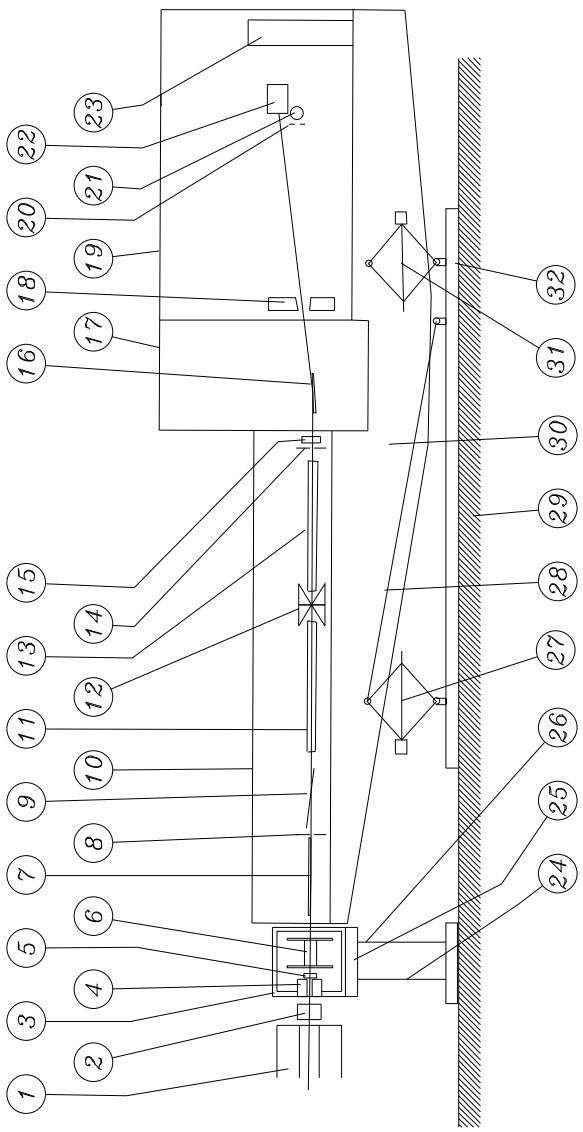

1	Stacked neutron guide
2	Beam shutter
3	Pb shielding
4	Coarse collimator
5	Monitor 1
6	Double-disk chopper
7	Super mirror
8	Diaphragm 1
9	Frame-overlap mirror
10	Beam def. compart.
11	Neutron guide
12	Spin flipper
13	Neutron guide
14	Diaphragm 2
15	Monitor 2
16	Sample
17	Sample compartment
18	Shielding diaphragm
19	Detector compartment
20	Detector diaphragm
21	Single detector
22	Pos. sens. detector
23	Beamstop
24	Leg 1
25	Short frame
26	Leg 2
27	Leg 3
28	Stabilizer rod
29	Smooth floor
30	Long frame
31	Leg 4
32	Steel basis

Figure 3.2: *Schematic layout of ROG*

channel is composed of 13 micro channels. A micro channel has a height of 60 mm, a width of 1 mm and a length of 3 m and is bent in the horizontal plane with a radius of 200 m. A micro channel is constructed of ^{58}Ni-coated glass sheets of 1 mm thickness and two 1 mm spacers. Due to total reflection thermal neutrons follow the curved channel. ^{58}Ni is used because of its high scattering-length density (see table 2.1) resulting in a smaller cutoff wavelength [31]. Because of the channel curvature gamma radiation and epithermal or fast neutrons are scattered or absorbed in spacers and glass sheets. If scattered further they are absorbed in the surrounding shielding. The total beam intensity, φ_t is 3.0 $\times 10^7$ cm^{-2}s^{-1}. The neutron flux distribution, $\psi(\lambda)$ is shown in fig. 3.3. The maximum neutron flux at a wavelength of 0.160 nm is 2.3 $\times 10^8$ s^{-1}cm^{-2}nm^{-1}. For a wavelength of 0.8 nm the transmitted neutron flux is still 10^6 s^{-1}cm^{-2}nm^{-1}. The diver-

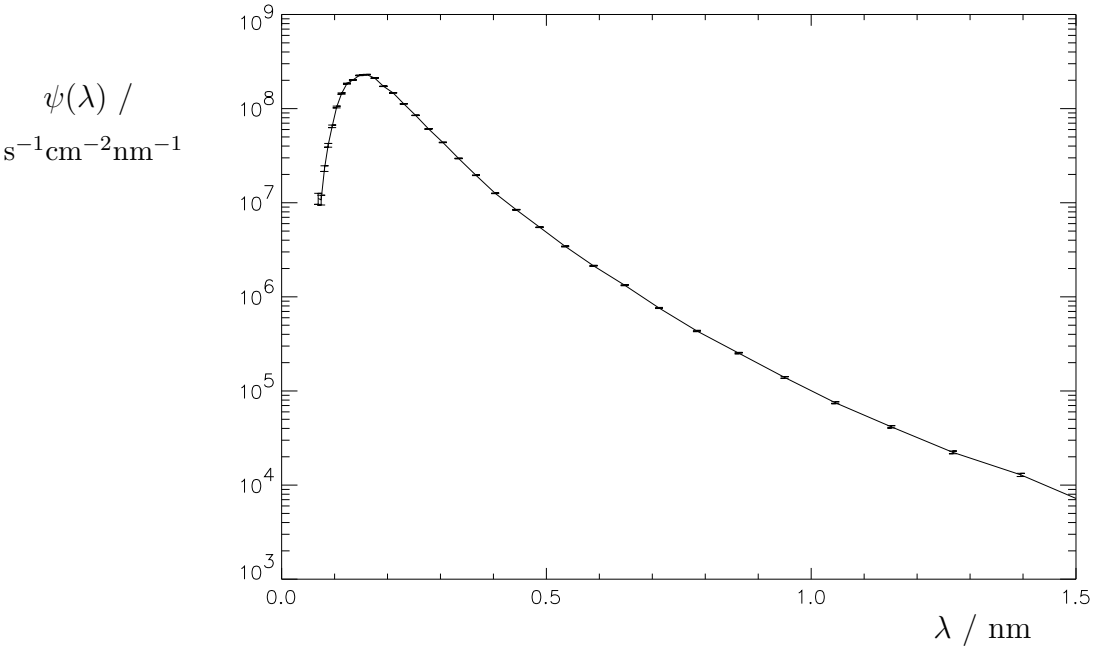

Figure 3.3: *Neutron flux distribution, $\psi(\lambda)$ at the exit of the SNG.*

gence of the beam is determined by geometry. α_v and α_h are the full widths at half maximum of the beam divergences in the vertical and horizontal plane respectively. Due to the properties of the SNG α_v is for all practical purposes 0.020 radians. For large wavelength α_h is proportional to the wavelength and is given by $\alpha_h = 0.040\lambda/\lambda_o$ radians, $\lambda_o = 1$ nm. Exact expressions for α_h and α_v are given in [30]. The gamma intensity at the exit of the SNG is 1700 cm^{-2}s^{-1}, corresponding to a dose equivalent rate of 800 μSv/h. The epithermal and fast neutron intensity is 180 cm^{-2}s^{-1}, corresponding to a dose equivalent rate of 100 μSv/h. Hence the beam emerging from the SNG is a 'clean' neutron beam.

3.4 Short frame

3.4.1 Coarse collimator

The neutron beam cross section is reduced in size by a coarse collimator. The collimator is made of two 10 cm high and 18 cm long Pb blocks. Two plates of 5 mm thick $^6Li_2CO_3$ are mounted in front of the Pb blocks (upstream the neutron beam) to absorb the unwanted neutrons. Pb reduces the intensity of the gamma radiation in the beam. The slit height of this collimator can manually be adjusted between 0 and 15 mm and is typical approximately 3 mm. The beam width is 27 mm.

3.4.2 Monitor 1

The intensity of the reduced beam is measured by monitor 1. This is an LND3000 fission chamber with an efficiency of $3.9(3) \times 10^{-4}\lambda/\lambda_o$ and an absorption of $0.122(6)\lambda/\lambda_o$, with $\lambda_o = 1.0$ nm. The thickness is 19 mm and the sensitive area is 70 mm in diameter. It is used to monitor the reactor intensity.

3.4.3 Double-disk chopper

The double-disk chopper is used to create a pulsed neutron beam with a pulse length proportional to the wavelength of the neutrons [32]. The chopper disks

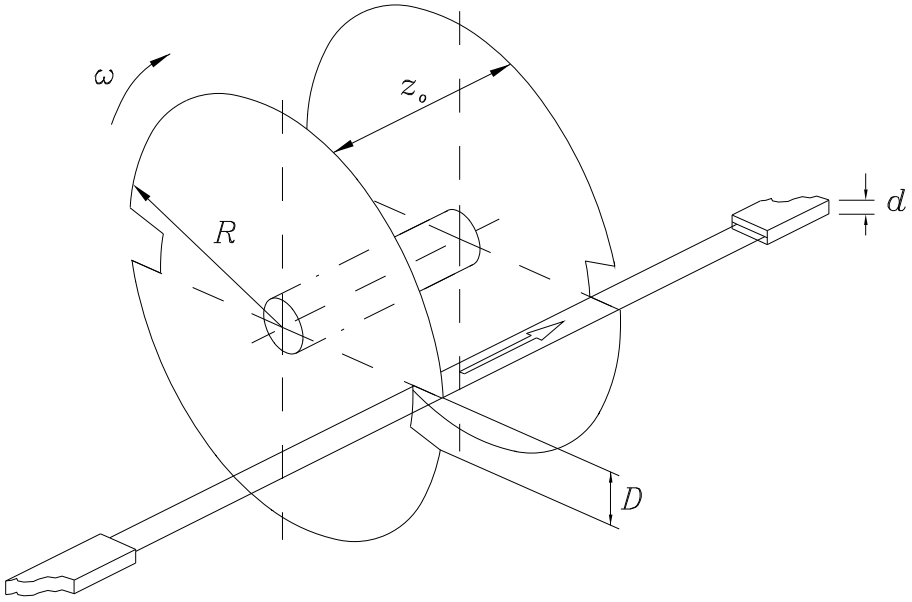

Figure 3.4: *Sketch of the double-disk chopper.*

(thickness 6 mm, diameter 400 cm) can endure the large centrifugal forces on the disk resulting from the high speed of rotation (up to 20000 rpm). Each disk was constructed of several layers of carbon-fiber-reinforced grids held in an epoxy, in

which boron (^{10}B enriched) powder was distributed as a neutron absorber. The layers were melted under high pressure to create one strong plate. In each disk two open sections of 30 degrees were made. The disks are mounted such that the two open sections in the disks are shifted 30 degrees relative to one another as shown in fig. 3.4. It can be shown that, for the wavelengths $\lambda < h/12m_n z_o f_c$,

$$\Delta t_c = \frac{m_n}{h} z_o \lambda \quad , \tag{3.7}$$

where $z_o = 200$ mm is the distance between the two disks and f_c the chopper frequency. The transmission of the chopper is given by

$$T_c(\lambda) = 2 f_c \Delta t_c = 2\frac{m_n}{h} f_c z_o \lambda \quad , \tag{3.8}$$

where the factor of 2 is due to the number of pulses in one revolution of the chopper.

The neutron attenuation of the disks must be very high to suppress the time (i.e. wavelength) dependent background countrate. The neutron beam is absorbed by only one disk during 1/3 of a revolution because the disks contain two holes of 30 degrees. If the attenuation of one disk is not sufficient, a time dependent neutron intensity remains. Considerable effort was taken to enhance the attenuation as much as possible. After the first tests the attenuation of the plates appeared to be too small. It was decided to add 16 layers of paint mixed with Gd_2O_3. Measurements show that for neutrons with wavelengths larger than 0.1 nm the attenuation is sufficiently high. Neutrons with wavelength smaller than 0.1 nm cause a (relatively) small time-dependent background, which in most cases can be ignored.

3.5 Beam definition

3.5.1 Diaphragms

The geometry of the neutron beam is defined by two diaphragms with their centers positioned at 150.0 mm above the surface of the long frame. The distance between the diaphragms, L_{12} is 3000 mm. The widths, w_1 and w_2 of the diaphragms can be adjusted between 0 and 30 mm, and the heights, d_1 and d_2 between 0 and 10 mm. The intensity distribution along the sample depends on the setting of the diaphragms, the angle of reflection, the distance between the diaphragms and the distance between diaphragm 2 and the middle of the sample ($L_{2S} = 405$ mm). Because of the small beam divergences and cross sections considered here, the source can be assumed isotropic and homogeneous. Then, the intensity distribution perpendicular to the beam (i.e. the vertical direction) at the sample position has a trapezium shape. If the center of the trapezium is considered to be at the $x = 0$ position, then the edges x_1 and x_2 (shown in fig. 3.5) are given by:

$$x_1 = (d_1 - d_2)L_{2S}/2L_{12} + d_2/2 \qquad x_2 = (d_1 + d_2)L_{2S}/2L_{12} + d_2/2 \quad , \tag{3.9}$$

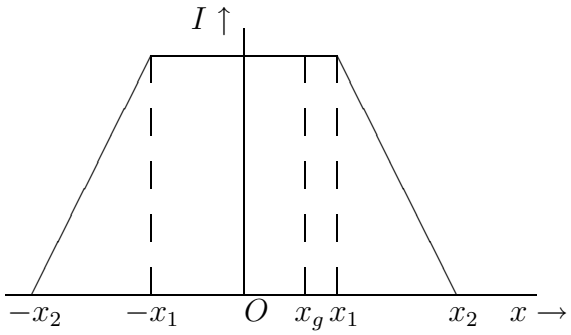

Figure 3.5: *Neutron intensity distribution perpendicular to the beam (see text).*

as long as $x_1 > 0$. As soon as $x_1 \leq 0$ the trapezium reduces to a triangle with a base from $-x_2$ to x_2. These calculations do not take into account the gravity effect. To emphasize this, the integral intensity of the trapezium I_0, measured as a function of wavelength, was compared with a measurement where only the intensity of the profile from x_g to x_2, I_1 was measured. The ratio I_1/I_0 is shown

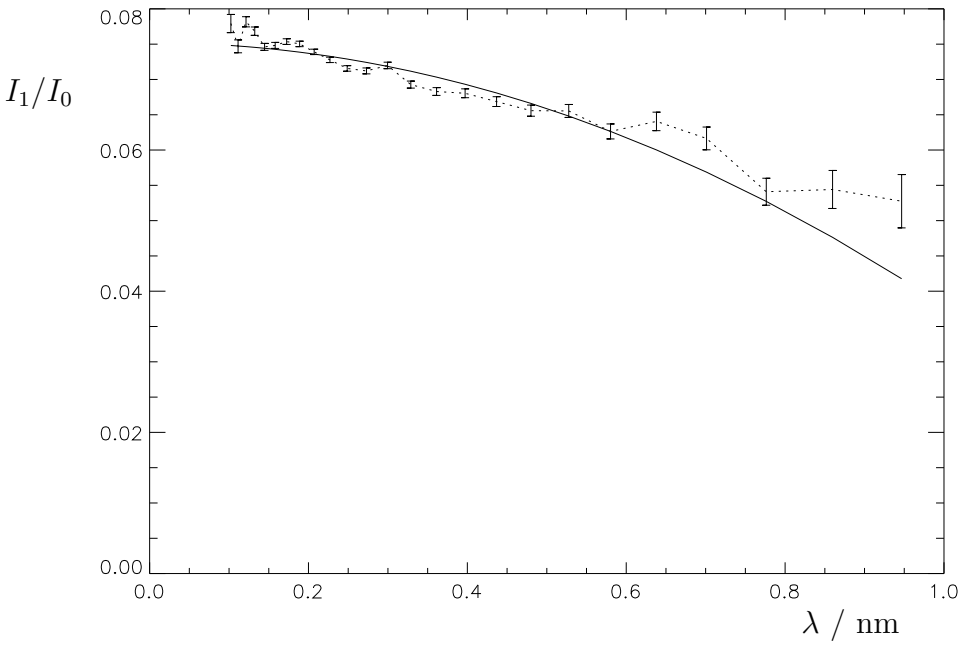

Figure 3.6: *Ratio of upper part of profile intensity to total profile intensity, I_1/I_0 as a function of wavelength as measured (error bars) and according to theoretical calculations (full line).*

in fig. 3.6 with error bars. The full line represents the theoretical expectation, due to the shape of the profile and the falling of the neutrons as given by

$$\frac{I_1}{I_0} = \tau(1 - \frac{\lambda^2}{\lambda_g^2}) \quad , \tag{3.10}$$

where τ and λ_g are calculated from the shape of the profile and the dimensions of the setup. As long as $x_g < x_1$

$$\tau = \frac{1}{2} - \frac{x_g}{x_2 - x_1} \quad \text{and} \quad \lambda_g = \sqrt{\frac{2H_o\lambda_o^2(x_2 + x_1 - 2x_g)}{(L_{12} + L_{2S})L_{2S}}} \quad , \tag{3.11}$$

where H_o is 8 km and λ_o 1.0 nm as given in appendix B. For these measurements d_1 was 0.85(1), d_2 1.06(1) and x_g 0.505(5) mm, yielding x_1=0.544(13), x_2=0.659(13), τ = 0.080(10) and λ_g=1.50(9) nm. The theoretical expectation and the fit to the measurement (τ = 0.0752(8); λ_g=1.42(13) nm) agree very well, although the effect is extremely small. Only with the extreme setting as used in this experiment it can be shown. For ROG falling neutrons are of importance only for small samples (less than 1 cm) and large wavelengths (larger than 0.5 nm) and can usually be ignored (see appendix B for detailed information).

The total beam intensity integrated over all wavelengths, I_t is given by:

$$I_t = T_t\varphi_t d_1 T_V w_1 T_H \quad , \tag{3.12}$$

where $T_V = d_2/\alpha_v L_{12}$ and $T_H = w_2/\alpha_h L_{12}$. If T_V or T_H are larger than 1 they must be replaced by 1. The average wavelength of the neutrons is 0.226 nm so the average of α_h is 9.2×10^{-3} radians. The effect of the neutron guides (see section 3.5.4) between chopper and sample is neglected in these calculations. The factor T_t takes into account the transmission of chopper and flightpath. The intensity as a function of the incident angle on the sample is shown in fig. 3.7. The spread in incident angles on the sample is given by the standard deviation

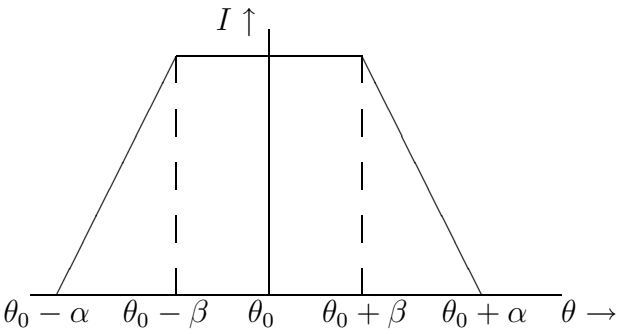

Figure 3.7: *Neutron intensity as a function of incident angle,* $\alpha = (d_1 + d_2)/2L_{12}$ *and* $\beta = \mid (d_1 - d_2)/2L_{12} \mid$.

$$\sigma_\theta = \frac{1}{L_{12}}\sqrt{\frac{d_1^2 + d_2^2}{12}} \quad . \tag{3.13}$$

The sample can be over-illuminated and a part of the neutron beam will miss the sample, if the diaphragms are not correctly adjusted. At any diaphragm setting

there is a minimum reflection angle depending on the sample length or there is a minimum length depending on the reflection angle

$$\theta L_{min} \approx d_2 + \frac{L_{2S}}{L_{12}}(d_1 + d_2) \quad , \tag{3.14}$$

if $\sigma_\theta/\theta \lesssim 0.1$. This is shown in fig. 3.8. For a certain fixed relative resolution

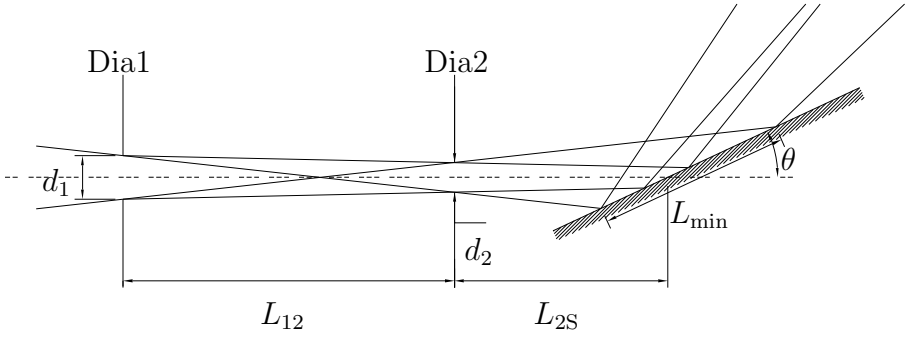

Figure 3.8: *Sketch of beam definition with diaphragms.* d_1 *and* d_2 *are the heights of and* L_{12} *the distance between the diaphragms;* L_{2S} *the distance between the second diaphragm and the middle of the sample;* L_{min} *the length of the footprint of beam on sample and* θ *the incidence angle.*

$\rho = \sqrt{12}\sigma_\theta/\theta$, the heights of the diaphragms can be optimized. Therefore reduced variables are introduced:

$$\begin{aligned} d_2^* &= d_2/\rho\theta L_{12} \quad , \\ d_1^* &= d_1/\rho\theta L_{12} \quad , \\ L_{min}^* &= L_{min}/L_{12}\rho \quad , \\ \hat{I}_t &= \frac{T\varphi_t}{2}\frac{w_1 w_2}{\alpha_v \alpha_h}(\theta\rho)^2 \quad . \end{aligned} \tag{3.15}$$

Now eqs. (3.13) and (3.12) become:

$$\begin{aligned} (d_1^*)^2 + (d_2^*)^2 &= 1 \quad , \\ I_t &= 2\hat{I}_t d_1^* d_2^* \quad , \\ L_{min}^* &\approx d_2^* + \frac{L_{2S}}{L_{12}}(d_1^* + d_2^*) \quad . \end{aligned} \tag{3.16}$$

The reduced quantities are shown in fig. 3.9 as a function of d_2^*. There is a maximum in the total intensity, $\hat{I}_t$ for $d_2^* = d_1^* = 2^{-\frac{1}{2}}$ which is proportional to the square of $\rho\theta$. If the sample length is less than L_{min} fig. 3.9 indicates the optimal settings of the height of the diaphragms.

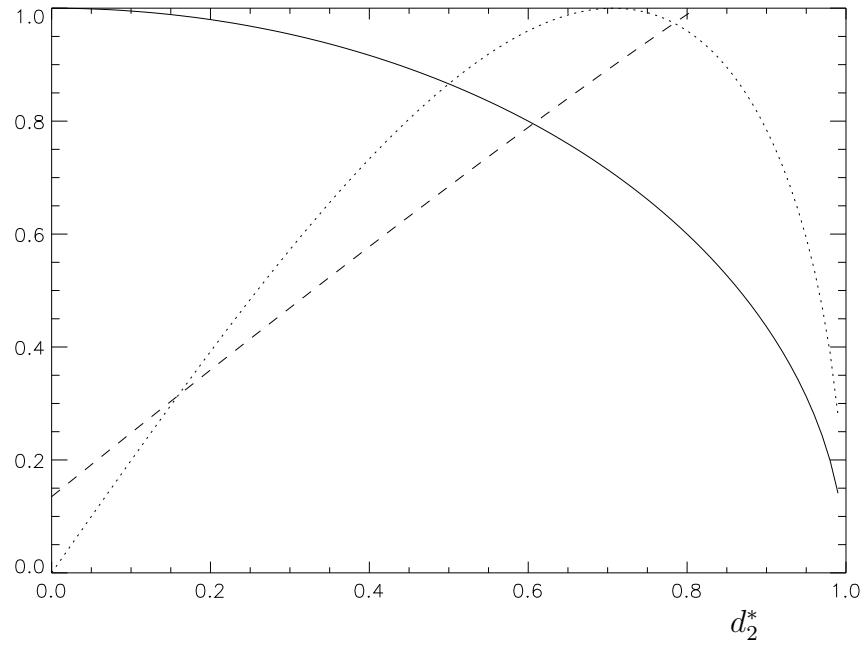

Figure 3.9: *Graph of some reduced quantities as a function of* d_2^*. $I_t/\hat{I}_t$ *(dotted line);* d_1^* *(full line) and* L_{min}^* *(dashed line).*

3.5.2 Super mirror

The super mirror (SUMI) is used to polarize and/or deflect the beam. It consists of three optically-flat glass substrates with a length of 60 cm. One of the substrates is not coated, the two others are coated by O. Sch¨arpf, (ILL/France) [33]. The different coatings result in different properties:

a No coating. The neutrons of both spinstates are reflected at the surface for $q \leq 0.066$ nm^{-1} .

b Non-magnetic super-mirror coating. The coating consists of a series of Ni/Ti bilayers with varying thicknesses. The two layers are made of materials with a large difference in scattering-length density. In this way the region of total reflection can be extended to larger q [33], [34]. The neutrons of both spinstates are reflected at the surface for $q \leq 0.20$ nm^{-1}. In fig. 3.10 the reflectivity of the super mirror as a function of wavelength is shown. The incident angle was 0.01 radians. The reflectivity drops off at $\lambda = 0.31$ nm, which corresponds to $q = 0.20$ nm^{-1}. This is in agreement with the reflectivity as reported by Sch¨arpf [33]. For comparison the cut-offs of glass, Ni and ^{58}Ni are given by arrows.

c Magnetic Co/Ti super-mirror coating. The neutrons of one spinstate are reflected at the surface for $q \leq 0.20$ nm^{-1}, and of the other spinstate are reflected for $q \leq 0.01$ nm^{-1}, so that a polarized neutron beam can be created, keeping the available wavelength range in mind.

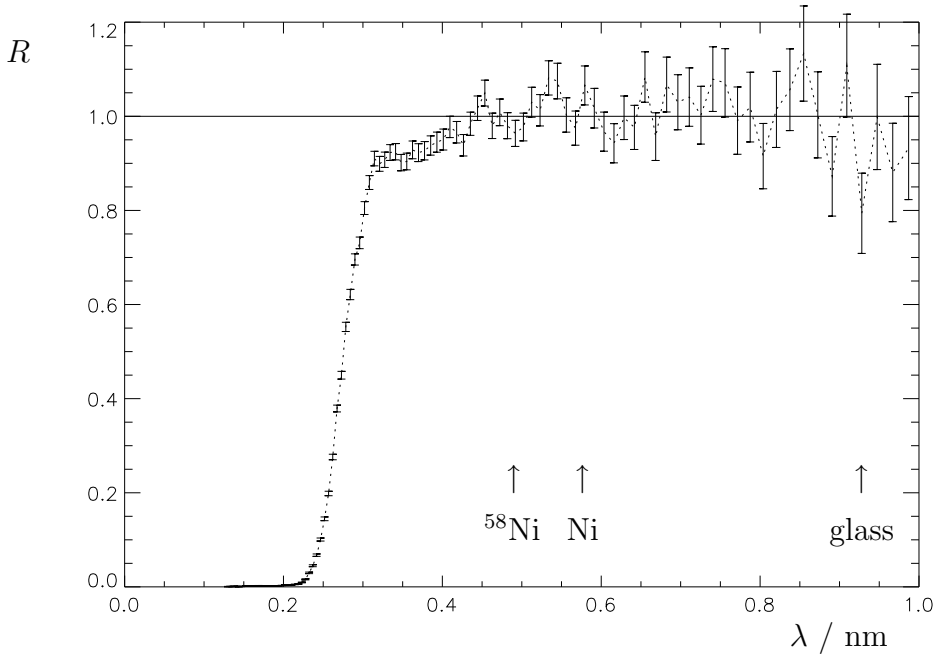

Figure 3.10: *Measured reflectivity of a non-magnetic super mirror, R as a function of wavelength. The incidence angle was 0.01 radians. The arrows represent the total reflection cut-offs for glass, Ni and ^{58}Ni.*

The lower limit of the neutron wavelength spectrum is determined by the super mirror and the used glancing angle

$$\lambda_{min} = \frac{2\pi\theta_{SUMI}}{q_{c,SUMI}} \quad . \tag{3.17}$$

3.5.3 Frame-overlap mirror

The frame-overlap mirror (FOMI) is used to reflect unwanted large-wavelength neutrons out of the beam. It consists of three 0.5 mm thick silicon plates coated with Ni. One silicon plate is made of 5 silicon wafers grown in the (111) direction. The total length of the plates is 55 cm. Neutrons of both spinstates are reflected out of the beam for $q \leq q_{c,FOMI} = 0.109$ nm^{-1}. Neutrons which are not reflected are transmitted through the silicon. In fig. 3.11 the transmission of the frame-overlap mirror as a function of wavelength is shown. The incident angle was 0.012 radians (diamonds) and -0.012 radians (crosses). The cut-off at large wavelength is clearly visible. Within statistical accuracy the transmitted intensity is zero. The cut-off for positive and negative incident angles is different. This can be due to an offset in the setting of the incident angle of approximately 5×10^{-4} radians. It is also possible that the three silicon plates are not exactly parallel. The cut-off at small wavelength is caused by the super mirror, which was positioned in the incident beam with an angle of 4.3×10^{-3} radians to reduce the background countrate resulting from the chopper (see section 3.4). The structure

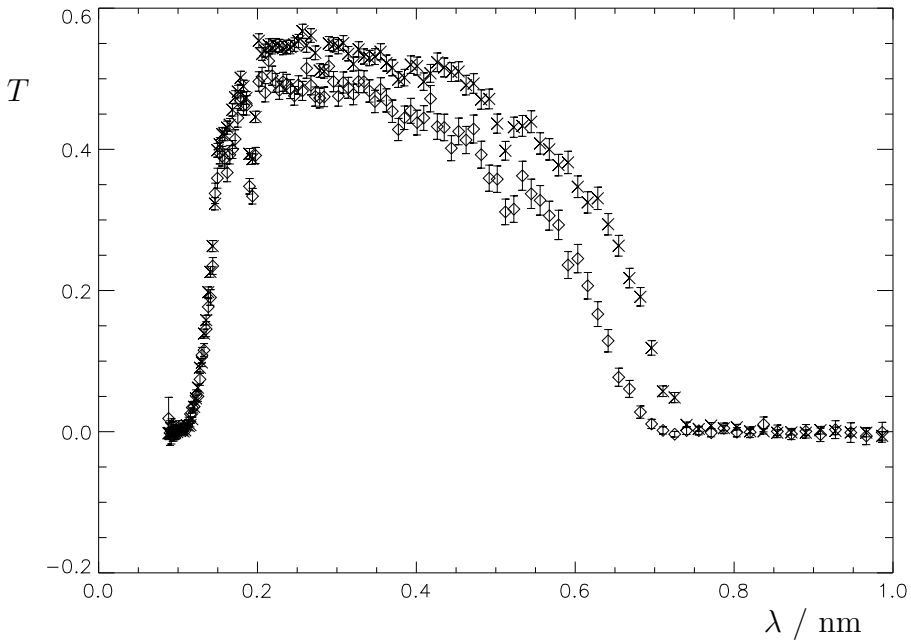

Figure 3.11: *Measured transmission of the frame-overlap mirror, T for different angles of the mirror in the beam: 0.012 radians (diamonds) and -0.012 radians (crosses).*

in the transmission is the result of the adsorption and scattering of neutrons by the silicon. The direction of the neutron beam is approximately perpendicular to the [111] direction. Bragg-reflection can occur for the (220) and (440) planes or for the (422) planes. The dip at $\lambda = 0.192$ nm is possibly caused by the (440) Bragg-reflection. The transmission of the silicon plates is given by

$$T_{Si} = \mathrm{e}^{-\mu_{Si}(\lambda) d_{Si}/\theta_{FOMI}} \ , \tag{3.18}$$

where d_{Si} is the total thickness of the plates, θ_{FOMI} the angle of the frame-overlap mirror in the beam and $\mu_{Si}(\lambda)$ the linear attenuation coefficient, shown in fig. 3.12. To calculate the transmission of the frame-overlap mirror for wavelengths larger than 0.2 nm, $\mu_{Si}(\lambda)$ can be modelled as shown in fig. 3.12 by

$$\mu_{Si}(\lambda) = 3.8 + 6.9\lambda \quad \mathrm{m}^{-1} \ , \tag{3.19}$$

where λ is the wavelength in nm. The measured transmission of the frame-overlap mirror at 0.012 radians was corrected for the attenuation by the silicon plates as shown in fig. 3.13. The solid line represents a theoretical calculation of the transmission of the frame-overlap mirror, which is given by the Fresnel transmission of a Ni substrate. The divergence of the beam was $5{\times}10^{-4}$ radians. The measured transmission corresponds very well to the theoretical calculation.

The upper limit of the neutron wavelength spectrum is determined by the frame-overlap mirror

$$\lambda_{max} = \frac{2\pi\theta_{FOMI}}{q_{c,FOMI}} \ . \tag{3.20}$$

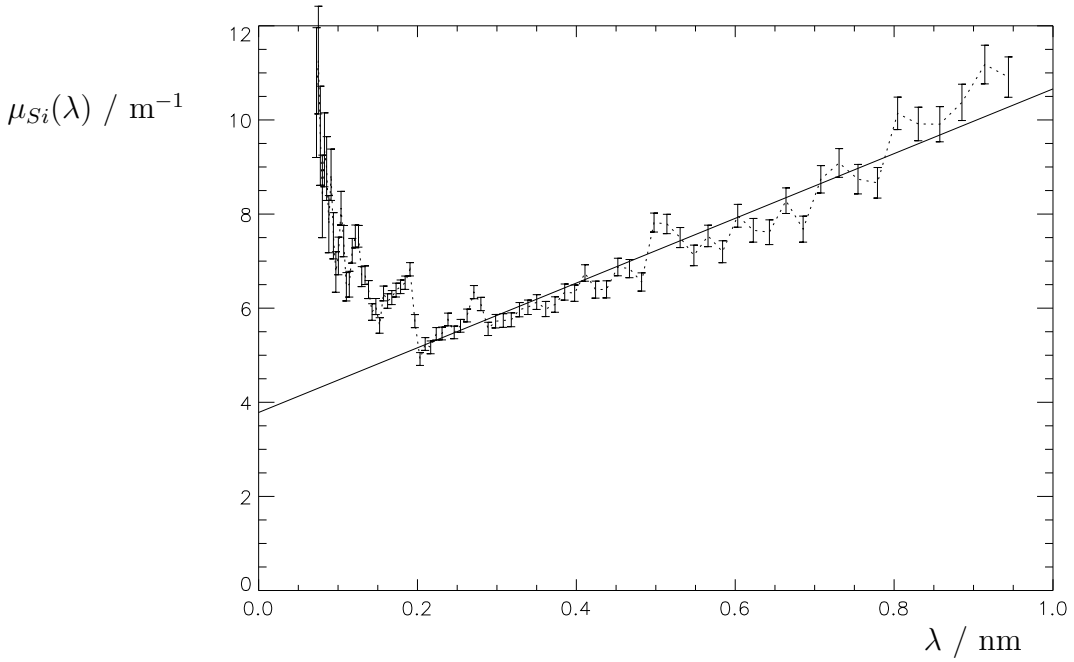

Figure 3.12: *Linear attenuation coefficient of silicon plates, $\mu_{Si}(\lambda)$ as a function of wavelength as measured (error bars) and as calculated from a useful model (see text) for large wavelength (line).*

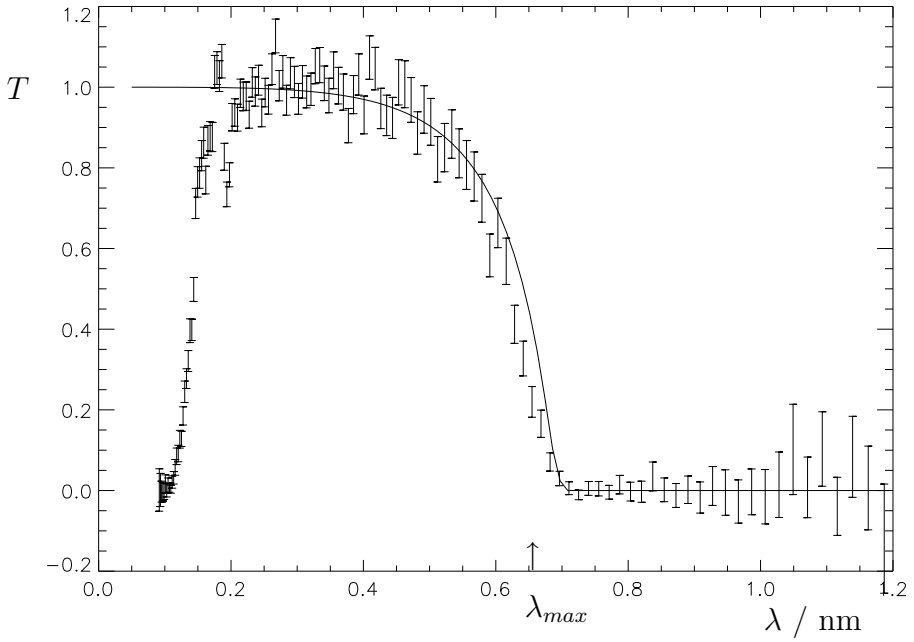

Figure 3.13: *Measured transmission of the frame-overlap mirror at an angle of 0.012 radians in the beam after correction for the transmission of the silicon plates (error bars), compared with the theoretical calculation (solid line).*

3.5.4 Neutron guides

Two neutron guides are used to confine the beam in the horizontal direction to reduce the loss of neutrons due to the horizontal divergence of the beam. They are made of glass plates coated with ^{58}Ni at the vertical surfaces. The length of both guides is 1.05 m. The width is 30 mm. Coated glass plates are also mounted along the frame-overlap mirror and the super mirror. These neutron guides as well as the super mirror and frame-overlap mirror are supplied by NTK, Wörishofen, Germany. The distance from the exit of SNG (width 27 mm) to the sample position is 5 m. The total length of the neutron guide (width 30 mm) is 3.25 m. The transmission of ROG taking into account only the horizontal divergences is calculated using ray-tracing techniques as discussed in [35]. This transmission is defined as the number of transmitted neutrons divided by the number of neutrons emerging from the SNG. In fig. 3.14 this transmission is shown as function of wavelength for the situation with (full line) and without (dashed line) neutron guides. The diaphragms were both set on a width of 30 mm. For wavelengths larger than 0.5 nm the gain is almost a factor of four! Due to the smaller divergence of the beam emerging from the SNG the transmission at shorter wavelengths is larger in both cases. The structure in the lines is due to inaccuracies in the calculations.

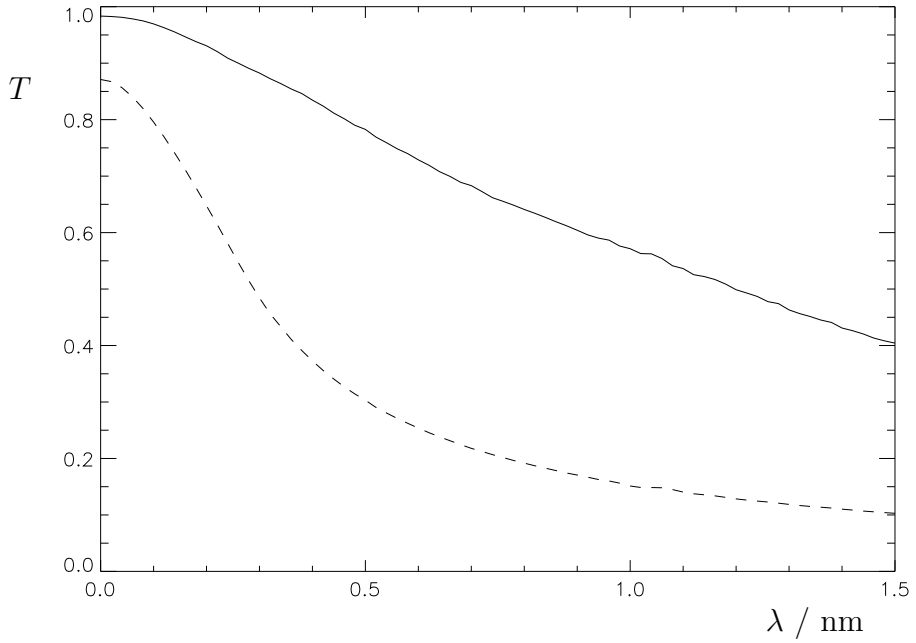

Figure 3.14: *Simulated transmission of ROG as a function of wavelength. Only the horizontal divergence with (full line) and without (dashed line) neutron guides has been taken into account.*

3.5.5 Spin flipper

A neutron spin flipper [36] is used to change the polarization of the neutron beam from parallel into anti-parallel to the magnetic induction. It is based on the principle of adiabatic rotation. The neutron flipper consists of two coils, that are each others mirror images (see fig. 3.15). The coils are open at one side. Entering the left coil the magnetic induction in the x direction increases slowly while the neutron moves along the z direction. While passing the wire sheets in the middle of the spin flipper the induction will remain constant or change direction depending on the currents through the coils. In this way an abrupt change in the magnetic induction can be introduced by changing the direction of the current in the second coil compared to the first one. The neutron

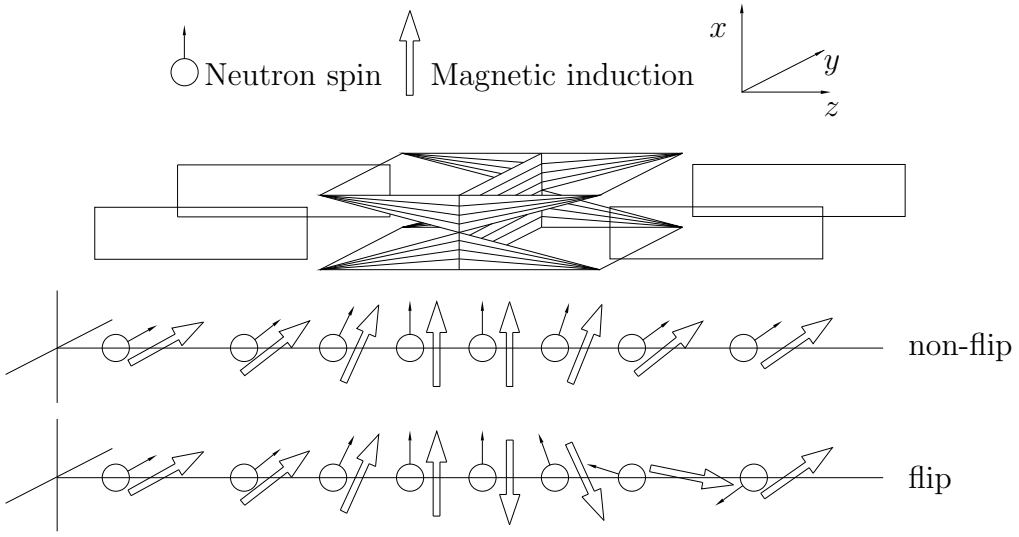

Figure 3.15: *Principle of an adiabatic spin flipper.*

spin direction adiabatically follows the changes in the direction of the magnetic induction, if changes in the induction are small compared to the Larmor frequency, i.e. the neutron spin precesses many times before a considerable change in the direction of the magnetic induction occurs. So, if the change in the magnetic induction is fast enough the neutron spin cannot follow this change and remains in approximately the same direction. After this fast magnetic induction change the neutron spin again adiabatically follows the slow change in the magnetic induction. The result is a 'flip' of the neutron spin. Magnetic guide fields are created by permanent magnets placed along the neutron guides from polarizer to sample environment. They are used to avoid depolarization of the neutron beam.

3.5.6 Monitor 2

Monitor 2 is a XERAM 4 MNH 10/4.2 9% ^{3}He counter and is used for the determination of the incident wavelength spectrum. The active thickness of the

monitor is 40 mm. The sensitive area is 100 × 42 mm, large enough to cover the incident neutron beam. The efficiency for 0.18 nm neutrons is approximately 9 %. The monitor is coupled to an amplifier with a dead time of approximately 10 μs. The pulses from this amplifier are analyzed by a time-of-flight analyzer, consisting of a time-coding and data handling module (TCOD/DHM) and a dual ported memory module (DPM) (see section 5.1).

3.6 Sample compartment

Neutrons enter and leave the sample compartment through valves, that can be opened and closed pneumatically. During a measurement the valves will be opened so neutrons can pass unhindered. When the atmospheric conditions in either the beam definition-, sample- or detector compartment are changed, the valves are closed. The sample is mounted on a twofold rotation stage to adjust both the incident angle and rotation of the sample plane around the neutron beam (rotations around the y-axis and z-axis respectively), and a translation stage to adjust the height of the sample in the beam. This translation stage can be mounted on a vibration-isolation table (type MOD-2, JRS, Switserland), which reduces the transmitted vibrations with at least a factor of 100 (depending on the frequency). For magnetic measurements it is possible to use a water-cooled electromagnet (with a maximum induction of 1 T).

3.7 Detection

The distance between sample and detector can be chosen between 1 and 2 m. Detected neutrons are counted by a multi-channel time-of-flight analyzer. In each channel neutrons with a time of flight within a specific time interval are counted. These time intervals are user-adjustable. The optimal width of the time channels, Δt_i can be chosen to be proportional to the time of flight of the neutrons counted in that channel, in order to match the resolution contributions in eqs. (3.3) and (3.7)

$$\frac{\Delta t_i}{t_{TOF}} \approx \frac{z_0}{L_{TOF}} \quad . \tag{3.21}$$

The time channel widths can be adjusted with discrete steps of 2 μs and have an accuracy of 0.1 μs. For the monitor 2 or single detector 256 channels of 4 bytes are available. For the position-sensitive detector 256×256 channels of 2 bytes are available (see also section 5.2).

The shielding diaphragm between the sample and the detector consists of two 5 cm thick, 10 cm wide and 15 cm high Pb blocks, with boron rubber and BN plates in front of it. It is used to absorb neutrons and gamma radiation in the transmitted beam and unwanted neutrons scattered from the sample (e.g. non-specularly reflected neutrons) and its environment in the direction of the detector. A computer controls the adjustment of the diaphragm position.

For detection either a single detector or a position-sensitive detector, both mounted on an x, y, z translation stage, are available. The single detector is a XERAM 30NH15 1 inch detector filled with 6 bar ^{3}He with its axis horizontal and perpendicular to the beam. Its sensitive length is 150 mm. The PSD consists of a position-sensitive photomultiplier with a 100 mm diameter photocathode (Hamamatsu R3292) and a ^{6}LiI(Eu) scintillator (3 inch diameter), and is described fully in the next chapter. The influence of the efficiency is discussed in section 5.2.5. An adjustable diaphragm in front of the detector (of the same type as described in section 3.5.1) reduces the intensity of unwanted neutrons. The neutrons are detected and processed in the same way as for monitor 2.

The beamstop is used to absorb all remaining radiation in the through-going beam for all possible settings of the long frame. It consists of a 5 mm thick 200 $\times$ 300 mm^2 boron rubber slab inside a 50 mm thick Pb shielding of 400 $\times$ 500 mm^2 area.

3.8 Translations and rotations

The translations and rotations of all components described above (with the exception of the course collimator) are computer controlled. The 21 movements are equipped with DC-motors and encoders. The accuracy is such that the settings of all components can be reproduced to yield overall angular uncertainties less than 10^{-4} radians.

The alignment (e.g. sample height and angle, detector height) is performed with the neutron beam itself, i.e. no laser alignment is used. The incidence angle, θ is determined by making vertical scans with the detector of both the straight beam (with no sample present), and the reflected beam. During these scans the chopper is placed outside the beam and a relatively small height of the diaphragm in front of the detector is used (see 5.2.2).

Chapter 4

Position sensitive detector[†]

Now faith is the assurance of things hoped for,
the conviction of things not seen.
For by it the men of old received divine approval.

By faith we understand that the world was created by the word of God,
so that what is seen was made out of things which do not appear.

Hebrews 11:1-3

4.1 Introduction

For ROG a position-sensitive detector (PSD) is convenient. The PSD is used to distinguish between specular, non-specular and background intensities. Because of the available space and the necessary performance, the PSD chosen for is a scintillator mounted on a 2-dimensional position-sensitive photo-multiplier, Hamamatsu R3292, with a 100 mm diameter sensitive area. The system described here is similar to the detection system used by Kurz et al. [37]. The main differences are the size of the photo-multiplier and the data handling electronics. The scintillator is made of 1.5-mm-thick ^{6}LiI(Eu) crystal or 1-mm-thick ^{6}Li glass (type GS20 or KG2). When a neutron hits the scintillator it is absorbed by ^{6}Li and an energy of 4.6 MeV is released in the form of kinetic energy of the fission reaction products ^{3}H and ^{4}He according to:

$$ {}^1_0\mathrm{n} + {}^6_3\mathrm{Li} \rightarrow {}^3_1\mathrm{H} + {}^4_2\mathrm{He} + 4.6\mathrm{MeV} \quad . \tag{4.1} $$

A small fraction of this energy is converted into light radiation of approximately 400 nm (about 2000 photons for ^{6}Li glass and 24000 photons for ^{6}LiI(Eu) crystal).

[†]This chapter is published as: 'Performance of an area scintillator detector', V.O. de Haan and A.A. van Well, SPIE **1737** (1992) 264.

A fraction of these photons hit the photo-cathode of the photo-multiplier. The anode of the photo-multiplier consists of two planes of perpendicular oriented wires, 28 $x-$ and 28 $y-$wires, connected to two resistor chains. At both ends of each chain charge pulses are created (A, B, C and D), see also fig. 4.1. These charge pulses are converted to voltage pulses with pulse heights proportional to the total charge using a shaping amplifier.

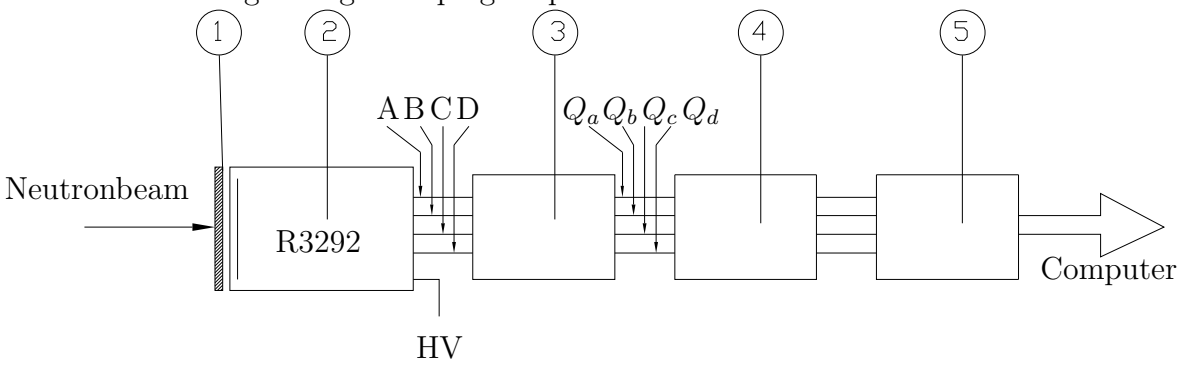

Figure 4.1: *Schematic drawing of the electronics of the PSD with scintillator (1), Photomultiplier (2), Pre-amplifier (3), Final amplifier (4) and A/D converter (5).*

4.2 Influence of shaping amplifier

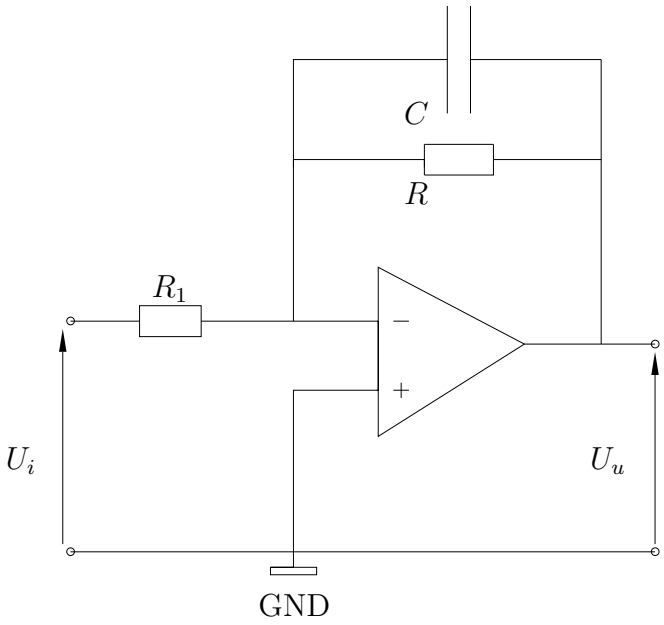

Figure 4.2: *Electric circuit of the shaping amplifier as used in the PSD. For the shaping amplifier of the PSD: $C = 4$ pF, $R_i = 1$ kΩ, $R = 234$ kΩ ... 2 MΩ.*

To optimize the PSD shaping amplifier to different scintillators its behavior must be understood. Fig. 4.2 shows the electric circuit of the shaping amplifier.

From this circuit the output voltage, $U_u(t)$ as a function of the input voltage, $U_i(t)$ is calculated:

$$U_u(t) + \tau \frac{dU_u}{dt} = -\frac{R}{R_i} U_i(t) \ , \tag{4.2}$$

where $\tau = RC$. This equation shows:

- If $t << \tau$, the shaping amplifier acts as an integrator. When $U_u(t)$ is differentiated with respect to t, the shape of $U_i(t)$ can be calculated. As long as τ is much larger than the duration of the input pulse $U_i(t)$, the maximum value of $U_u(t)$ is proportional to the number of photons produced by the scintillator.

- The maximum rise time of the output signal does not depend on R, but only on C, R_i and U_o, which is proportional to the total number of photons produced per second by the scintillator.

- The tail of the output signal is determined by τ: if τ increases the tail is longer. The tail is a measure for the "dead-time" of the shaping amplifier.

$U_u(t)$ was measured for 2 different scintillators (^{6}Li-glass KG2 and ^{6}LiI(Eu) crystal) and 4 different values of R (0.235, 0.469, 1.01, 1.99 MΩ) yielding τ = 0.94, 1.9, 4.1 and 8.0 μs respectively. To find the best approximation of the shape of $U_i(t)$, $U_u(t)$ for τ = 8.0 μs is differentiated. The results are shown in fig. 4.3.

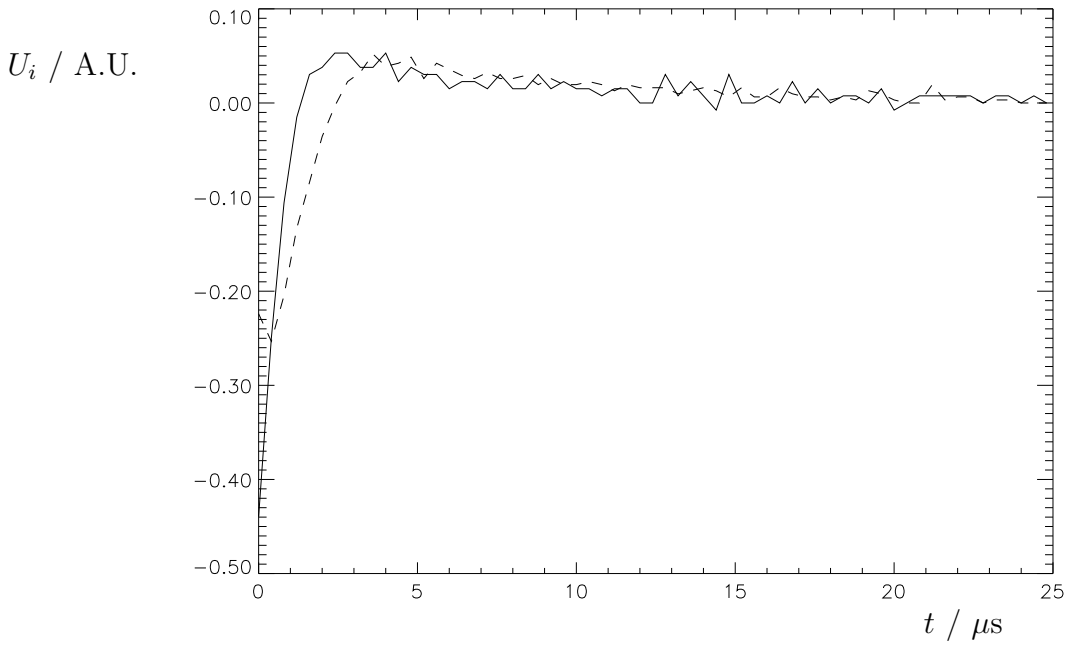

Figure 4.3: *Input voltage, $U_i(t)$ for ^{6}Li-glass (full line) and ^{6}LiI(Eu) (dashed line) scintillators as a function of t.*

The full width at half maximum (FWHM) of $U_i(t)$ for ^{6}LiI(Eu) is 1.3(2) μs. The decay time of the photon pulse is 1.4 μs, which is of the same order. The FWHM of $U_i(t)$ for ^{6}Li-glass is 0.7(2) μs. The decay time of the photon pulse is 0.1 μs, which is not of the same order. This can be due to the amplification of the photo-multiplier tube. These measurements show that the best value for τ depends on the scintillator used. A compromise between the dead-time and the accuracy of the shaping amplifier yields for ^{6}LiI(Eu) $\tau = 8$ μs and for ^{6}Li-glass $\tau = 4$ μs.

4.3 Influence of background radiation

To determine the sensitivity of the PSD for different kinds of radiation (gamma and neutron radiation) several pulse-height distribution measurements were performed. Every interaction of gamma or neutron radiation with the scintillator gives at the output of the final amplifiers a voltage pulse of a certain height, which is a measure of the number of photons detected. The pulse-height distribution gives information about the kind of interactions which occurred in the scintillator. A schematic example of a pulse-height distribution is shown in fig. 4.4.

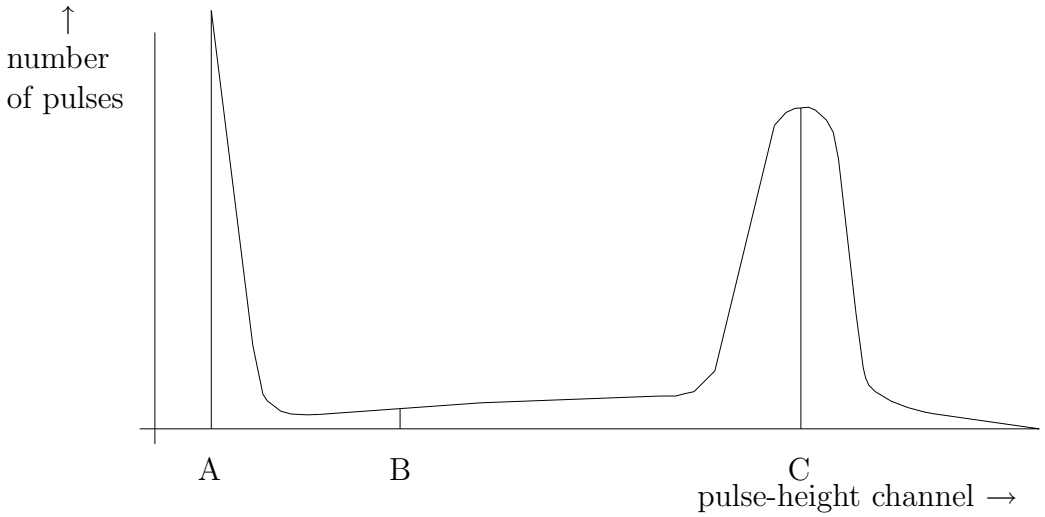

Figure 4.4: *Example of a pulse-height distribution. A, B and C are positions of characteristic channels.*

The peak at channel A is caused mainly by gamma radiation and electronic noise. The peak at channel C is caused mainly by neutron radiation. At channel B the number of counts is determined by both gamma and neutron radiation.

The gamma sensitivity is of great importance for the background countrate. The number of photons created by the gamma radiation depends on the energy of the radiation. The number of photons created by the gamma radiation is almost linear with the fraction of the energy of the gamma radiation absorbed in the scintillator. The absorbed fraction of the photon energy varies with each

interaction, but increases when the gamma energy decreases. This fraction is approximately 0.7(1) for 0.4 MeV gamma radiation and approximately 0.3(1) for 1.2 MeV gamma radiation and depends on the scintillator material and thickness. The gamma sensitivity of both scintillators was investigated by measuring the pulse-height distribution. Fig. 4.5 shows the pulse-height distribution of the LiI(Eu) crystal. The full line in fig. 4.5 represents the pulse height distribution when mainly neutrons are detected. The dashed and dotted lines represent the pulse-height distribution for gamma radiation of 1.2 MeV and 0.4 MeV respectively. All pulse-height distributions were normalized to 10^6 interactions. The sudden drop for small pulse heights is caused by a general lower discrimination level, set on approximately 50 A.U. The pulse-height distribution for the higher energy gamma-radiation extends to large pulse heights. Note that the pulse heights for both gamma-radiation energies are much smaller than the mean neutron-peak pulse-height. In this way it is easy to discriminate between a neutron capture or a gamma-radiation interaction. Lower and upper discrimination levels can be used to reduce the background countrate as much as possible.

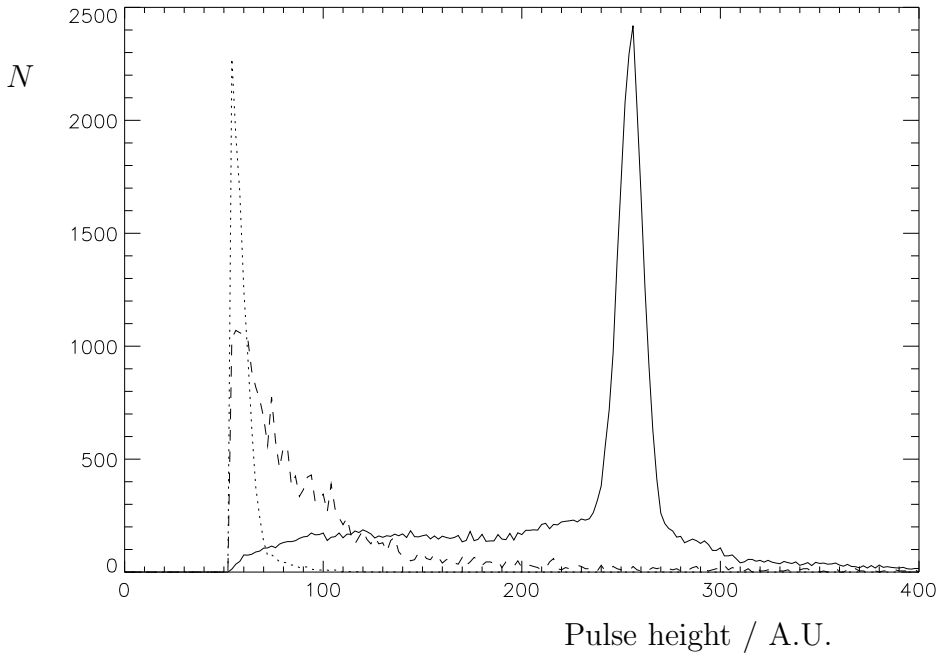

Figure 4.5: *Measured pulse-height distribution of LiI(Eu) crystal when mainly neutrons are detected (full line) and for different gamma-radiation energy's: 1.2 MeV (dashed line) and 0.4 MeV (dotted line). A general lower discrimination level was set on 50 A.U.*

Fig. 4.6 shows the pulse-height distribution of the Li glass KG2. The full line represents the pulse height distribution when mainly neutrons are detected. The dashed and dotted lines represent the pulse-height distribution for gamma radiation of 1.2 MeV and 0.4 MeV respectively. In this case a different amplification of

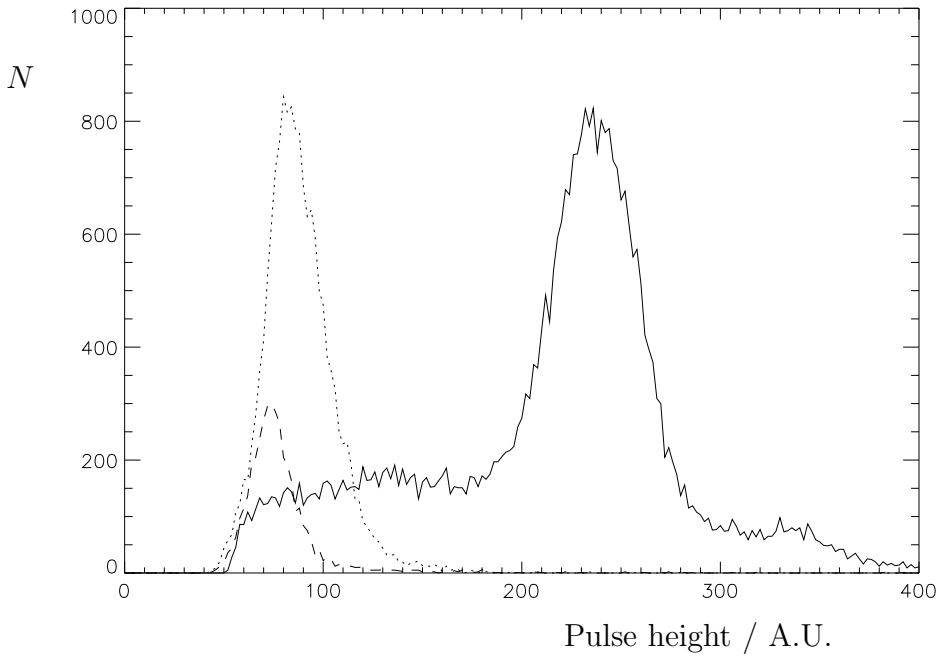

Figure 4.6: *Measured pulse-height distribution of Li glass when mainly neutrons are detected (full line) and for different gamma radiation energy's: 1.2 MeV (dotted line) and 0.4 MeV (dashed line). A general lower discrimination level was set on 50 A.U.*

the final amplifiers was used, so the horizontal scales of fig. 4.5 and 4.6 cannot be compared. Here again, the higher gamma energy results in a larger pulse height. The pulse heights for both kinds of gamma radiation are smaller than the mean neutron-peak pulse-height. However, the difference is less than in the case with the LiI(Eu) crystal. Now, it is less easy to discriminate between a neutron capture and a gamma-radiation interaction. Lower and upper discrimination levels can be used to reduce the background countrate as much as possible, but because the width of the neutron peak is larger and the gamma sensitivity is greater than in the LiI(Eu) crystal case, the reduction is not as good.

A pulse-height distribution was measured for a few configurations of shielding material around the PSD with the Li glass scintillator. The configurations of the shielding were made as a combination of at most 3 layers: an inner layer of 5 mm boron rubber, 5 cm lead and an outer layer of 5 mm boron rubber, containing 50 wt% B_4C. This is shown schematically in fig. 4.7. These measurements were done in two radiation fields A and B, which had approximately the same gamma fluxes and different neutron fluxes. The pulse-height distributions measured for radiation fields A and B (without shielding) are shown at the upper graph of fig. 4.8.

The pulse-height distributions measured for the configuration with the smallest transmission for neutron radiation for radiation fields A and B are shown at the lower graph of fig. 4.8. All pulse-height distributions were measured in

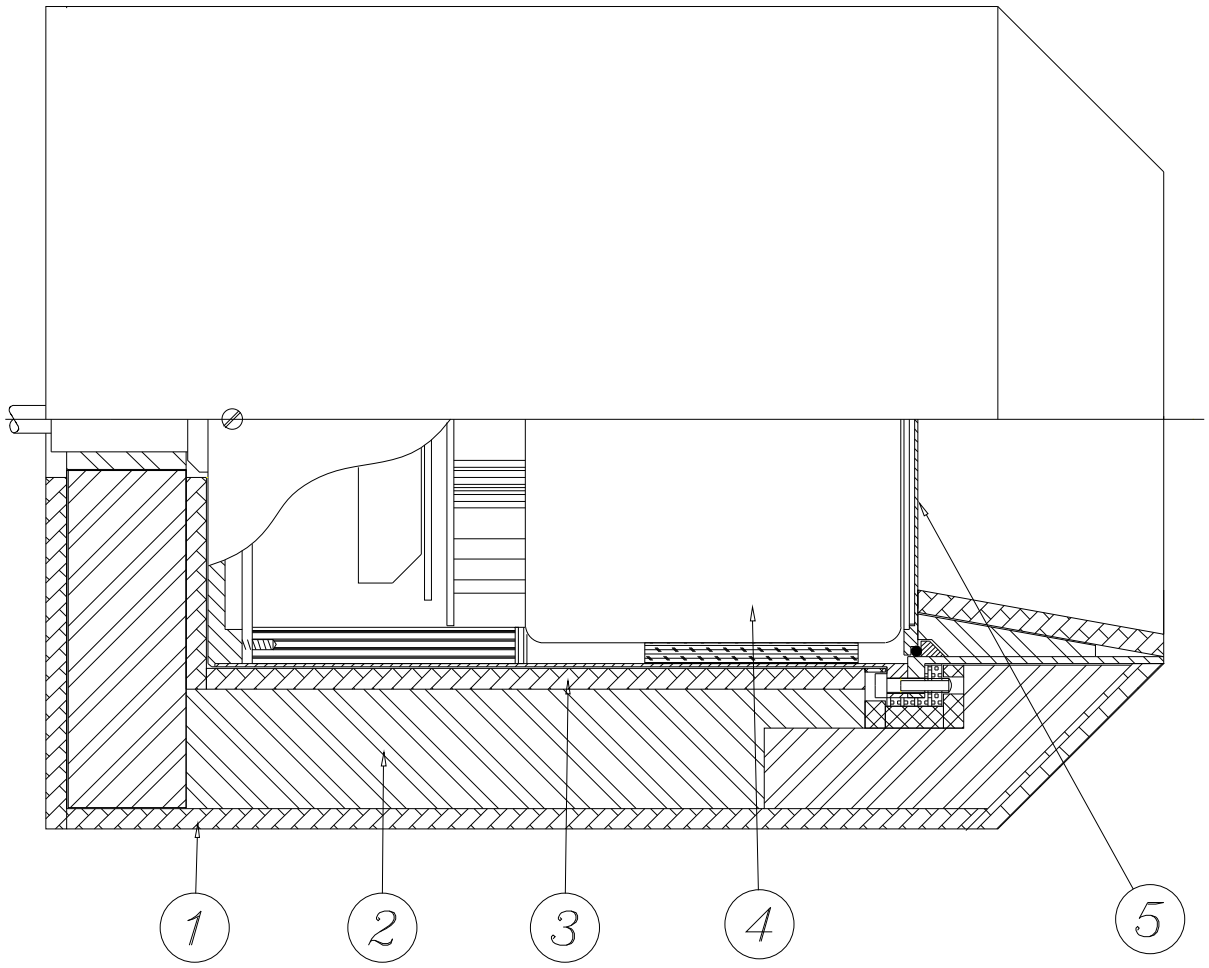

Figure 4.7: *Schematic view of the shielding around the PSD with outer 5 mm boron rubber slab (1); 5 cm lead (2); inner 5 mm boron rubber slab (3); photomultipliertube (4) and scintillator (5).*

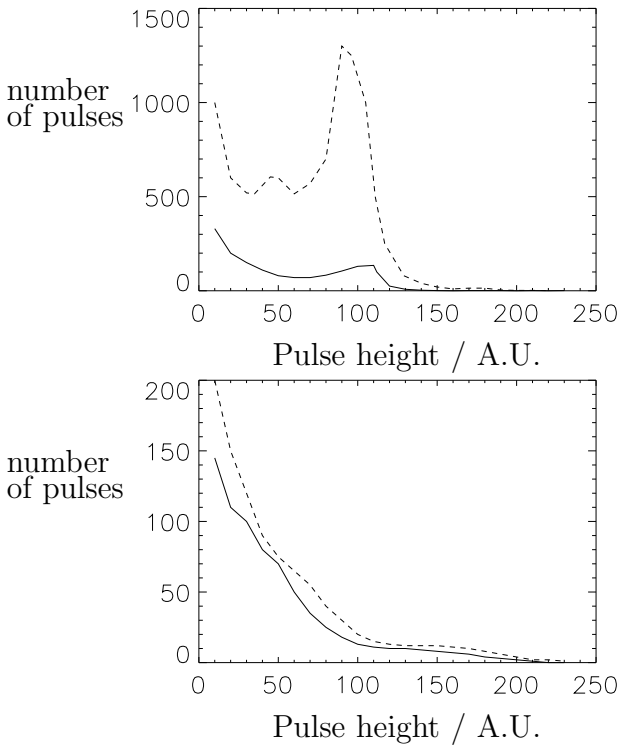

Figure 4.8: *Pulse-height distributions for the Li glass scintillator as measured with no (upper) and with best (lower) radiation shielding for radiation fields A (full line) and B (dotted line).*

3 minutes. From the measurements described above is concluded that the best radiation shielding configuration which was tested is a 5-mm-thick inner boron rubber layer, 5-cm-thick lead layer and 5-mm-thick outer boron layer.

4.4 Position determination

The position (x, y) where the light pulse was created is given by

$$(x, y) = f_{xy}(Q_A, Q_B, Q_C, Q_D) \ , \tag{4.3}$$

where $Q_A,\ Q_B,\ Q_C,\ Q_D$ are the peak values of A, B, C and D respectively. In the ideal case

$$x = \hat{x}\frac{Q_A}{Q_A+Q_B} \ , \quad y = \hat{y}\frac{Q_C}{Q_C+Q_D} \ , \tag{4.4}$$

where x varies from 0 to $\hat{x}$ and y from 0 to $\hat{y}$. This is shown in fig. 4.9.

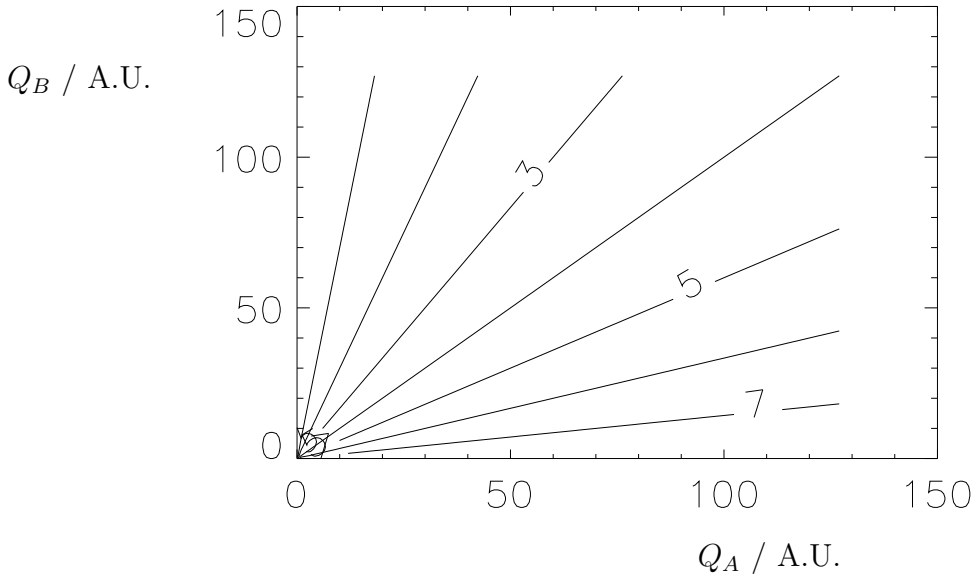

Figure 4.9: *Graph of 'ideal' detection position x of a neutron as a function of the pulse-heights Q_A and Q_B from the PSD. The lines shown are equi-x lines with x = (1 to 7) $\times\frac{\hat{x}}{8}$.*

However, because the world is non-ideal this is not the case. An approximation of this non-ideal part of the world is

$$x = f_x(Q_A, Q_B) \ , \quad y = f_y(Q_C, Q_D) \ . \tag{4.5}$$

Functions f_x and f_y ate stored in a RAM memory module in the hardware of the PSD. In this way, deviations from eq. 4.4 can be accounted for. Another advantage is that by using lookup tables, the electronic dead time is reduced considerably. However, because eq. (4.5) is an approximation of eq. (4.3) not all

non-linear behaviour can be accounted for. To determine functions f_x and f_y, a small neutron beam (ø FWHM 0.5 mm) was created to strike the PSD at a known position (x, y). An (x, y) grid of 64 by 64 positions was scanned. For each detection of a neutron Q_A, Q_B, Q_C and Q_D were measured by means of 4 8-bits ADC's. For each combination of Q_A and Q_B the mean value of x, $\bar{x}$ and the deviation of x, σ_x was determined. In this way function f_x is evaluated using a POSX table, which gives the x position for each combination of Q_A and Q_B. A representation of a POSX table is shown in fig. 4.10. Simultaneously, the same procedure was followed to produce a POSY table.

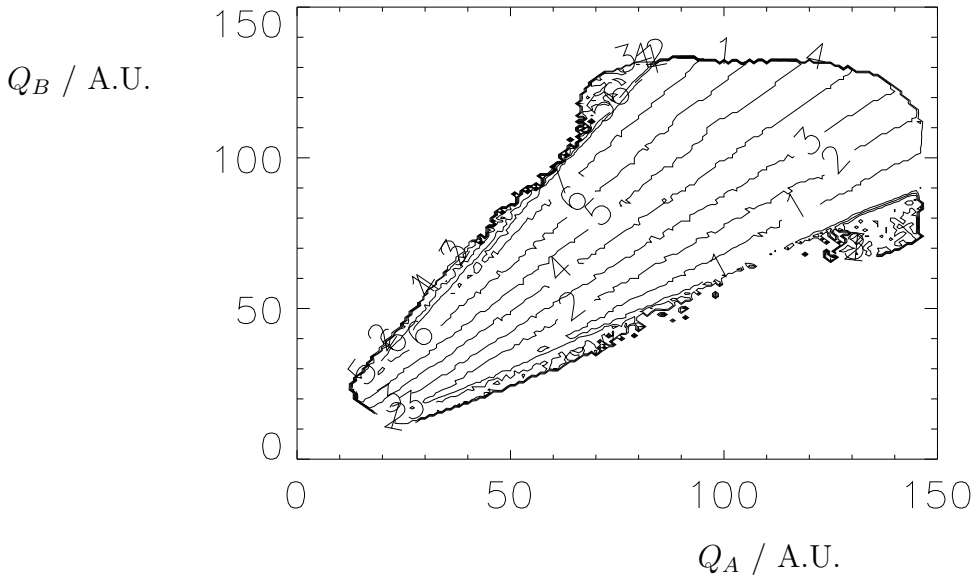

Figure 4.10: *Graph of measured detection position x of a neutron as a function of the pulse heights Q_A and Q_B from the PSD. The lines shown are equi-x lines with x = (8 - 1 to 7) $\times \frac{\hat{x}}{8}$.*

After the POSX and POSY tables were determined, the measured position of the neutron beam was compared to the actual position of the neutron beam. This is shown in fig. 4.11. At the edges of the scintillator the linearity is less, but still in the order of a few percent.

4.5 Spatial resolution

The spatial resolution of the PSD is determined by the electronics and by the combination of the used scintillator and the photo-multiplier. The main electronic resolution contributions are:

1. Fluctuations in A, B, C and D caused by noise introduced by (shaping) amplifiers.

2. Digitization of Q_A, Q_B, Q_C and Q_D during the ADC conversion.

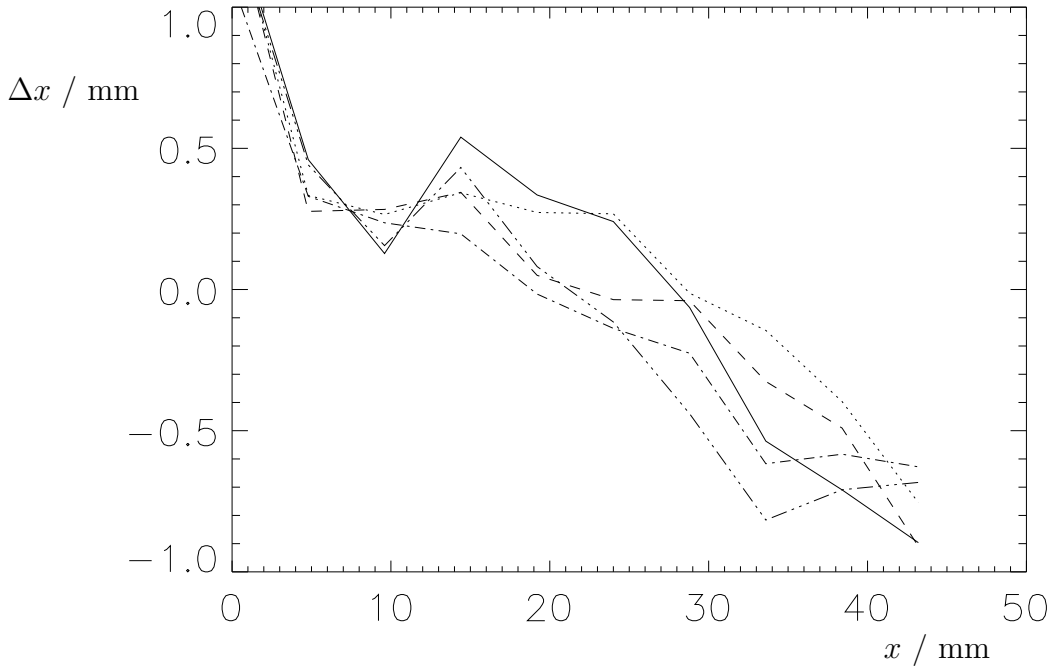

Figure 4.11: *Graph of deviation Δx of measured detection position of a neutron from the actual position x as a function of x. The lines shown are equi-y lines with $y = 0.1\hat{y}$ (full line); $y = 0.3\hat{y}$ (dashed line); $y = 0.5\hat{y}$ (dotted line); $y = 0.7\hat{y}$ (dash-dotted line) and $y = 0.9\hat{y}$ (dash-double dotted line); $\hat{y} = 4.8$ cm.*

The main scintillator resolution contributions are [37]:

1. Fluctuation of the absorption position of the neutron.
2. Fluctuation of the number of photons produced by a neutron absorption.
3. Fluctuation in the number and position of the photons which reached the cathode of the photo-multiplier.
4. Fluctuation in the number and position of the photo-electrons which reached the anode of the photo-multiplier.

In the following these contributions are discussed.

4.5.1 Electronic resolution contributions

Fluctuations in A, B, C and D caused by noise introduced by (shaping) amplifiers

Each amplifier introduces a noise signal, which does not depend on the input signal. Noise introduced by an amplifier will introduce a variation in the peak value of the pulse. This variation results in a broadening of the resolution. A noise signal with a root mean square voltage of σ_n gives rise to a resolution of σ_x

$$\frac{\sigma_x}{\hat{x}} = \sigma_n \frac{\sqrt{Q_A^2 + Q_B^2}}{(Q_A + Q_B)^2} \,, \tag{4.6}$$

and a similar expression for σ_y. The resolution will be worse if Q_A and Q_B are more different. When a Gaussian resolution contribution is assumed, for the FWHM of the resolution $2\sigma_x\sqrt{ln4} = 2.35\sigma_x$ is found. When the input signal is larger, the signal to noise ratio is larger and hence the contribution to the spatial resolution decreases.

Digitization of Q_A, Q_B, Q_C and Q_D during the ADC conversion

The peak values of the signals A, B, C and D are measured using a peak detector and an Analog to Digital Converter. Digitization of the signal gives rise to a fluctuation of the measured value of the peak of maximally one bit of the ADC. Furthermore, the way eq. (4.5) is evaluated also gives rise to a variation in the determination of the position. When the position is calculated using eq. (4.4) this resolution can be simulated. In the simulation Q_A had a homogenous pulse-height distribution between 0 and Q_{max}. Q_B was calculated with eq. (4.4) ($x = \hat{x}/2$). Q_A and Q_B were digitized using 8 bits (0 - $2^8 = 0$ - Q_{max}). Then x was calculated again by using eq. (4.4) and reduced to 8 bits. The result is shown by the full line in fig. 4.12.

The effect of digitizing Q_A and Q_B is clear. Simulations show that this effect will be less if more bits to digitize Q_A and Q_B are used. Another improvement is

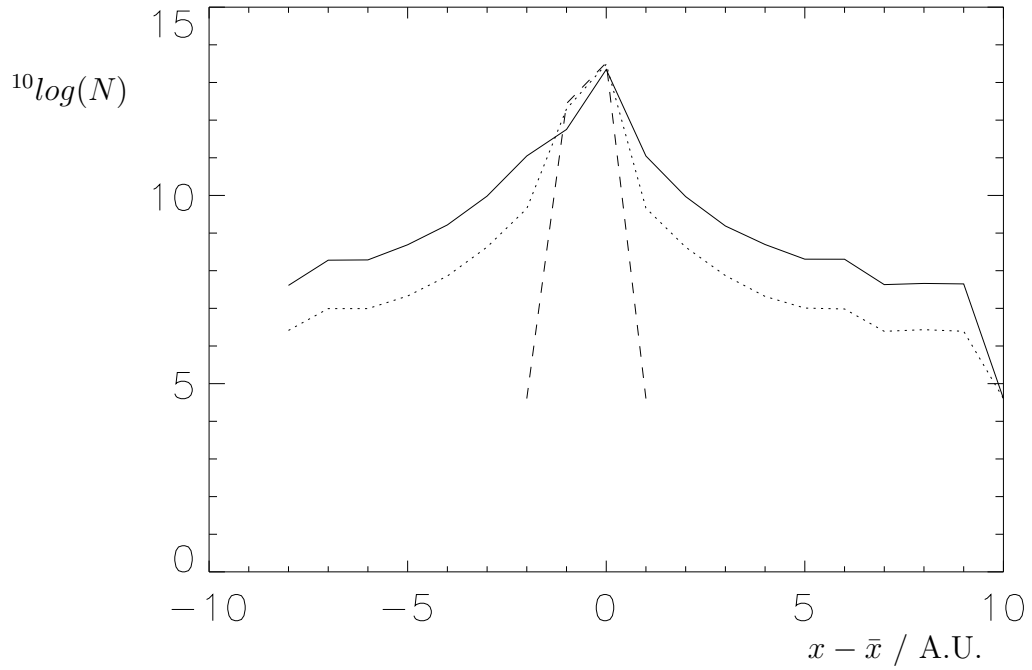

Figure 4.12: *Effect of digitization on the resolution of the PSD. A (full line): 8 bits used for digitization; B (dotted line), C (dashed line): 10 bits used for digitization; A,B: Q_A and Q_B varied between 0 and Q_{max}; C: Q_A and Q_B varied between $0.9Q_{max}$ and Q_{max} (see also text).*

to apply a lower limit to Q_A and Q_B. This can be understood reviewing eq. (4.6). Now, σ_n is produced by the truncation process due to the digitation, so σ_n is of the order of one bit. For small values of Q_A and Q_B σ_x will become very large. In the final hardware 10 bits are used to digitize Q_A and Q_B. The simulation is represented by the dotted line in fig. 4.12. Also there will be a lower level for Q_A and Q_B, so the problems mentioned above are significantly reduced, as shown by the dashed line in fig. 4.12.

4.5.2 Scintillator and photo-multiplier resolution contributions

Fluctuation of the absorption position of the neutron

The absorption position of the neutron in the scintillator varies because of the width of the impinging neutron beam. Furthermore, the depth to which the neutron penetrates the scintillator, is determined by whether or not the neutron is absorbed by a ^{6}Li nucleus. However, because during the test measurements the width of the impinging neutron beam was small (ø FWHM 0.5 mm) and the thickness of the scintillator is not very large (1 to 1.5 mm) the contribution of this effect to the resolution is negligible compared to the contributions of the effects discussed in the following sections.

Fluctuation of the number of photons produced by a neutron absorption

When a neutron is absorbed an energy of 4.6 MeV is released in the form of kinetic energy of the fission products ^{3}H and ^{4}He. Only a small fraction of this energy is converted into light radiation. This fraction is determined by the type of scintillator used, but also differs from interaction to interaction.

Fluctuation in the number and position of the photons which reached the photo-cathode

In the ideal case the photons created by the absorption of the neutron will spread isotropically in all directions. However, because of crystal imperfections or impurities this can vary. The position of absorption in the scintillator results in a varying number of photons hitting the photo-cathode. The solid angle of the photons created that will reach the cathode is determined by total internal reflection in the combination of the scintillator and photo-multiplier window. A refractive index of 1.5 yields a critical angle of total reflection of $\approx 50^o$. This means that only photons within a solid angle of $\pi/2$ sterad are transmitted to the cathode, yielding for the LiI scintillator a fraction of photons which reach the cathode, $\epsilon_{g,1}$, of 0.12. The Li-glass scintillator was used in combination with a diffuse reflector, resulting in $\epsilon_{g,2} \approx 2\epsilon_{g,1}$.

Fluctuation in the number and position of the photo-electrons on the anode of the photo-multiplier

Photo-electrons created by photons hitting the photo-cathode will be accelerated towards the anode. This avalanche process increases the spread in position of the electrons. The resolution contribution of the geometry of the scintillator and the photo-multiplier is given by [37]

$$\sigma_p = \frac{\sigma_g}{\sqrt{\epsilon_q \epsilon_g N_p}} \ , \tag{4.7}$$

where σ_g is the variance of the averaged photo-electron distribution hitting the anode and depends on the geometry of the scintillator and the photo-multiplier only, ϵ_q is the quantum efficiency of the photo-cathode of approximately 0.2, and N_p is the number of created photons. Note that if more photons are created the resolution will be better.

All effects mentioned in the above sections add up to a (gaussian) resolution. To differentiate between the PSD-resolution contribution and the electronic-resolution contribution the scintillator is changed. Also the resolution contribution of part of the electronics can be determined by making Q_A, Q_B, Q_C and Q_D equal. This gives information about the resolution contribution of the final amplifiers and the digitization process.

4.5.3 Resolution measurements

In these measurements x was determined using eq. (4.4), because f_x and f_y were not yet determined.

Determination of the electronic-resolution contribution

To determine the electronic resolution contribution, σ_e of the final amplifiers and the ADC, Q_A and Q_B were made equal and close to Q_{max}, the peak value of the pulse-height distribution of the neutrons. The result is shown as the full line in fig. 4.13. The FWHM equals 2.2(2) channels, which corresponds to 0.93(5) mm (241 channels = 100 mm), so $\sigma_e = 0.40(2)$ mm.

Determination of the PSD-resolution contribution

To determine the resolution contribution of the PSD and to check whether eq. (4.7) holds, the total resolution σ_x of electronics and PSD was measured:

$$\sigma_x^2 = \sigma_e^2 + \sigma_p^2 \ , \tag{4.8}$$

where σ_p is the resolution contribution of the PSD with LiI scintillator, $\sigma_{p,1}$, or the resolution contribution with the Li-glass, $\sigma_{p,2}$. The results are shown as the dashed and dotted lines in fig. 4.13. From the full widths at half maximum the

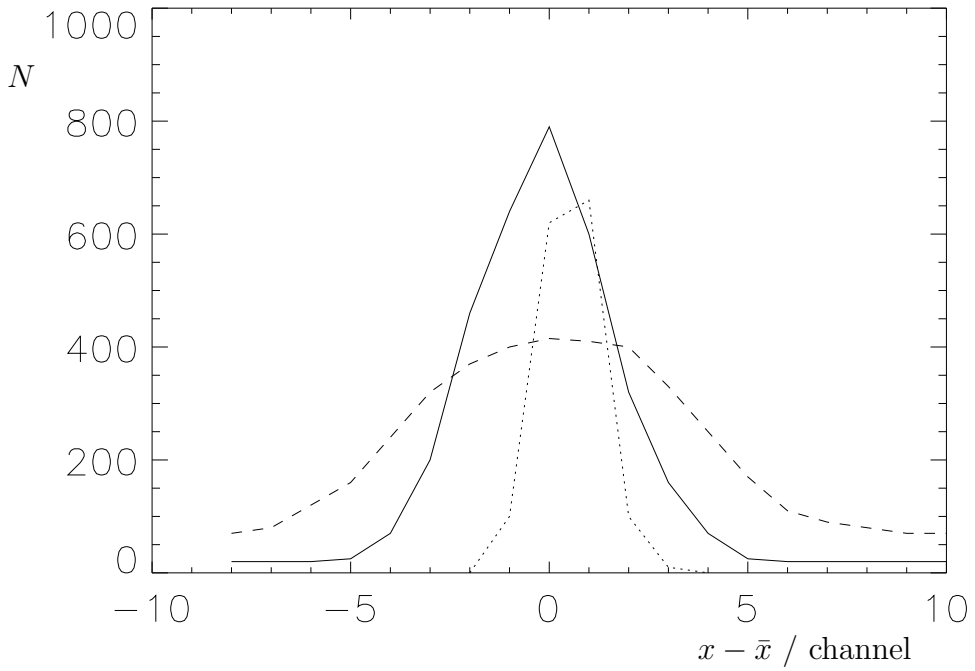

Figure 4.13: *Measured resolution distributions for only the final amplifier and the A/D converter (dotted line), both electronics and PSD with LiI(Eu) scintillator (full line), and both electronics and PSD with Li glass (dashed line).*

$\sigma_{p,1}$ and $\sigma_{p,2}$ were calculated: $\sigma_{p,1} = 0.54(6)$ mm and $\sigma_{p,2} = 1.51(5)$ mm. Using eq. (4.7) and 24000 photons for LiI crystal and 2000 photons for Li-glass yields $\sigma_{g,1} = 13$ mm and $\sigma_{g,2} = 15$ mm, respectively. From this it is concluded that $\sigma_{g,1}$ and $\sigma_{g,2}$ are mainly determined by the size of the electron spot at the anode [37].

4.6 Lower, middle and upper discrimination levels

To reduce the background countrate of PSD it is essential that the electronic hardware of the PSD can discriminate between electric pulses created by gamma radiation and pulses created by neutron radiation. Usually neutrons will create larger pulses than gamma radiation. When all pulses are interpreted as neutrons, this will lead to an increased background countrate. Lower (LL) and Upper (UL) Levels will be used, so only pulses in the vicinity of the neutron-peak pulse-height will be taken into account. A Middle Level (ML) is needed to fix the pulse-height distribution to a certain constant distribution by means of gain stabilization [38]. Due to temperature fluctuations the neutron-peak pulse-height varies. Measurements show that this shift is approximately 0.5 % per ^{o}C. The neutron-peak pulse-height varies considerably over the total area of PSD. This is why it was decided to use a position-dependent LL, ML and UL, to obtain the optimum

background suppression.

First POSX and POSY tables as described in section 4.4 must be made. Then the pulse-height distribution, $p(h)$ for each (x, y) combination is determined, with $h = Q_A + Q_B + Q_C + Q_D$. The peak in the pulse-height distribution is approximated by a gaussian distribution, with $\bar{h}$ the mean value of the peak and σ_h its standard deviation. When $p(h)$ is measured, $\bar{h}$ and σ_h can be determined. Then for LL $= \bar{h} - a\sigma_h$, ML $= \bar{h}$ and UL $= \bar{h} + a\sigma_h$ is chosen. a is chosen to minimize the relative variance of the signal. It can be shown that if the signal to background countrate is of the order of 1 the minimum relative variance is found for $a \approx 1.5$. To determine the position-dependent quantities $\bar{h}(x, y)$ and $\sigma_h(x, y)$, three tables must be created: $N(x, y)$ to store the number of neutrons detected at position (x, y), $SUMH(x, y)$ to store Σh at position (x, y) and $SUMHH(x, y)$ to store Σh^2. From these tables $\bar{h}(x, y)$ and $\sigma_h(x, y)$ can be calculated

$$\bar{h}(x,y) = \frac{SUMH(x,y)}{N(x,y)} \quad \text{and} \quad \sigma_h(x,y) = \sqrt{\frac{SUMHH(x,y)}{N(x,y)} - \bar{h}^2}\ . \tag{4.9}$$

Note that the position (x, y) can be determined using POSX and POSY tables, so it is not necessary to use a collimated beam. However, for an accurate determination of the pulse-height distribution at position (x, y), a high neutron countrate at that position is favourable. Fig. 4.14 shows the ML table. Clearly the (x, y) dependence can be observed.

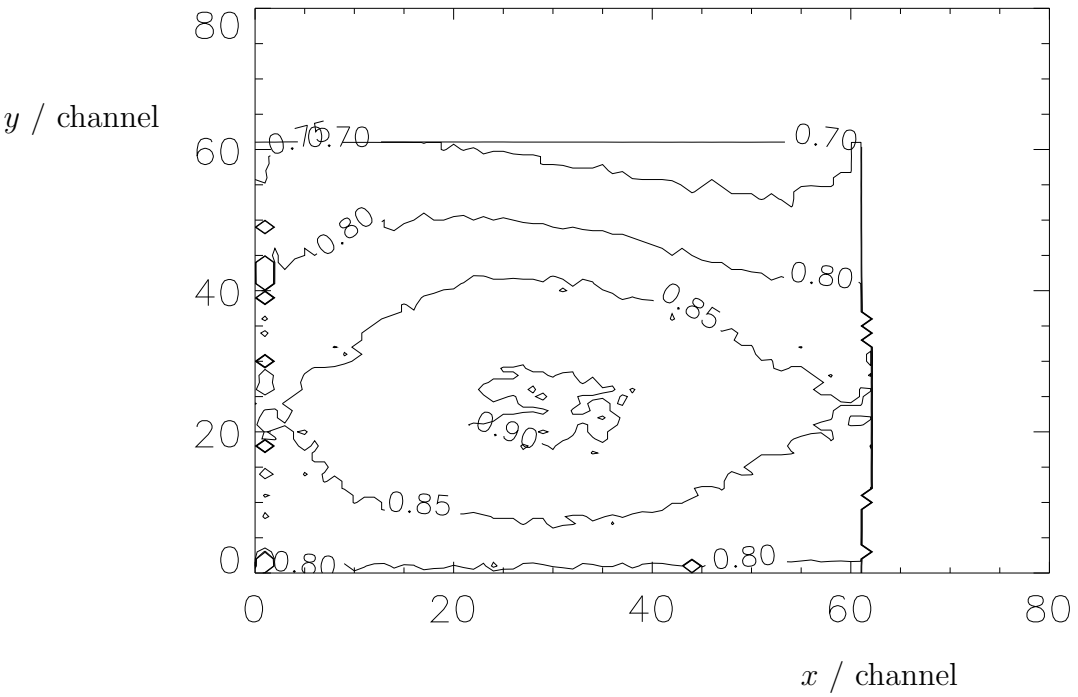

Figure 4.14: *Graph of the peak of the pulseheight distribution in arbritrary units as a function of the position on the PSD.*

Measurements performed with Li-glass as scintillator show a reduction in background countrate of a factor of 2 to 10, depending on the type of radiation field the PSD is subjected to.

4.7 Conclusions

The spatial resolution of the PSD is determined by the electronics, the scintillator used, and the intrinsic photo-multiplier contribution. Two scintillators were tested, LiI(Eu) crystal and Li glass (type GS20). A gaussian resolution distribution was assumed with a standard deviation σ_x. The resolution contribution of the electronics was measured separately and is 0.40(2) mm. The resolution contribution of the LiI(Eu) crystal was determined by measuring the total resolution and subtracting the electronic resolution contribution; it equals 0.54(6) mm and is of the same order as the electronic resolution contribution. The resolution contribution of the Li glass was determined in the same way and is 1.51(5) mm, which is much larger than the electronic resolution contribution. This is in agreement with eq. (4.7). A reduction of the electronic-resolution contribution will improve the resolution. This can be done by reducing the noise of the amplifiers or by using more bits for digitization. However, the lower limit of the total resolution will be $\sigma_x = 0.54(6)$ mm. Using lower and upper level discrimination tables reduces the background countrate considerably. From the above it is concluded that the performance of the PSD described here, is satisfactory.

Chapter 5

Data handling[†]

However much man may toil in seeking,
he will not find it out;

even though a wise man claims to know,
he cannot find it out.

Ecclesiastes 8:17

5.1 Introduction

With ROG, neutron intensities are measured before the sample by a monitor (MON) and after the sample by a single detector (DET). There is a position sensitive detector (PSD) available to measure the position of the reflected neutron in two directions (x, y). The x-direction is perpendicular to sample plane and incident beam. The y-direction is parallel to sample plane and perpendicular to incident beam.

ROG has the possibility to measure wavelength-dependent neutron intensities by measuring the time of flight t_{TOF}. A multi-channel time-of-flight (TOF) analyzer counts the number of neutrons arriving at the detector within time intervals corresponding to the channel widths. The channel widths are user adjustable, so they can be matched to other resolution contributions (see section 3.7). For measurements with monitor or single detector 256 channels of 4 bytes are available, therefore the maximum number of counts per channel is 4.29×10^9, restricted by memory. For measurements with the PSD 256×256 channels of 2 bytes are available; here the maximum number of counts per channel is 65535.

[†]Parts of this chapter are published as: 'ROG, the neutron reflectometer at IRI, Delft', V.O. de Haan, J. de Blois, P. van der Ende, H. Fredrikze, A. van der Graaf, M.N. Schipper, A.A. van Well and J. van der Zanden, Nucl. Instrum. Methods in Phys. Res. A (accepted) and 'Genetic algorithms used in model finding and fitting for neutron reflection experiments', V.O. de Haan and G.G. Drijkoningen, Physica B **198** (1994) 24.

If a sample has a periodically changing scattering-length density in time, T, the corresponding reflection profiles can also be measured. Then, the y dependence of the measurement is interchanged for time channels representing T. Because of the low neutron intensity, this can only be used when the sample changes periodically. This option will not be considered in this thesis. The neutrons are labeled in the hardware with the parameters mentioned above. The 'labelled neutrons' are sorted in the dual-ported memory (DPM) by adding 1 to the contents of a corresponding memory address. The maximum memory needed for a TOF measurement with the PSD and two spin states is 64 Mbytes.

The data is collected on the VME electronics of ROG and transferred to a VAX workstation (VS6) [39]. This is shown in fig. 5.1. The neutron pulses are detected by the data handling module (DHM) [40]. A FIFO-buffer at the input averages the incoming neutron countrate. Here the neutrons are labelled. Neutron pulses are processed by the multi-channel TOF analyzer connected to a data handling module and stored in a 64 MBytes DPM. A VSB connection to the DHM is one part of the DPM and the VME bus the second. In this way the storage rate of the input data is independent of the computer control. VS6 is connected to the VME system, using the SCSI bus. Therefore the DPM can be read as a virtual harddisk of VS6. Data transport from DPM to the hard disk of VS6 is done automatically after a measurement has been finished. Even during a measurement data transport can take place for continuous investigation of the measured data. The data is stored automatically on a mass storage device. VS6 is used for data reduction and correction.

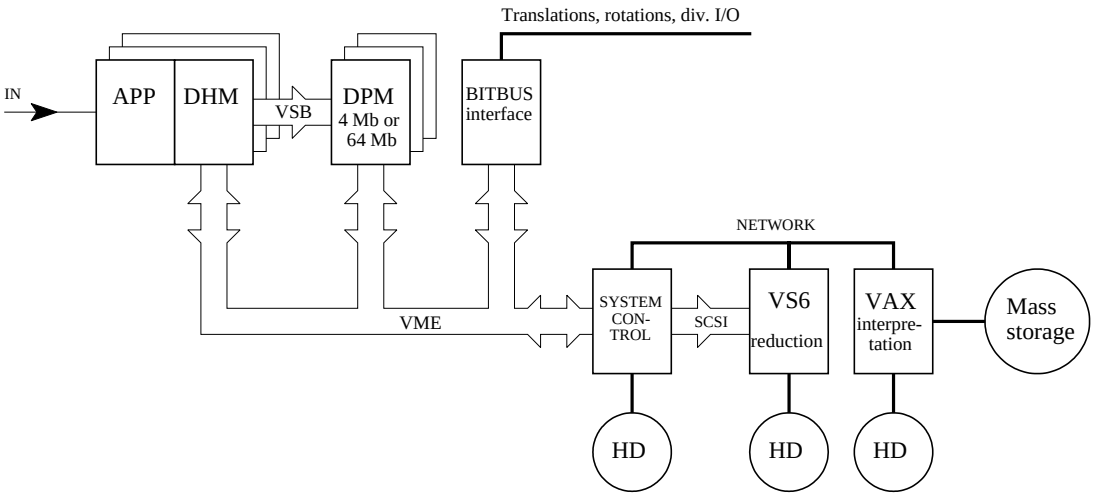

Figure 5.1: *Schematic view of the data flow.*

For specular reflection measurements the component of the wavevector perpendicular to the sample plane, q is the important parameter. With PSD q depends on x and t_{TOF}. With DET q depends on the (fixed) position of the detector and t_{TOF}. The corrections needed to obtain the reflectivity $R(q)$ from raw data are described in section 5.2.

A VAX mainframe is used for data fitting and interpretation. The fit procedures are discussed in sections 5.3 and 5.4. The last section of this chapter describes how the correlation between the model parameters can be estimated.

5.2 Corrections and calibrations

Before data can be interpreted, the parameters of the measured intensities, such as wavelength, λ and angle of reflection, θ_0 must be determined. Also, some data correction calculations, such as constant background and dead time, must be performed. The variance in the measured intensity is calculated assuming Poisson statistics. By using the law of propagation of errors the variance of the reflectivity is determined. The next sections describe these correction calculations.

5.2.1 Wavelength determination

The neutron wavelength is determined by measuring the total time of flight of a neutron from the chopper to the detector. The number of neutrons counted in time-of-flight channel i, with a finite time interval from t_i to t_{i+1}, is denoted by C_i (see fig. 5.2). The value of i varies between 1 and the total number of channels, N. The settings t_i are user adjustable. Usually $(t_{i+1} - t_i)/t_i$ is chosen to be constant (see also section 3.2).

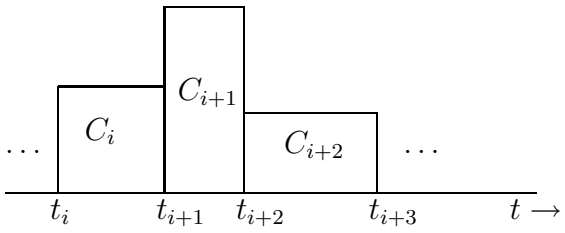

Figure 5.2: *Graphical representation of the multi-channel time-of-flight analyzer.*

The neutron wavelength corresponding to the time of flight is given by

$$\lambda_i = \frac{h}{m_n} \frac{t_i}{L_{TOF}} \ , \tag{5.1}$$

L_{TOF} is calculated from geometrical parameters, according to appendix A. For the monitor the distance between the mid plane of the chopperblades and the center of the monitor is used. For the detector the distance between the mid plane of the chopperblades and the upstream wall of the detector is used. The average wavelength of the neutrons counted in channel i depends on the shape of the spectrum. If the relative change of the spectrum as a function of wavelength is not too large the average wavelength is given by

$$\bar{\lambda}_i = \frac{\lambda_i + \lambda_{i+1}}{2} \ . \tag{5.2}$$

With measurements of the transmission of 45 mm poly-crystalline beryllium, the wavelength calibration was checked. These measurements are shown in fig. 5.3. The measurements give a cut-off wavelength of 0.396(1) nm. Poly-crystalline beryllium has a cut-off wavelength at 0.3958 nm [41]. Note that within statistical accuracy there is no significant difference. From the measurements it is concluded that the wavelength determination is correct and accurate to 0.25 %, for both monitor and detector.

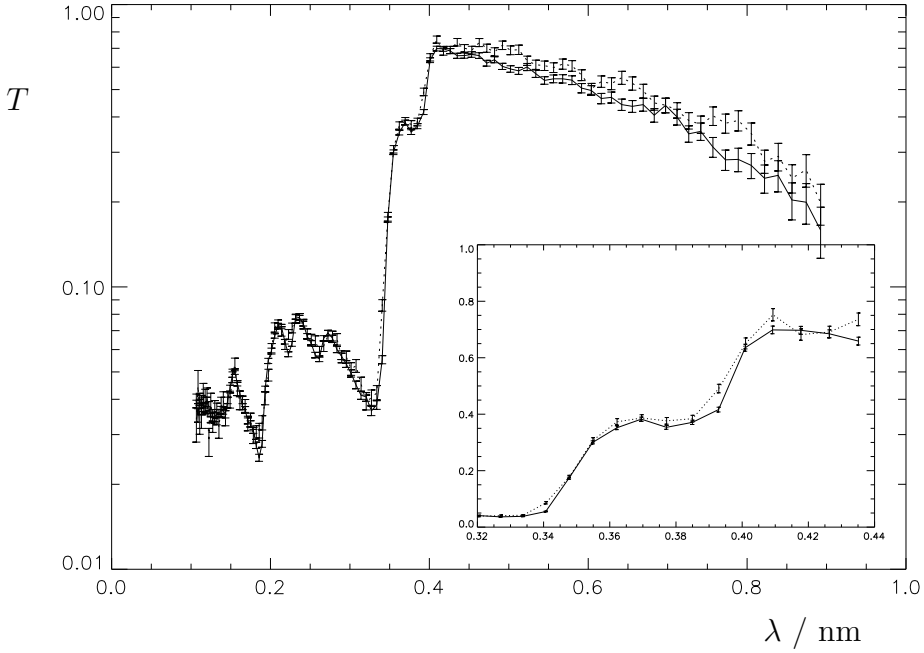

Figure 5.3: *Transmission of 45 mm poly-crystalline beryllium as a function of wavelength as measured with monitor (full line) and detector (dashed line).*

5.2.2 Reflection angle determination

The reflection angle is determined by measuring the position of the straight beam at the position of the diaphragm in front of the detector x_o and the position of the reflected beam x (see section 3.8). With the position-sensitive detector these are measured simultaneously. With the single detector a scan has to be made with a small diaphragm opening in front of the detector. The reflection angle is given by

$$\theta = \frac{x - x_o}{2L_{\mathrm{SD}}} \ , \tag{5.3}$$

where L_{SD} is the distance between sample and the diaphragm in front of the detector. The spread in the reflected angle is mainly determined by the beam definition (see section 3.5) and the sample flatness. The spread in incident angle gives rise to an asymmetric angular distribution of the reflected beam and consequently to a small decrease in x, because the reflectivity depends strongly on

the incident angle. Simulations show a maximum deviation of 0.5 %. Small-angle scattering from windows or air in the flightpath can influence this, but its effect is relatively small. The accuracy of the angle determination strongly depends on the accuracy of x. The accuracy in x depends on the length and flatness of the sample and is typically between 0.02 and 0.10 mm. This introduces an inaccuracy in the angle of $\lesssim 10^{-4}$ radians. In a reflection experiment the height of the diaphragm in front of the detector should be set such that all specularly reflected neutrons from the sample are transmitted.

5.2.3 Constant background

The background countrate of a detector is induced by electronic noise and by unwanted events such as capture of thermal or fast neutrons, or gamma radiation. These unwanted events are converted to counts, yielding a TOF-independent background. The corrected number of counts is given by

$$C_{i,cor} = C_i - c_B(t_{i+1} - t_i)N_f \ , \tag{5.4}$$

where c_B is the background countrate and N_f the number of time-of-flight frames measured. c_B can be determined from a background countrate measurement, which consists of a regular measurement with closed diaphragms. Another way to determine c_B is to use the TOF channels corresponding with wavelengths outside the available wavelength range of the incident spectrum. All events counted in these channels are due to the background countrate. TOF-dependent background due to capture gammas produced by absorption of thermal neutrons can be neglected, because of the low energy of the produced gammas. TOF-dependent background due to incoherent scattering from the sample should also be taken into account, but can usually be neglected. TOF-dependent background caused by short-wavelength neutrons transmitted through the chopper blades becomes important for low countrates in the order of the time-independent background countrate and at the limits of the available wavelength range. It also depends on the reflectivity of the sample and on the frequency of the chopper. Usually these effects can also be neglected.

5.2.4 Dead time

Normally, the dead time of a detector in combination with an amplifier, τ_d is given in seconds. If the measured countrate in a channel, c_i is known, the corrected countrate, $c_{i,cor}$ can be calculated

$$c_{i,cor} = \frac{c_i}{1 - \tau_d c_i} \ . \tag{5.5}$$

This equation holds as long as $\tau_d c_i \ll 1$. For the corrected total number of counts is found

$$C_{i,cor} = C_i \left(1 - \frac{C_i \tau_d}{(t_{i+1} - t_i)N_f}\right)^{-1} \ . \tag{5.6}$$

For ROG the dead time is mainly determined by the amplifiers used. The dead time of the detector and monitor is 14 μs and 12 μs respectively.

5.2.5 Efficiency

The efficiency, ϵ of the detector or monitor depends on the wavelength. It can be calculated assuming the height of the neutron beam is small compared to the effective thickness of the detector, d_e. Then the detector (or monitor) thickness is the same for all neutrons. If the absorption and scattering of neutrons in the wall of the detector or monitor are taken into account, the efficiency is given by

$$\epsilon = a\mathrm{e}^{-b\lambda}(1 - \mathrm{e}^{-c\lambda}) \ , \tag{5.7}$$

where a is determined by the scattering in the wall of the detector or monitor, b by the absorption in the wall and c by the absorption in the detection gas or scintillator for neutrons with a wavelength $\lambda_o = 1$ nm. Here it is assumed that the scattering cross-section is wavelength-independent and that none of the neutrons scattered in the walls are detected, which is reasonable because of the small fraction of scattered neutrons ($\approx 3\%$). In reality the scattering of the wall consists of a large fraction of coherent Bragg scattering. This scattering is wavelength dependent. However, because the fraction of scattered neutrons compared to the number of incident neutrons is small, for the calculation of the efficiency this scattering may be assumed to be wavelength independent. In the ideal case the parameters a, b and c can be calculated, if the wall thickness, d_w and composition of the wall and the detection gas of the detector or monitor are known

$$a = \mathrm{e}^{-\Sigma_{s,w}d_w} \ , \qquad b = \frac{\Sigma_{a,w}d_w}{\lambda_o} \ , \qquad c = \frac{\Sigma_{a,g}d_e}{\lambda_o} \ , \tag{5.8}$$

where $\Sigma_{s,w}$ is the total macroscopic scattering cross section of the wall, $\Sigma_{a,w}$ and $\Sigma_{a,g}$ are the macroscopic absorption cross section of the wall and detection gas (or scintillator) for neutrons with wavelength λ_o[1]. For the detectors and monitor used in ROG, these parameters are listed in tables 5.1 and 5.2. To check these

Detector type	$\Sigma_{s,w}$ m^{-1}	$\Sigma_{a,w}$ m^{-1}	d_w mm	$\Sigma_{a,g}$ m^{-1}	d_e mm
XERAM 30NH15	102	141	0.5	435	25
PSD LiI(Eu)-crystal	0	111*	1.5	9000	1.5
Monitor LCC 4MNH	9.1	7.7	2.0	13	40

* Absorption in Eu and I of LiI(Eu) crystal. Al container ignored.

Table 5.1: *Macroscopic cross sections (λ = 1 nm) of materials used in, and important dimensions of, detectors and monitor of ROG.*

values the transmission of the monitor and detector was measured as a function of

[1]The absorption is assumed to be proportional to the wavelength.

Detector type	a	b / nm^{-1}	c / nm^{-1}
XERAM 30NH15	0.956(4) [0.950]	[0.071]	10.16(4) [10.9]
PSD LiI(Eu)-crystal	0.853(2) [1.000]	0.252(9) [0.167]	13.2(2) [13.5]
Monitor LCC 4MNH	0.997(1) [0.982]	[0.015]	0.744(5) [0.52]

Table 5.2: *Efficiency parameters of ROG detectors and monitor determined from fit (calculated values are added in brackets).*

wavelength (see also section 5.2.6). The transmission of the monitor or detector, T is given by

$$T = a^2 \mathrm{e}^{-(2b+c)\lambda} \ . \tag{5.9}$$

The parameters a and $2b + c$ can be determined from a fit of this equation to the measured transmission. The results are shown in fig. 5.4 and fig. 5.5. The fitted parameters are given in table 5.2. For the detector the parameters agree very well to the values as calculated using the data given by the suppliers of the detectors, except for the b of the PSD. This can be due to the uncertainty in the scintillator composition or the negligence of the fact that Eu is a resonant absorber. The absolute values of a and c for the monitor agree quite well. The

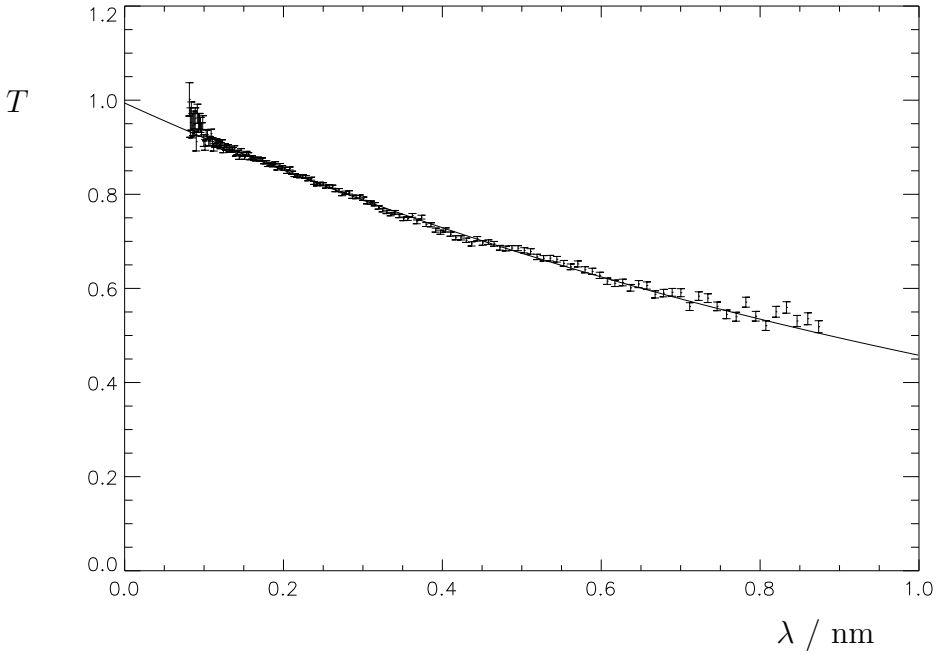

Figure 5.4: *Measured transmission of monitor (error bars) and fit (line).*

efficiencies calculated from these parameters for the monitor and detector are shown in fig. 5.6.

For the PSD the wavelength-dependent efficiency was measured by comparing the incident beam intensity to the number of detected neutrons. The incident beam intensity was measured with the monitor and corrected for the transmission

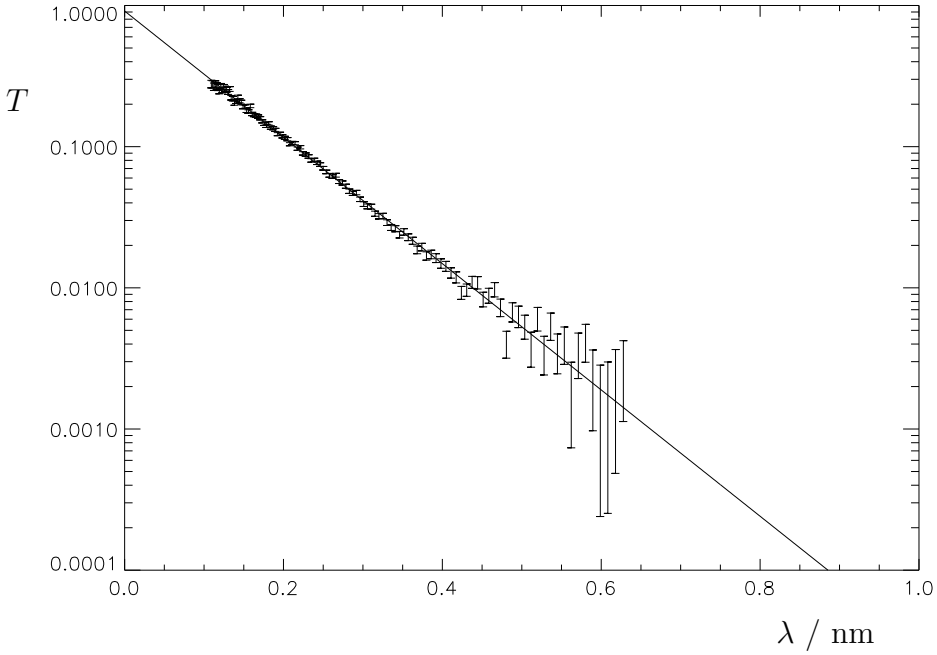

Figure 5.5: *Measured transmission of detector (error bars) and fit (line).*

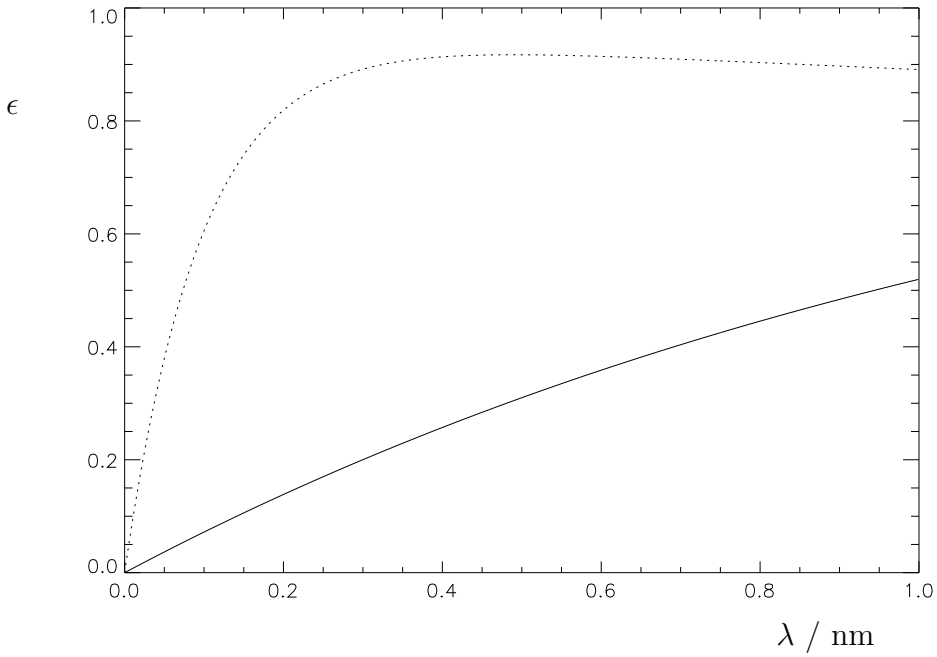

Figure 5.6: *Calculated efficiencies for ROG monitor (full line) and detector (dotted line).*

of the monitor and the attenuation by air between monitor and PSD. The result is shown in fig. 5.7 with error bars. The full line is a fit of eq. (5.7) to the data. The parameters are shown in table 5.2 and agree with the expected values. For

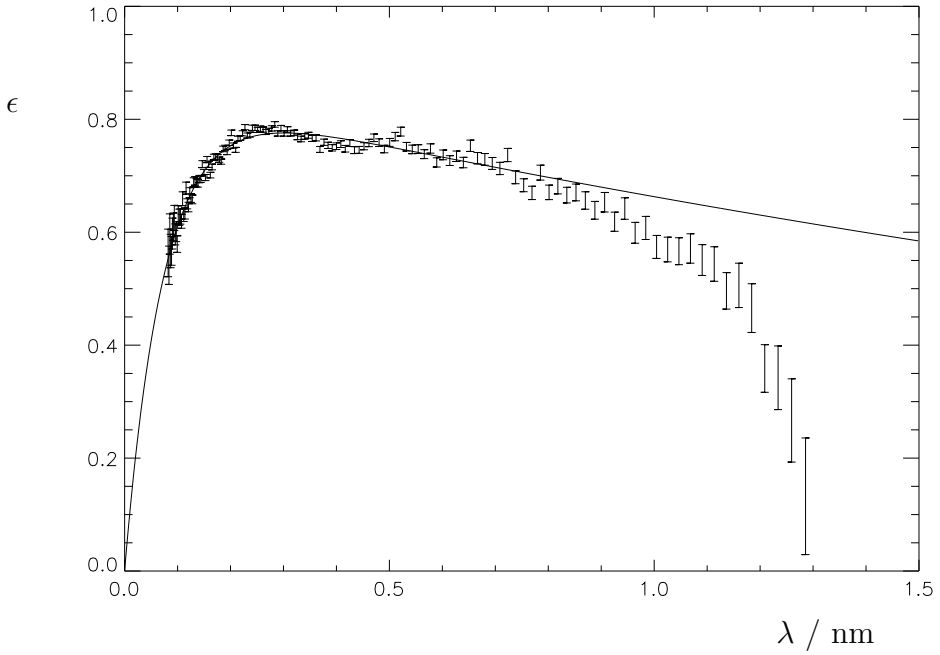

Figure 5.7: *Measured wavelength-dependent efficiency of PSD (error bars) and fit (line).*

the efficiency of monitor and detector is corrected by division of the countrate by the efficiency:

$$c_{i,cor} = \epsilon^{-1} c_i \ . \tag{5.10}$$

5.2.6 Transmission monitor

The neutron beam incident on the sample is attenuated by the monitor. The transmission of the monitor, T_m is given by

$$T_m = a_m^2 \mathrm{e}^{-(2b_m + c_m)\lambda} \ , \tag{5.11}$$

where the index m denotes that the parameters for the monitor should be taken. The transmission of the monitor is shown in fig. 5.4. In the correction procedure the monitor countrate is multiplied by the transmission of the monitor for proper normalization of incident flux on the sample.

5.2.7 Transmission flightpath

The flightpath of the neutrons between monitor and detector is filled with air or argon. By absorption and scattering of neutrons, the intensity of the beam

decreases. The transmission of the flightpath is given by

$$T_{fp} = \mathrm{e}^{-\Sigma_{eff}(\lambda) L_{MonDet}} \ , \tag{5.12}$$

where L_{MonDet} is the distance between monitor and detector, $\Sigma_{eff}(\lambda)$ the effective macroscopic total cross section of the gas in the flightpath. $\Sigma_{eff}(\lambda)$ can be approximated by $\Sigma_{eff} \approx \Sigma_s + \Sigma_a \lambda/\lambda_o$, where Σ_s is an effective macroscopic 'scattering' cross section and Σ_a is an effective macroscopic 'absorption' cross section of the gas for neutrons with a wavelength of $\lambda_o = 1$ nm. For air these parameters were determined by fitting the effective macroscopic total cross section to experimental data. For argon they were determined by fitting the effective macroscopic total cross section to data from literature [42]. The results are shown in table 5.3. The monitor countrate must be multiplied by the transmission of the flightpath.

gas	Σ_s m^{-1}	Σ_a m^{-1}
air	0.030	0.136
argon	0.0007	0.0157

Table 5.3: *Transmission parameters of air and argon at 300 K and 1 atm.*

5.2.8 Reflectivity calculation

The reflectivity is calculated by dividing the corrected number of counts of the detector, $C_{d,i}$ by the corrected number of counts of the monitor, $C_{m,i}$ for a corresponding wavelength region. Normally, the TOF channels of DET and MON are matched. A wavelength region (determined by the channel width) of DET corresponds to a similar wavelength region of MON. Then, the reflectivity is calculated as follows

$$R_i = \frac{C_{d,i}}{C_{m,i}} \ . \tag{5.13}$$

Otherwise, when the wavelength regions do not match, the next equation is used

$$R_k = \frac{\Sigma f_{d,i} C_{d,i}}{\Sigma f_{m,i} C_{m,i}} \ , \tag{5.14}$$

where $\Sigma f_{d,i} C_{d,i}$ is the number of counts detected by the detector in wavelength region λ_k to λ_{k+1} and $\Sigma f_{m,i} C_{m,i}$ the number of counts detected by the monitor in the same wavelength region. $f_{x,i}$ is determined by

$$f_{x,i} = \frac{\lambda_{max} - \lambda_{min}}{\lambda_{x,i+1} - \lambda_{x,i}} \ , \tag{5.15}$$

where x is d or m for detector or monitor respectively, λ_{min} the maximum of λ_k and $\lambda_{x,i}$, and λ_{max} the minimum of λ_{k+1} and $\lambda_{x,i+1}$. To avoid correlation between

two adjacent channels, the wavelength regions λ_k to λ_{k+1} are determined such that at least one TOF channel of either the monitor or the detector is included in the wavelength region. This is elucidated in fig. 5.8. The average wavelength of a region is calculated using eq. 5.2.

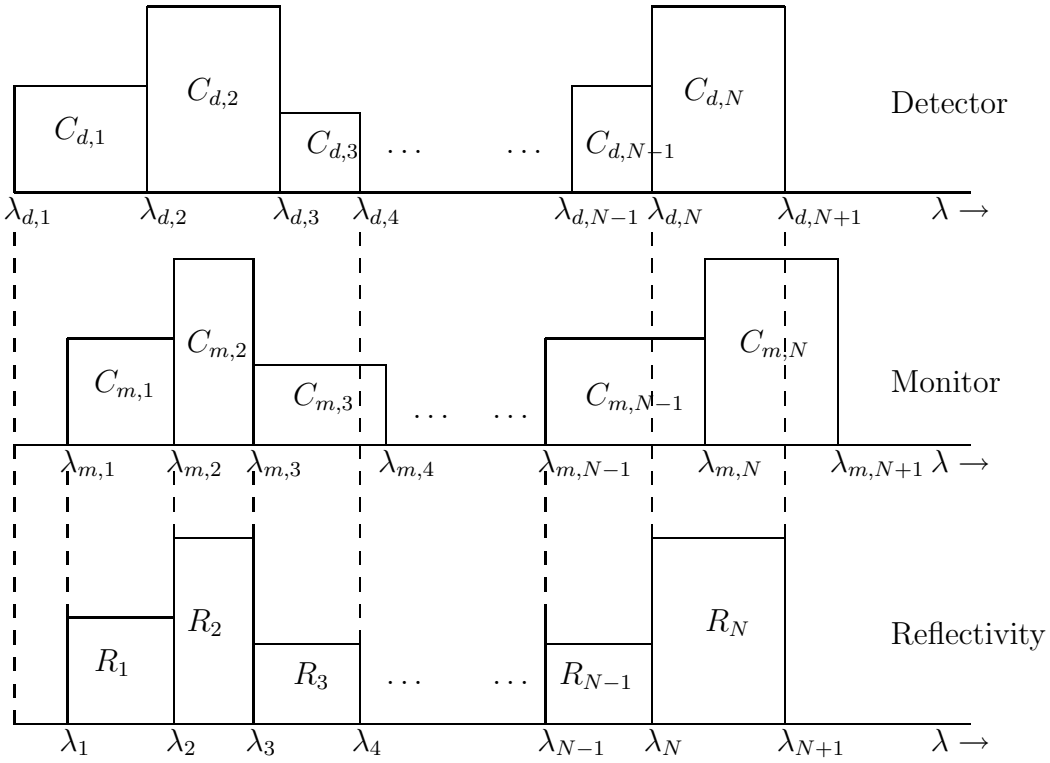

Figure 5.8: *Graphical representation of reflectivity calculation.*

5.2.9 Results

To emphasize the effect of the corrections, in fig. 5.9 the detector and monitor counts of a 3 hour measurement of an empty beam are shown. Note the logarithmic scale and large wavelength range of neutrons available. The heights of the diaphragms were set on 1 mm, the widths on 30 mm. The resolution of the TOF channels, $(t_{i+1} - t_i)/t_i$ was 10 %. At large wavelengths the monitor counted more neutrons than the detector. This is due to the different efficiencies of monitor and detector, and the absorption of neutrons by the monitor. The slope of the curves decreases for large wavelengths. This is due to the background countrate of the detector and monitor. The corrected detector and monitor intensities are shown in fig. 5.10. The ratio of detector over monitor intensity is shown in fig. 5.11. The ratio is 1 within 5 % over the whole wavelength range.

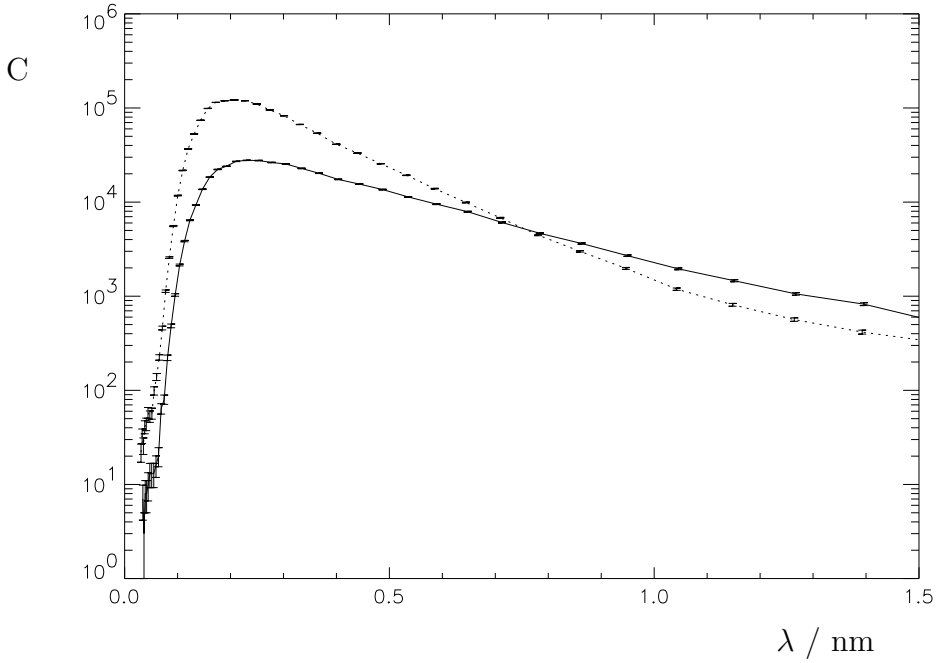

Figure 5.9: *Raw monitor (full line) and detector (dotted line) data as collected by the multi-channel time-of-flight analyzer.*

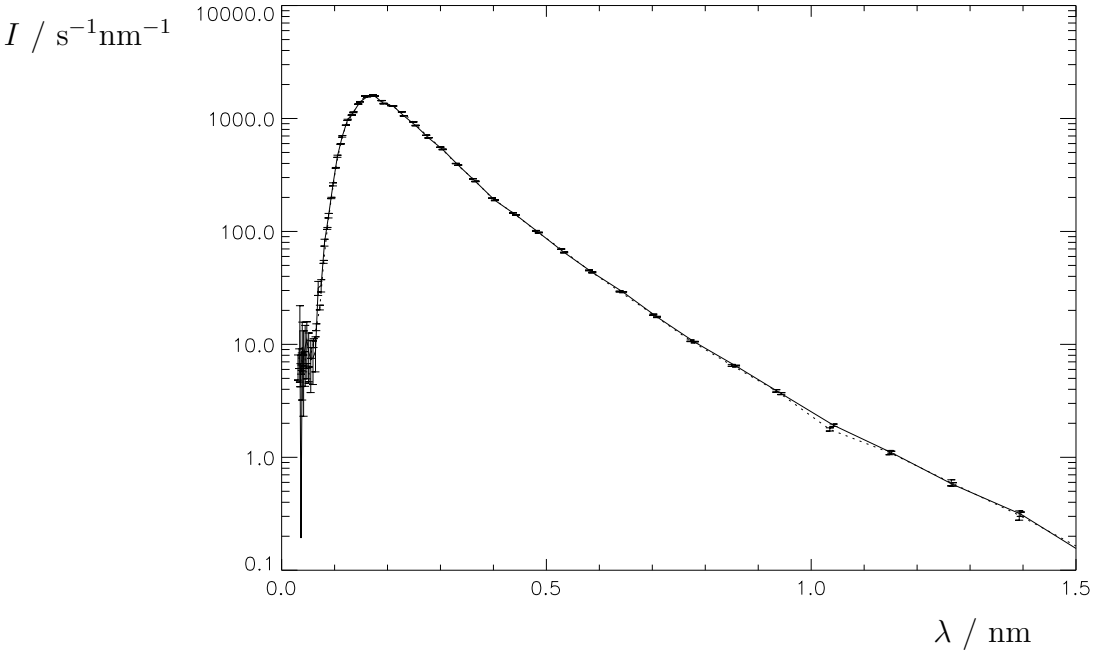

Figure 5.10: *Monitor (full line) and detector (dotted line) intensities, corrected for constant background, efficiency and dead time.*

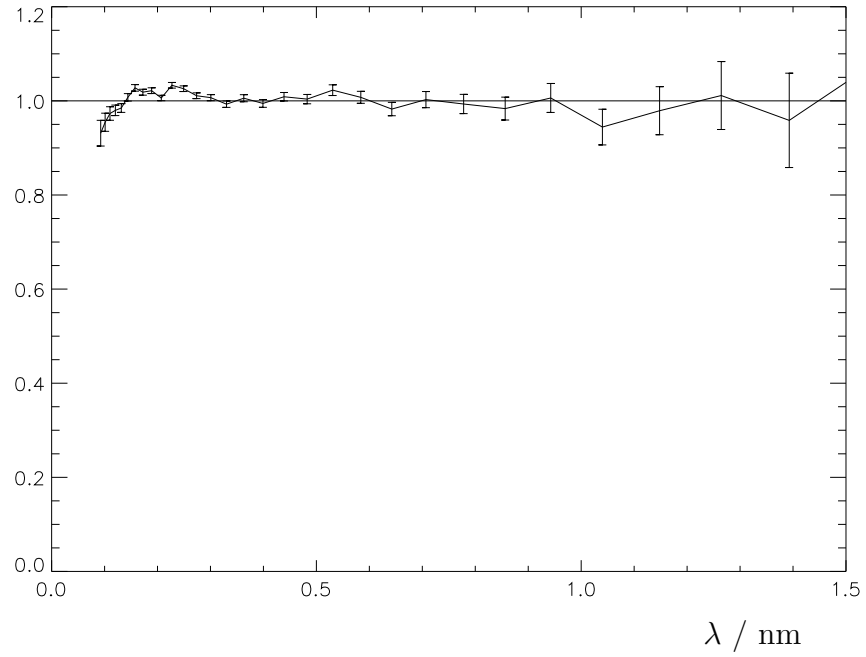

Figure 5.11: *Ratio of corrected detector to monitor intensity.*

5.3 Fit procedure

Although in some special cases[2] it is possible to interpret the reflection profile directly, usually the interpretation is done by model fitting. The depth profile is divided into several layers and for each layer the thickness, the scattering-length density and the interfacial roughness can be fitted. The reflectivity of the model is calculated using the matrix method eq. (2.33) or the recursion relations between the reflectivity at each interface eq. (2.34).

Let χ^2 be the weighted mean-squared deviation of the model reflectivity M_i with the measured reflectivity R_i

$$\chi^2 = (n-p)^{-1} \sum_{i=1}^{n} (\frac{R_i - M_i}{\sigma_{R_i}})^2 \ , \tag{5.16}$$

where n is the number of data points and p the number of fitting parameters of the model. The deviations are weighted with the statistical accuracy, σ_{R_i}. With a weighted least-squares fit procedure it is possible to minimize χ^2. The model fits the data when χ^2 is close to 1. The standard deviation of χ^2 is

$$\sigma_{\chi^2} = \sqrt{\frac{2}{n-p}} \ . \tag{5.17}$$

The uncertainty in the parameters of the model can be estimated by the determination of the confidence interval of a parameter. For a χ^2 distribution with $n-p$

[2]These cases are low reflectivity or profiles which are relatively simple and give standard reflection profiles as discussed in chapter 2.

degrees of freedom the $\alpha \times 100\%$ confidence interval is determined by changing a parameter from its 'best' value until the χ^2 has increased to $\tilde{\chi}^2$, where

$$\frac{\tilde{\chi}^2 - \chi^2}{\chi^2} = \frac{p}{n-p} F(p, n-p, 1-\alpha) \ . \tag{5.18}$$

Here $F(p, n-p, 1-\alpha)$ is the F-distribution for $n-p$ degrees of freedom [44].

Another way to estimate the uncertainties in model parameters is to linearize the problem and use the law of propagation of errors to calculate the variances and covariances in the parameters. This is described in section 5.5. It is possible to find a solution with $\chi^2 \approx 1$ if the initial guess for the parameters is not too far from that minimum, assuming an appropriate model is used. Sometimes different initial conditions can lead to different minima with $\chi^2 \approx 1$. Then, extra knowledge about the sample is needed to decide which minimum is the real minimum. Usually, one needs to know the structure of the sample quite good to find a unique solution. Sometimes the initial guess for the parameters does not lead to a χ^2 of 1. Then different initial conditions, or even different models, have to be tried. In this case only an expert on the field of reflectivity fit procedures can judge which set of initial conditions or what model would have a better chance to converge to a correct minimum. In the next section a method is described, which constructs sets of initial conditions without the explicit help of a fit expert. This method also offers another opportunity to investigate correlations between parameters.

5.4 Genetic algorithms

Genetic algorithms have been studied for over 30 years. They are applied to many fields, ranging from designing jet-turbines to model fitting of seismic data [43]. It is based on the hypothesis of evolution of a species by survival of the fittest individuals within a population. The individuals can create offspring by sexual reproduction. The keyword 'sexual' points to the fact that information that makes an individual fit enough to survive and hence to reproduce is combined with information from an other individual. The resulting offspring can be even more fit. This mixture of information induces a higher rate of evolution of a population than simple reproduction and an occasional mutation. The way this is done in nature is by means of genes and chromosomes. The trick of Genetic algorithms is to create a 'genetic code' that describes the model, and can be manipulated as natural genes. More about the ideas behind Genetic algorithms can be found in [45]-[46].

When a Genetic algorithm is applied to model fitting the genetic code consists of a bit stream. Every parameter of a model is discretized into a number of bits between an upper and lower limit. All these binary parameters are put in a fixed sequence in a one-dimensional array to construct a bit stream. This bit stream contains information about the model. With this genetic code, manipulations of sexual reproduction and mutation can easily be done by manipulating

bits. Sexual reproduction is simulated by taking two bit streams, cutting them at the same random position and swapping two counter parts to create two new bit streams. Mutation is simulated by occasionally changing a bit from 0 to 1 or from 1 to 0. The chance a mutation occurs can be varied and is typical 1 % per bit. The mutation chance should not be taken too large because otherwise random bitstreams are created, loosing the effects of the genetic manipulation. The fitness of a bit stream is calculated by transformation of the discretized parameters to corresponding physical parameters and calculation of the weighted mean square deviation of the measurement from the model. A pool of bit streams is created to simulate a population. Typically a pool contains between 25 and 100 bit streams. For all models in this pool (represented by the bit streams) the fitness is calculated. The next 'generation' is created by mutation, sexual reproduction and survival of the fittest models. One iteration contains a calculation of the fitnesses and the creation of a new pool generation. A typical fit contains approximately 25 to 100 iterations. Further iteration should be stopped, because of breeding-in. The initial pool is generated taking random values for the parameters. A program was developed on a VAX/VMS system with Genetic algorithm subroutines already in use at the department of Mining and Engineering of the Delft University of Technology to apply this algorithm to model finding and fitting of neutron reflection experiments. The results are discussed below.

The Genetic algorithm was applied to a measurement on reflectometer EROS of Laboratoire Leon Brillouin in Saclay [47]. A calibration sample consisting of 5 bilayers of Co/Ti on a glass substrate was measured. The expected scattering-length-density profile as a function of z, the distance perpendicular to the surface, $\Gamma(z)$ is shown in fig. 5.12 (full line) (see also table 5.4 model 'as made'). The measurement is shown as error bars in fig. 5.13. The resolution, scattering-length densities of substrate, Co and Ti and thickness of the Co and Ti layers were fitted. The resolution was discretized using 8 bits, the scattering-length densities using 12 bits, the thicknesses using 8 bits and the roughnesses using 4 bits. The number of bits was determined by looking at the sensitivity in χ^2 of the model if a parameter is increased or decreased by 1 bit. The sensitivity for all these changes should approximately be the same. These parameters are put one after an other in a bitstream. The pool contained 25 bit streams and 50 iterations were performed. Relative to the CPU time needed for the determination of the 25×50 χ^2's, virtually no time was needed for the evaluation of the Genetic algorithm. After 50 iterations the best model in the pool, shown in fig. 5.12 (dotted line), gave $\chi^2 = 3.4$. The calculated reflectivity is shown in fig. 5.13 (full line). For further refinement Genetic algorithms are not suited, particularly because on a small local scale the model can be linearized and a least-square solution will converge faster than Genetic algorithms. The result of the Genetic algorithms procedure was used as an initial model for a least-squares fitting procedure resulting in the model shown in fig. 5.12 (dashed line) with $\chi^2 = 1.4$, which is satisfactory. The reflectivity of this model is shown in fig. 5.13 (dotted line). For the Co layer a thickness of 9.4(4) nm and a scattering-length density of 6.4(3) $.10^{-3}$ nm^{-2}

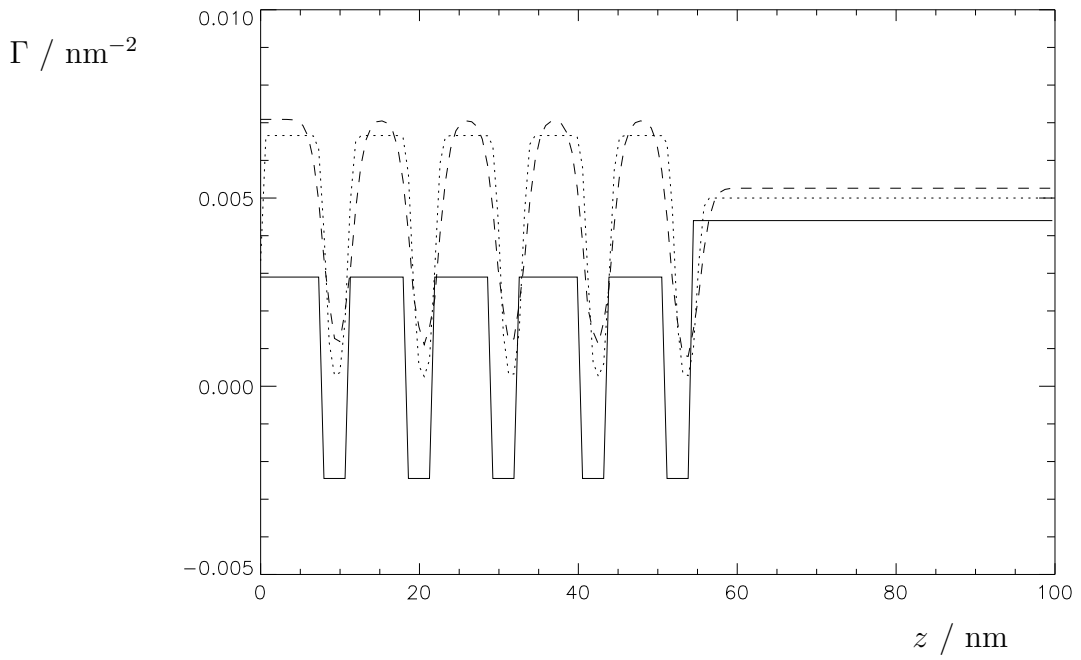

Figure 5.12: *Scattering-length-density profiles of model 'as made' (full line), best model after 50 iterations of Genetic algorithms (dotted line) and model after least-squares fit (dashed line).*

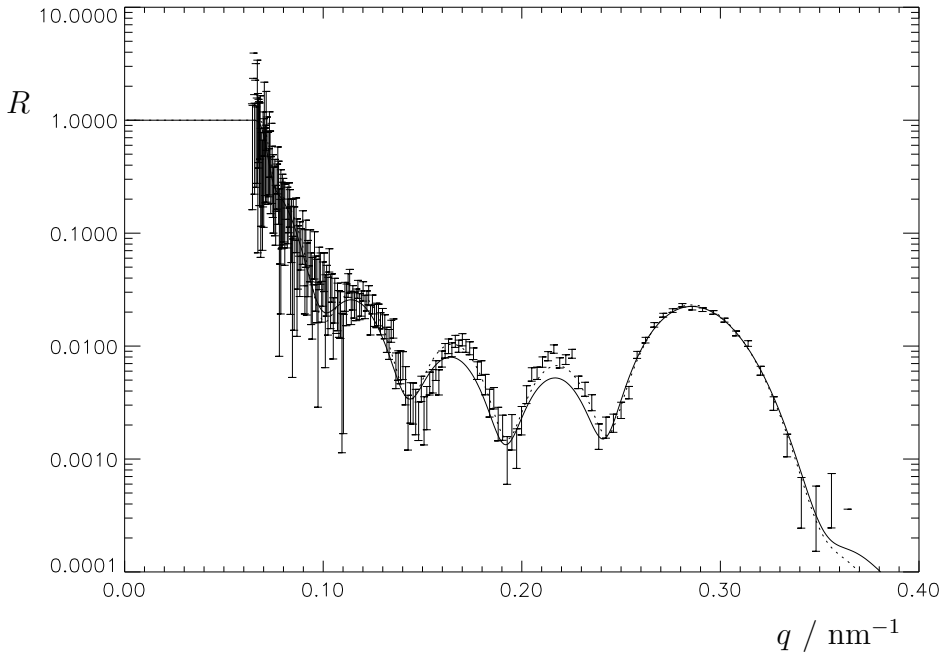

Figure 5.13: *Reflectivity as a function of vertical component of the wave vector of measurement (error bars), best fit after 50 iterations of Genetic algorithms (full line) and least-squares fit with initial model found by Genetic algorithms (dotted line).*

and for the Ti layer a thickness of 1.48(4) nm and a scattering-length density of -5.8(5) $.10^{-3}$ nm^{-2} was found. The interfacial roughness was fitted to be approximately 1 nm at each interface. From the above it is concluded that with Genetic algorithms it is possible to find an initial model for a least-squares fitting procedure independent from the experience of a neutron reflection expert.

5.5 Parameter correlations

An important subject concerning fit procedures, which is commonly left undiscussed, is the correlation between parameters of the model. The question is: how can a set of model parameters change without affecting the fit quality? Two types of correlations can be discriminated. First, 'local correlations' in the vicinity of a local minimum of χ^2 in the parameter space. Second, 'global correlations' within the total parameter space.

'Local correlations' can be studied by linearizing the problem around the minimum and using the law of propagation of errors [48]. The covariance of two model parameters x_i and x_j is given by

$$\mathrm{covar}(x_i, x_j) =< x_i - \bar{x}_i >< x_j - \bar{x}_j >= C_{ij} \ , \tag{5.19}$$

with $\hat{C} = [\hat{J}^{\mathrm{T}}\hat{J}]^{-1}$. $\hat{J}$ is the Jacobian matrix defined by

$$J_{ij} = \partial F_i / \partial x_j \ , \tag{5.20}$$

where $F_i = (R_i - M_i)/\sigma_{R_i}$. The standard deviation of x_i is given by

$$\sigma_{x_i} = \sqrt{\mathrm{covar}(x_i, x_i)} \ . \tag{5.21}$$

The correlation between x_i and x_j is given by

$$r_{x_i,x_j} = \frac{\mathrm{covar}(x_i, x_j)}{\sigma_{x_i}\sigma_{x_j}} \ . \tag{5.22}$$

'Global correlations' can not be studied using solely least-squares because of its local character. Genetic algorithms explore the whole parameter space and in combination with least-squares can be used to study global correlations. The previously discussed measurement is used to illustrate the possibilities of Genetic algorithms to investigate global correlations between parameters. Because the fitted Γ for the Ti layer did not match the theoretical Γ of Ti (-2.45 $.10^{-3}$ nm^{-2}), the 24 other models in the pool were also used as initial model for a least-squares fit. For the Co layer all fits gave approximately the same scattering-length density and thickness. For the Ti layer however, different combinations of scattering-length density and thickness were found, listed in table 5.4, which resulted in fits to the data all with $\chi^2 = 1.4(1)$. From the fact that these combinations are points of a straight line, it was concluded that a fit would also be possible for a fixed

	R	Γ_{glass}	Γ_{Co}	Γ_{Ti}	d_{Co}	d_{Ti}
		10^{-3}	10^{-3}	10^{-3}		
#	%	nm^{-2}	nm^{-2}	nm^{-2}	nm	nm
0	-	4.5	2.84	-2.45	7.5	3.3
1	5.8	5.3	6.3	-3.1	9.2	1.8
2	6.6	5.3	6.4	-4.6	9.3	1.6
3	6.1	5.2	6.4	-5.8	9.4	1.5
4	5.8	5.2	6.3	-6.5	9.5	1.4
5	5.9	5.2	6.1	-7.3	9.7	1.2
6	5.6	5.3	6.3	-10.0	10.0	0.9

Table 5.4: *Combinations of scattering length-densities, Γ and thicknesses, d of the Co/Ti bilayer, resulting in a same quality fit with χ^2 = 1.4(1). # 0 is the model 'as made'. # 1 to 6 refer to models resulting from the Genetic algorithm procedure (see text). R is the resolution (FWHM) of the measurement.*

scattering-length density of the Ti layer of -2.4 $.10^{-3}$ nm^{-2}, with a thickness of approximately 2 nm. Taking these values as initial conditions for a least-squares fit, keeping the scattering-length density of Ti fixed, resulted in a thickness of 2.1(4) nm. The conclusion is that the combination of Genetic algorithm and least-squares fitting procedures can be used as a tool to investigate the parameter dependence of the fit. It can find different sections of the parameter space where local minima are located.

The deviations of this model to the 'as made' model may be due to magnetization of the Co, resulting in a higher scattering-length density for the Co layers (see also table 2.1), and roughness of the layers resulting in a (gaussian) transition zone between two layers. The scattering-length density of the glass was also found to be higher than that of SiO_2 ($4.5\times10^{-3}\text{nm}^{-2}$), which can be due to uncertainties in glass composition.

Chapter 6

Adsorption of diblock copolymers at the air-water interface†

Every perfection is attended with a certain imperfection,
and dark spots remain in all our contemplations.

Thomas a Kempis

6.1 Introduction

In many natural and technical processes the presence of polymers at surfaces and interfaces plays a crucial role (for a recent overview see [49], [50]). Therefore, it is needed that the adsorption process of a polymer at a surface is understood. Scaling theories [51] and self-consistent field (SCF) theories [52], [53] predict the volume fraction profile of the polymer at the interface. The adsorption of diblock copolymers at the air-water interface is studied to compare the SCF theory with both macroscopic surface pressure and microscopic neutron reflectivity measurements. The SCF theory is applied for relatively small volume fractions of polymers.

In the next sections the theory of terminally-attached polymers is discussed and the model and sample preparation are described. Then surface-pressure and neutron-reflectivity measurements for a series of polymers (with a large range in number of segments) as a function of surface concentration are presented. The last section gives the discussion and conclusions.

†This chapter will be published as: 'Adsorption of diblock copolymers at the air-water interface', V.O. de Haan, H.D. Bijsterbosch, M.A. Cohen Stuart, A.W. de Graaf, F.A.M. Leermakers and A.A. van Well (in preparation).

6.2 Theory of terminally-attached polymers

A system of polymers, each consisting of m segments, is considered. One end of the polymer chain is grafted to a surface. The chains are extended into the solution, forming a brush. The height of this brush, H and the volume fraction profile, $\Phi(z)$ are described by the SCF theory. This theory is based on a quasi-crystalline lattice model [52]. Because of a mean-field approach all interactions within a layer parallel to the interface are smeared out. Every site of the lattice can be occupied by either a segment of the polymer or a solvent molecule. The SCF theory as used here, assumes that each site or segment has the same size as a solvent molecule, which is of the same order as the bond length of a monomer, l. By taking into account all possible conformations, each weighted with its Boltzmann probability factor, the equilibrium distribution of a polymer-solvent system at the interface is calculated. Nearest-neighbour interactions between polymer segments and solvent molecules are taken into account by the Flory-Huggins interaction parameter, χ.

If the volume fraction of polymer is not too large (< 0.2) it can be described with a parabolic profile [49], [53]

$$\Phi(z) = \frac{3}{2}\bar{\Phi}(1 - \frac{z^2}{H^2}) \quad , \tag{6.1}$$

where $\bar{\Phi}$ is the average volume fraction of the polymer brush. $\bar{\Phi}$ only depends on the number of polymer molecules at the surface

$$\bar{\Phi} = \eta l^{4/3} A_s^{-2/3} \quad , \tag{6.2}$$

where A_s is the available area per molecule, $\eta = (\pi^2/72p\nu)^{1/3}$, p the stiffness parameter and $\nu = 1 - 2\chi$ the excluded-volume parameter. The brush height also depends linearly on the number of segments of the polymer

$$H = \eta^{-1} m l^{5/3} A_s^{-1/3} \quad . \tag{6.3}$$

For the surface pressure of the brush is found [52]

$$\frac{\pi_b}{kT} \approx \left(m^{-1} + \frac{3}{5}\nu\bar{\Phi}\right)\bar{\Phi} H l^{-3} = A_s^{-1} + \frac{3}{5}\nu\bar{\Phi} m A_s^{-1} \quad , \tag{6.4}$$

where, k is the Boltzmann constant and T the temperature. This equation only holds for small volume fractions as in eq. (6.1).

6.3 Sample preparation and model

An experimental study is performed of polymer adsorption at the air-water interface. Then there is perfect control over the surface density of the polymers and the system is accessible for thermodynamic measurements (surface pressure) and

for neutron reflectivity studies, yielding structural information. The adsorption to the air-water interface is obtained by using amphiphillic diblock copolymers AB. Part A is hydrophobic polystyrene (PS) $[CH_2 - CH(C_6H_5)]_n$, where n is 38. Part B is hydrophillic polyethylene oxide (PEO) $[C_2H_4 - O]_m$, where m is 90, 148, 250, 445 and 700 for the different polymers used, which are denoted by ZGH-1 to ZGH-5 respectively. The polymers were supplied by G. Riess and and synthesised and characterized by Z. Hruska [54]. The polydispersity is defined as

$$\omega = \frac{< M^2 >}{< M >^2} \quad , \tag{6.5}$$

where M is the molar mass of the polymer. The brackets denote an averaging over the number of molecules with mass M. The polydispersity of the polymers and other parameters are shown in table 6.1.

	PS	PEO
Molar mass monomer with respect to hydrogen, M	104	44
Density, ρ [10^3 kgm^{-3}]	1.04	1.10
Scattering-length density, Γ [10^{-3} nm^{-2}]	1.76	0.75
Bond length, l [nm]	0.25	0.33
Polymer	m	ω
ZGH-1	90	1.21
ZGH-2	148	1.15
ZGH-3	250	1.20
ZGH-4	445	1.17
ZGH-5	700	1.25

Table 6.1: *Parameters of polystyrene (PS) and polyethylene oxide (PEO), and of the polymers used: m is the average length of the tail and ω the polydispersity.*

For the neutron reflection experiments the samples were prepared at room temperature in a teflon trough of 255 × 105 mm. The polymers were dissolved in chloroform (0.5 g/l) and spread by injection on the water surface. In this way the available area per molecule, A_s could be controlled. Analysis with ultraviolet spectroscopy of the concentration of polymers in the chloroform solution shows that also some single blocks of PS and PEO were present. The actual concentration of diblocks is somewhat smaller as assumed. This has no influence on the comparison between the measurements but the absolute values of the fit parameters become less accurate. The reduction of the polymer concentration was neglected in the analysis of the data presented here.

A sketch of the polymers at the air-water interface is shown in fig. 6.1. The hydrophobic part of the polymer acts as an anchor[1], it keeps the polymer grafted to the surface. The hydrophyllic part submerges into the solution like a tail. As

[1]Although it has more resemblance to a buoy in the theory presented here, this part is commonly denoted by 'anchor'.

long as the tail is not forced into the solution it floats at the surface like a pancake (fig. 6.1a). A monolayer [55] of PEO is formed [56]. This is favorable due to the excess of adsorption energy of a segment of the tail at the surface compared to the adsorption energy of a solvent molecule [57], [58]. By increasing the coverage

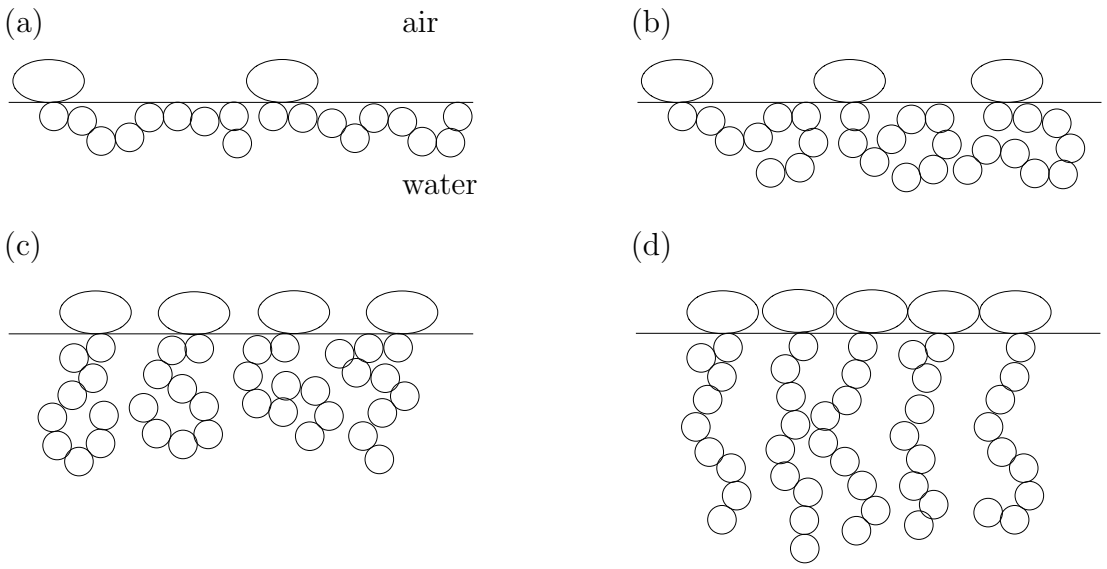

Figure 6.1: *Sketch of a diblock copolymer at the surface of water for decreasing values of the available area per molecule (a) to (d).*

(decreasing A_s) the tails stretch, forming a brush with increasing brush height (swelling).

A similar system is described by Richards et al. [59]. They report on neutron reflectivity measurements of an amphiphillic diblock copolymer at the air-water interface. The anchor of this polymer was polymethylmethacrylate (PMMA) and the buoy PEO.

6.4 Surface-pressure measurements

From measurements of the surface pressure as a function of the available area per molecule it is possible to confirm the model.

Two regions can be distinguished. At low concentration (large A_s) the surface pressure is determined by the PEO monolayer (it is assumed that only PEO contributes to the surface pressure.). For the surface pressure of the adsorbed monolayer is found [52]

$$\frac{\pi_a(A_s)}{kT} = A_s^{-1} - l^{-2}\left(\ln(1-\Phi_o) + \Phi_o + \chi\Phi_o^2\right) \approx A_s^{-1} + \frac{\nu}{2}m^2l^2A_s^{-2} + \frac{1}{3}m^3l^4A_s^{-3} \quad , \tag{6.6}$$

where $\Phi_o = ml^2A_s^{-1}$ is the fraction of surface sites occupied by PEO. The approximation is a virial expansion and only holds for large A_s. For ZGH-5 this

contribution is shown as the dashed line in fig. 6.2 (with $\chi = 0.4$ and $l = 0.33$). If Φ_o goes to 1 (decreasing A_s) eq. (6.6) diverges and the surface pressure increases very fast. Then, PEO is forced into the solution (fig. 6.1b and c). For polymers with smaller tails this occurs for smaller values of A_s. If A_s decreases further a brush is formed and the monolayer does not change significantly so the contribution of the monolayer to the surface pressure remains constant. The maximum of Φ_o depends on the surface-adsorption energy and determines the plateau height. This height does not depend on the length of the tail. To compare with experiment the maximum of Φ_o was taken to be 0.67. At high concentration (small A_s)

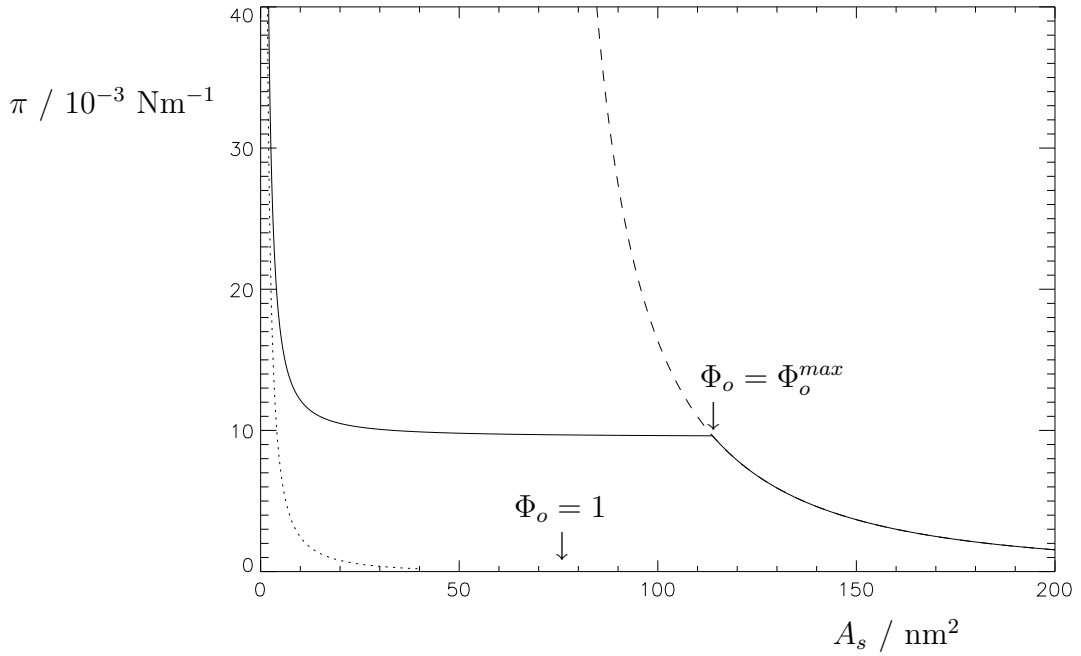

Figure 6.2: *Theoretical surface pressure, π as a function of available area per molecule, A_s for ZGH-5: monolayer PEO (dashed line); contribution of brush (dotted); total (solid).*

a brush is formed. The surface pressure is increased by the repulsion of the tails. The theory to calculate this contribution holds for polymers terminally attached at a solid surface, where the effect of the anchors is ignored and is discussed in section 6.2. For ZGH-5 this contribution conform eq. (6.4) is shown as the dotted line in fig. 6.2 (p was taken to be 0.5 calculated with eq. (A5.5) from [49]). The total surface pressure, π_s is calculated as the sum of the two contributions

$$\pi_s = \pi_a + \pi_b \quad . \tag{6.7}$$

For ZGH-5 the total surface pressure is shown as the solid line in fig. 6.2.

Measurements of the surface pressure, π_s as a function of the available surface area per molecule were performed at the Wageningen Agricultural University. The method used is described elsewhere [60]. The results are shown in fig. 6.3.

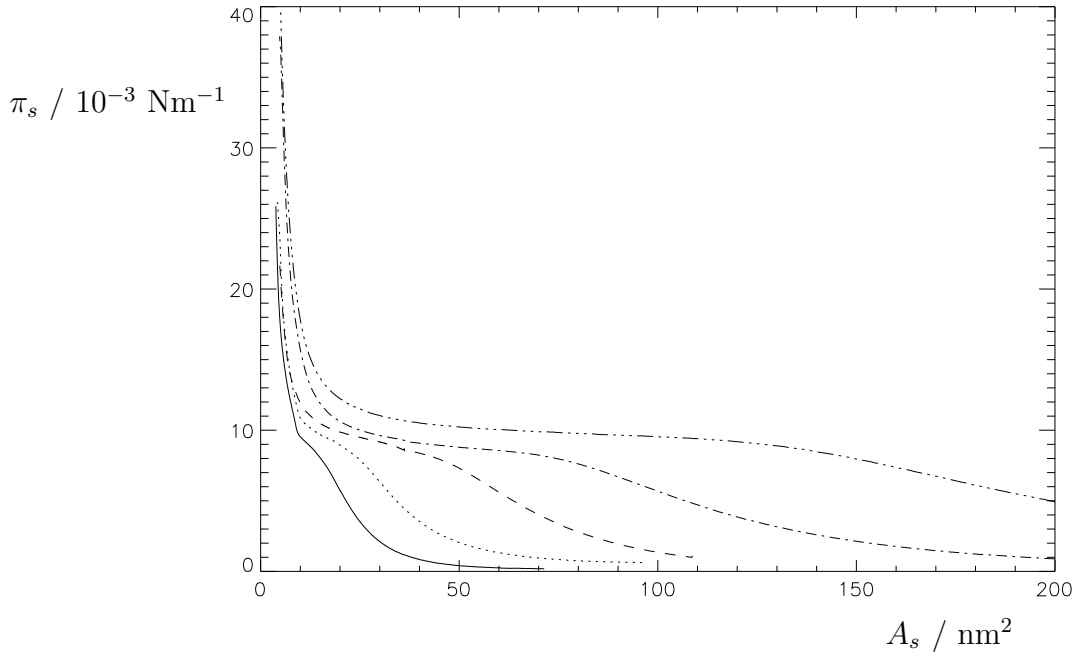

Figure 6.3: *Measured surface pressure, π_s as a function of available area per molecule, A_s for different polymers: ZGH-1 (full line), ZGH-2 (dotted), ZGH-3 (dashed), ZGH-4 (dash-dotted) and ZGH-5 (dot-dot-dot-dashed).*

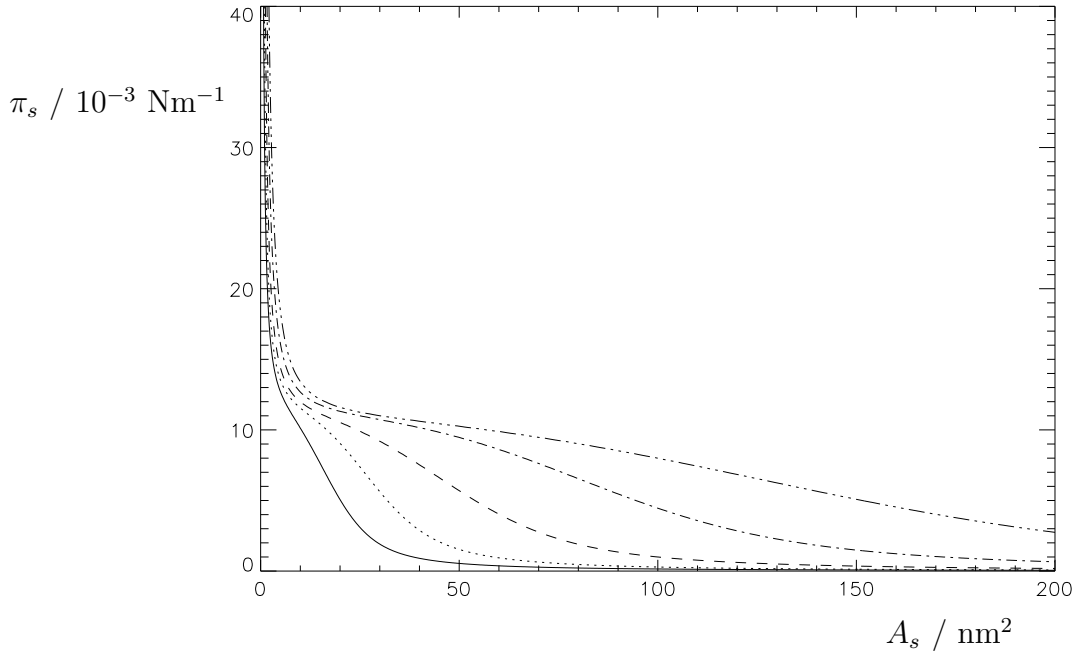

Figure 6.4: *Theoretical surface pressure, π_s as a function of available area per molecule, A_s (eq. (6.7)) for different polymers: ZGH-1 (full line), ZGH-2 (dotted), ZGH-3 (dashed), ZGH-4 (dash-dotted) and ZGH-5 (dot-dot-dot-dashed).*

The different polymers used are denoted by different lines. To compare the theoretical with the measured surface pressure the polydispersity of the polymers should be taken into account. This was done by assuming the length of the tails to have a gaussian distribution with a polydispersity as given in table 6.1. The results are shown in fig. 6.4.

Qualitatively the measurements and the calculations are similar. Both the constant plateau height and the dependence of the tail length are reproduced. Quantitatively the plateau is more pronounced in the measurements. This might indicate that the polydispersity is less than assumed. Furthermore the plateau height in the measurements varies more than theoretically expected. This indicates a (small) dependence of the maximum of Φ_o on m, which can be due to the development of 'surface micelles' as shown for different systems by Meszaros et al. [61].

At small A_s, when the anchors get in touch (fig. 6.1d), the measurements stop because the surface pressure becomes larger than the surface tension of water. This happens at approximately the same A_s-value for the polymers used here (≤ 5 nm^2), which is of the same order as the square of the radius of gyration of PS (in this case approximately 1.7 nm).

6.5 Neutron reflectivity measurements

With neutron reflection experiments it is possible, if the contrast is large enough, to give quantitative information about the volume-fraction profile, and then a more quantitative comparison with theory is possible. To be able to measure the volume-fraction profile the contrast between polymer and solution should be as large as possible. Therefore, the water used was deuterated. The scattering-length density of heavy water is much larger than of normal water (see table 2.1). The scattering-length density of styrene and ethylene oxide is 1.76×10^{-3} and 0.75×10^{-3} nm^{-2}, respectively. The contrast is determined mainly by the 'gap' in the water, caused by the tails of the polymers. The model used for the scattering-length-density profile is:

$$\begin{array}{lll} \Gamma(z) = 0 & z < 0 & , \\ \Gamma(z) = \Gamma_b - \frac{3}{2}(\Gamma_b - \Gamma_e)\bar{\Phi}(1 - z^2/H^2) & 0 \leq z \leq H & , \\ \Gamma(z) = \Gamma_b & z > H & , \end{array} \tag{6.8}$$

where Γ_b is the scattering-length density of heavy water and Γ_e the scattering-length density of (poly)ethylene oxide. An example for $\bar{\Phi} = 0.1$ and $H = 50$ nm is shown in fig. 6.5. The gap is not very large, so very accurate measurements must be performed. The gap is proportional to $\bar{\Phi}$, so for smaller values it becomes less visible. The dashed line represents the actual scattering-length density of the polymer if the PS anchors and the PEO monolayer are not ignored. The solid line is the model where the PS anchors and the PEO monolayers are modelled by a roughness at the surface. The difference in detail due to negligence of anchors and

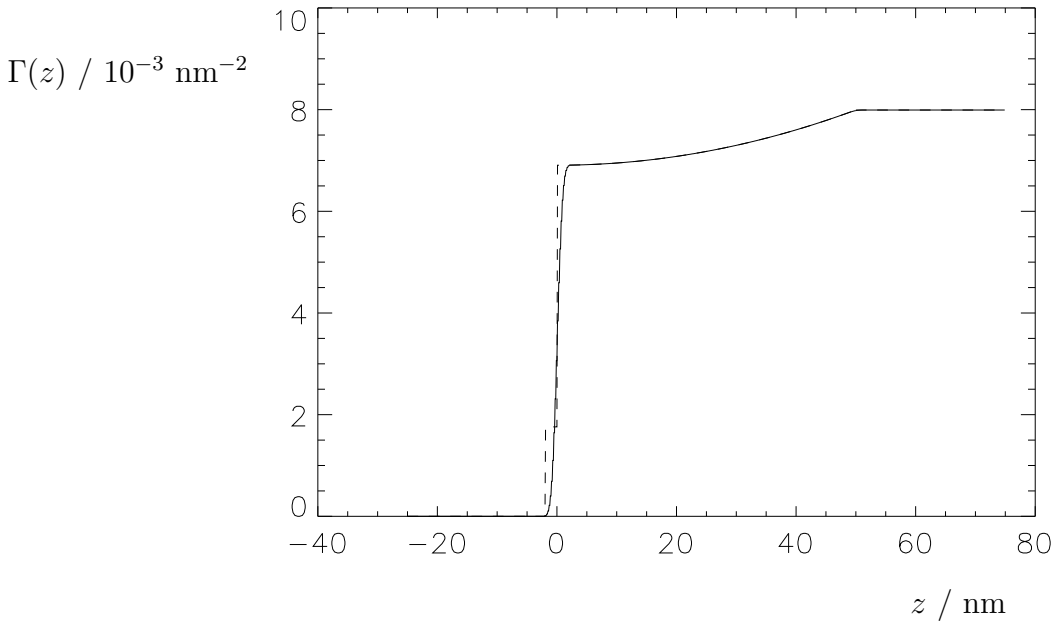

Figure 6.5: *Example of a scattering-length-density profile for* $\bar{\Phi} = 0.1$ *and* $H = 50$ *nm. Fitted (solid line) and actual profile (dashed).*

monolayer is hardly visible. Because the anchors and the monolayer are hardly visible the neutron reflection experiments can only be performed in the region where the brush is well developed.

The reflection angle for the neutron reflectivity measurements was set at 15.0 mrad. At this angle the minimum wavelength for total reflection from D_2O is 1.05 nm. The frame-overlap mirror was set at -21 mrad, giving a maximum wavelength in the incident beam of 1.2 nm. Hence, the wavelength region between 1.1 and 1.2 nm could be used to normalize the reflectivity to 1. The correction factor was typically 0.83. This differs from 1 because the diaphragm in front of the detector was set a little too narrow. The flight path of the neutrons from chopper to detector was 5355 mm. The chopper frequency was set at 25 Hz, so that in the wavelength region between 1.2 nm and 1.5 nm only the background countrate was recorded, which was 0.015 neutrons/s. The diaphragms 1 and 2 were set at 3 and 1 mm respectively, giving a footprint of 106 mm and an angular resolution of 2 % (standard deviation). The measuring time per experimental condition was approximately 7 hours. An example of a reflection experiment for pure D_2O and ZGH-5 with $A_s = 6.4$ nm^2 is shown in fig. 6.6. The lines are fits of the model to these measurements. For the ZGH-5 measurement clearly a bump is visible, indicating a layer.

The scattering-length-density profile was discretized in 20 layers of thickness $H/20$ nm, from which the reflectivity was calculated using eq. (2.34). The parameters that were fitted are Γ_b, $\bar{\Phi}$, H and the roughness at the surface, σ_s. The fit procedure is discussed in section 5.3. The errors in the parameters, defined

as 68.3 % confidence intervals, are calculated with eq. (5.18). The data could be fitted easily with the model as discussed above. The correlations (see section 5.5) between the fit parameters H and $\bar{\Phi}$ varied between -0.2 and -1. The best correlations were obtained at the smallest values of A_s. If $\bar{\Phi}H$ is less than 0.5 nm (corresponding to an adsorbed amount of approximately 0.6 mg/m^2) it is not possible to distinguish between a large $\bar{\Phi}$ and small H, or a small $\bar{\Phi}$ and a large H. In this case the correlation between the fit parameters H and $\bar{\Phi}$ is almost -1. For ZGH-2 only the measurement at the smallest A_s gave a solution where the absolute value of the correlation between the fit parameters was less than 0.9. Measurements on ZGH-1 were therefore omitted. The weighted mean-square deviation of the fits to the data, χ^2 varied between 1 and 2 for the different measurements. The roughness at the surface was fitted to be approximately 1 nm. The fitted average volume fractions and brush heights as a function of the available area per molecule are shown in figs. 6.7 and 6.8 respectively.

6.6 Discussion and conclusions

The lines shown in figs. 6.7 and 6.8 are calculated using eqs. (6.2) and (6.3), with $l = 0.39(3)$ nm and $p\nu = 0.04(1)$. Between parentheses the 68.3 % confidence interval is given. It is determined by a fit of all $\bar{\Phi}$- and H-values, shown in figs. 6.7 and 6.8. Even for the large range in the tail length as used here, the theory can describe the data quite well. Note that the independence of $\bar{\Phi}$ on the length of the tail is reproduced remarkably well. Also the linear dependence of the brush height on the tail length is found. The values found for l and $p\nu$ are in agreement with the literature values for the bond length of ethylene oxide $l = 0.33$ nm, and $\chi = 0.45$ [49].

The deviations that are still visible can be due to a number of effects. First, the accuracy of A_s is limited by the sample preparation method (about 5 %). Second, the polydispersity gives rise to deviations. Because the exact distribution is not known, it is virtually impossible to take this into account. Third, the approximation introduced through eq. (6.1). If this approximation is not valid the volume-fraction profile will deviate from the parabolic profile and the fitted values of $\bar{\Phi}$ and H will differ from theory. For instance, if the excluded-volume parameter is very close to zero the volume-fraction profile changes to $\Phi(z) = 4\bar{\Phi}/\pi(1 - z^2/H^2)^{1/2}$ [53]. This profile was used to fit the data. It was found that this fits equally well and $\bar{\Phi}$ is the same. H is 10 % smaller than with the parabolic profile. However, theoretically both H and $\bar{\Phi}$ are proportional to $A_s^{-1/2}$, which is not reproduced by the measurements. It is not possible to get a good fit with a rectangular volume profile. Because the volume fractions are very small the measurements are not very sensitive to the exact shape of the volume-fraction profile, but the shape can not deviate too much from eq. (6.1). From close inspection of the reflectivity data there is an indication that the measurements contain more structure than the fit. This can be due to a deviation

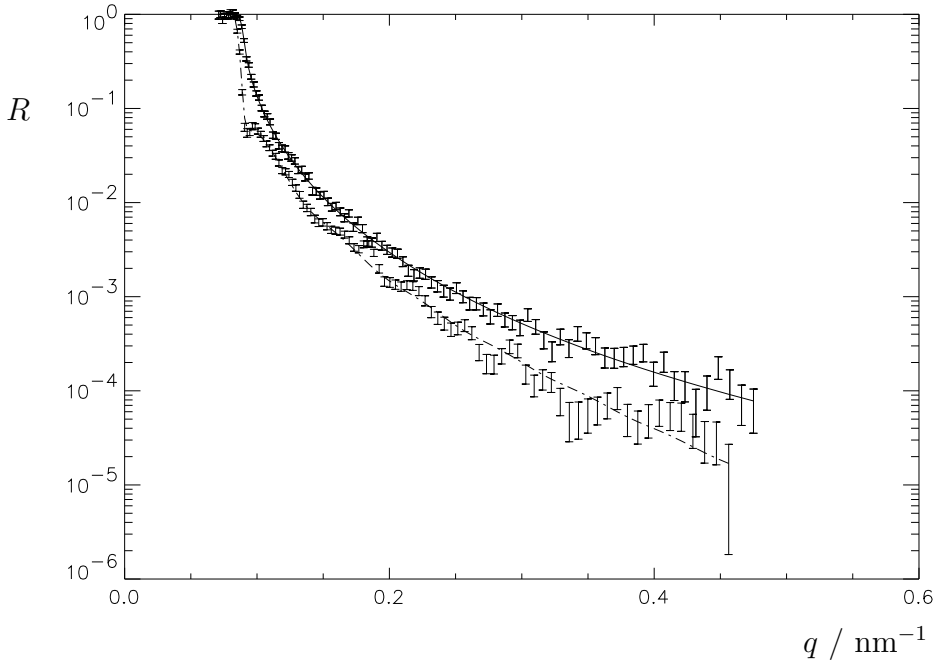

Figure 6.6: *Reflectivity, R as a function of the vertical component of the wavevector, q for D_2O (error bars, full line) and ZGH-5 with 6.4 nm^2 per molecule (error bars, dashed line). The lines represent fits of the model to the data, with $\bar{\Phi}$ =0.09 and H = 47 nm.*

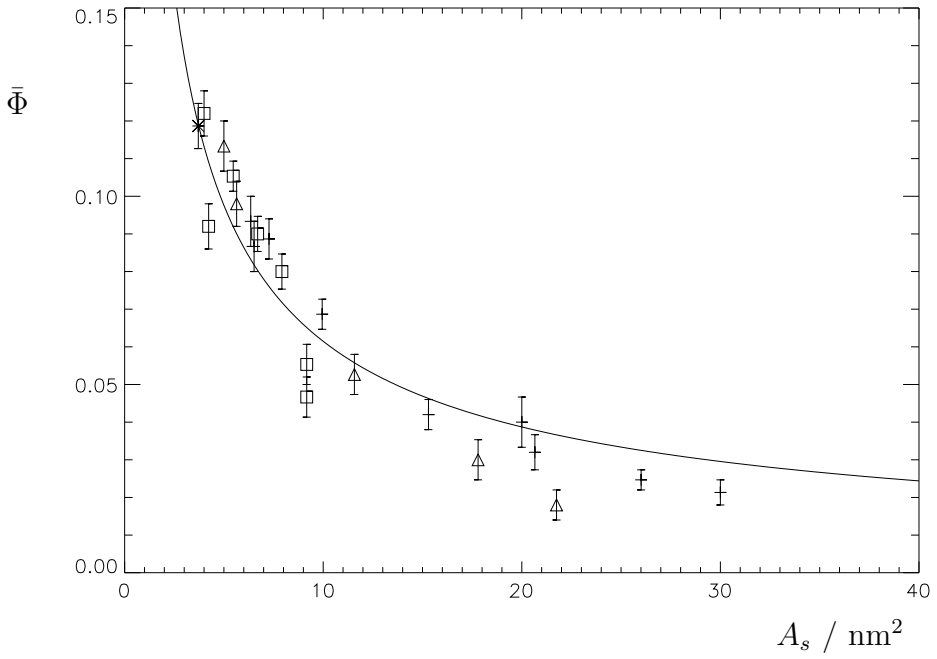

Figure 6.7: *Average volume fraction, $\bar{\Phi}$ as a function of available area per molecule, A_s for different polymers: ZGH-2 (asterisk); ZGH-3 (squares); ZGH-4 (triangles); ZGH-5 (plusses). The line corresponds to the model as described in the text.*

of the real volume profile from the parabolic volume profile which was assumed here. However, the statistics of the measurement do not allow a more quantitative analysis of these deviations. If more information about the volume-fraction profile is required, measurements extending to larger q-values must be performed. Last possibility is the negligence of the PS anchors and the PEO monolayer in the scattering-length-density profile, although this is a relatively small effect.

Here it is shown that with neutron reflection experiments it is possible to get quantitative information about the volume-fraction profiles of terminally-attached diblock copolymers. The self-consistent field theory describes the dependence of the volume-fraction profile on the length of the tails and the available area per molecule within the statistics of the measurements. For a better quantitative comparison of the theory with experiments it is necessary that the sample preparation is controlled better. Especially the concentration of the dissolved polymers must be controlled better. A smaller dispersity would also be beneficial.

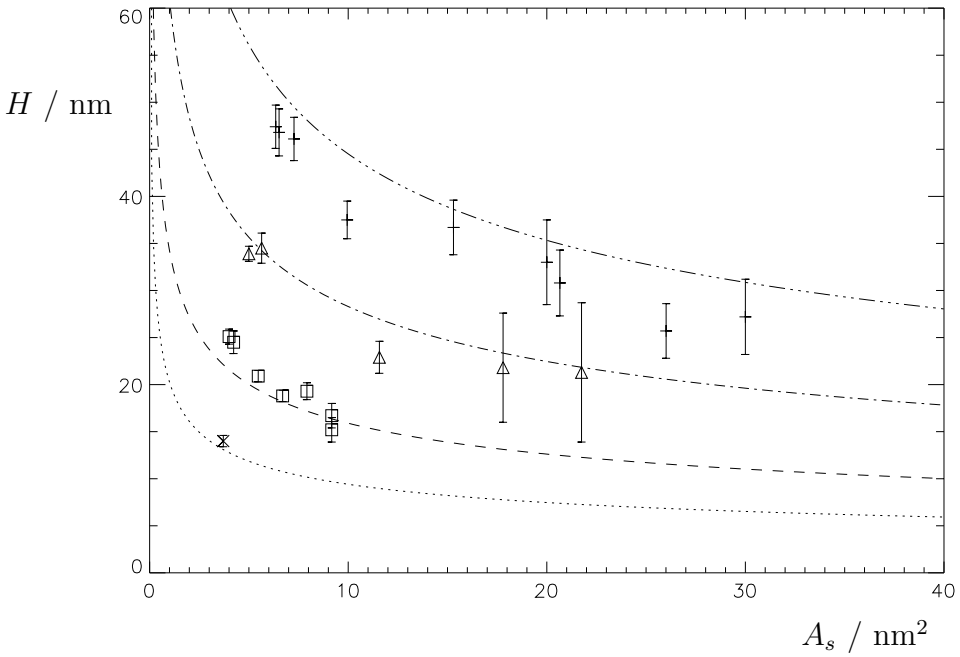

Figure 6.8: *Brush heights, H as a function of available area per molecule, A_s for different polymers: ZGH-2 (asterisk, dotted line); ZGH-3 (squares, dashed line); ZGH-4 (triangles, dash-dotted line); ZGH-5 (plusses, dot-dot-dot-dashed line). The lines correspond to the model as described in the text.*

Chapter 7

Concluding remarks

Knowledge, wisdom of Mind,
Love, wisdom of Heart,
Hope, wisdom of Life.

From the research described in this thesis it can be concluded that even at a moderate-flux reactor as the Hoger Onderwijs Reactor of IRI it is possible to perform good neutron reflectivity measurements. An important criterion is the relation between the neutron intensity at the sample position and the resolution of the reflectometer. For ROG this relation was optimized by the use of a double-disk chopper and neutron guides. Another important criterion is the background countrate introduced by gamma radiation and fast neutrons. The background countrate is mainly determined by the stacked neutron guide, which has a very low gamma radiation and fast neutron flux. It is possible to measure reflectivities down to 10^{-5}, if no other sources of background are present. An annoyance can be the background produced by other set-ups in the vicinity of ROG. The production of background radiation must be prevented or it must be properly shielded, because the background directly influences the smallest attainable reflectivity. The reflectivity can be determined within 5 % by measuring the incoming beam with a monitor and the reflected beam with a detector, after corrections for background countrate, dead time, efficiencies and transmissions. Corrections for the scattering of the air in the flight path between the monitor and detector are applied.

The position-sensitive detector enables the measurement of off-specular reflection. From off-specular reflection data it is possible to obtain information about the lateral structure of the surface of a sample. Again a small background countrate is important. The position-sensitive detector uses a scintillator to convert a neutron into a a light pulse. A scintillator is very sensitive to gamma radiation. The electronic system used to detect the pulses reduces the background countrate considerably using position-dependent lower- and upper pulse-height

discrimination levels. Hence, even with the position-sensitive detector it is possible to measure (off-specular) reflectivities down to 10^{-5}. The resolution of the position-sensitive detector is determined by the type of scintillator and the electronics used. For the system used here the standard deviation is approximately 0.75 mm.

Inversion of neutron reflectivity data is not straightforward. Due to the loss of phase information in a reflectivity measurement the solutions are not unique. Care must be taken that the sample is not totally unknown, because without a-priori knowledge about the structure of the sample it is impossible to give a unique solution for the scattering-length-density profile. Most of the time sufficient a-priori knowledge can be taken into account to attain a good and reliable scattering-length-density profile. Genetic Algorithms can be used as fit procedure for neutron reflectivity data. The (expected) scattering-length-density is parameterized in a model. With Genetic Algorithms a set of parameters which agree with the data can be found in a robust way. Also it is possible to get an idea about the non-uniqueness of the solution from the global correlations. Local correlations between parameters can be found by linearizing the solution and using the law of propagation of errors.

In this thesis it is shown that retrieval of phase information is in principle possible. This gives the possibility of directly calculating the scattering-length-density profile from the Gel'fand-Levitan equations. In the future measurements must be performed to prove this. The inversion calculations must be applied and the influence of statistics and resolution will have to be investigated.

ROG has the possibility to measure magnetic samples. Therefore the neutron beam must be polarized. This is possible with the super mirror. The handling of the polarized neutron beam and the correction and interpretation of polarized neutron reflectivity data goes beyond the scope of this thesis. More information is given in [62] and will be given by A. van der Graaf [63].

It is shown that with neutron reflection experiments it is possible to get quantitative information about the volume-fraction profiles of terminally-attached diblock copolymers. The self-consistent field theory describes the dependence of the volume-fraction profile on the length of the tails and the available area per molecule within the statistics of the measurements. For a better quantitative comparison of the theory with experiments it is necessary that the sample preparation is controlled better. Especially the concentration of the dissolved polymers must be controlled better. A smaller dispersity would also be beneficial.

Bibliography

[1] J.B. Hayter, R.R. Highfield, B.L. Pullman, R.K. Thomas, A.I. McMullen and J. Penfold, J. Chem. Soc. Faraday Trans. 1, **77** (1981) 1437.

[2] M. Stamm, S. Hüttenbach and G. Reiter, Physica B **173** (1991) 11.

[3] E.M. Lee, C.F. Majkrzak, M. Elmiger and L. Passell, Nucl. Instrum. Methods in Phys. Res. B **93** (1994) 75.

[4] J. Penfold, Physica B **173** (1991) 1.

[5] G.P. Felcher, R.O. Hilleke, R.K. Crawford, J. Haumann, R. Kleb and G. Ostrowski, Rev. Sci. Instrum. **58** (1987) 609.

[6] A. Karim, B.H. Arendt, R. Goyette, Y.Y. Huang, R. Kleb and G.P. Felcher, Physica B **173** (1991) 17.

[7] H. Zabel, I.K. Robinson, editors 'Surface X-Ray and Neutron Scattering', (Springer-Verlag, Berlin Heidelberg, 1992).

[8] H.J. Lauter, V.V. Pasyuk, editors 'Proceedings of the International Conference on Surface X-Ray and Neutron Scattering SXNS-3', Physica B **198** (1994) 1-266.

[9] V.F. Sears, 'Neutron Optics', (Oxford University press, Oxford, 1989).

[10] J. Lekner, 'Theory of reflection', (Martinus Nijhof publishers, Dordrecht, 1987).

[11] V.F. Sears, Neutron News **3** (1992) 26.

[12] S.W. Lovesey, 'Theory of neutron scattering from condensed matter', Volume 2, (Clarendon Press, Oxford, 1984).

[13] L.G. Parratt, Phys. Rev. **95** (1954) 359.

[14] T. Fokkema and A. Ziolkowski, Geophysics **52** (1987) 965.

[15] S.K. Sinha, E.B. Sirota, S. Garoff and H.B. Stanley, Phys. Rev. B **39** (1988) 2297.

[16] P. Beckmann and A. Spizzichino, 'The Scattering of Electromagnetic Waves from Rough Surfaces', (MacMillan, New York, 1963).

[17] L. Névot and P. Croce, Rev. Phys. Appl. **15** (1980) 761.

[18] J. Penfold and R.K.Thomas, J. Phys. Condens. Matter **2** (1990) 1369.

[19] G.P. Felcher, (submitted to Phys. B);
A. Karim, N. Singyh, M. Sikkak, F. Bates, W.D. Dozier and G.P. Felcher, (submitted to J. Chem. Phys.);
H. Dosch, 'Critical phenomena at surfaces and interfaces', Springer tracts in modern physics vol. 126 (Springer-Verlag, Berlin Heidelberg, 1992).

[20] R.A. Cowley and T.W. Ryan, J. Phys. D Appl. Phys. **20** (1987) 61.

[21] D.K.G. de Boer, Phys. Rev. B **49** (1994) 5817.

[22] H.E. Moses, Phys. Rev. **102** (1956) 559;
R.G. Newton, SIAM Rev. **12** (1970) 346;
B.N. Zakhariev, A.A. Suzko, 'Direct and Inverse Problems', (Springer-Verlag, Heidelberg, 1990);
T.M. Roberts, Physica B **173** (1991) 143.

[23] R.E. Burge, M.A. Fiddy, A.H. Greenaway and G. Ross, Proc. R. Soc. Lond. A **350** (1976) 191.

[24] E.J. Kramer, Physica B **173** (1991) 189.

[25] T.L. Crowley, E.M. Lee, E.A. Simister, R.K. Thomas, Physica B **173** (1991) 143.

[26] D.S. Sivia and R. Pynn, SPIE **1738** (1992) 305.

[27] C.F.Majkrzak, N.F. Berk, J.F. Ankner, S.K. Satija and T.P. Russell, SPIE **1738** (1992) 282.

[28] D.S. Sivia, W.A. Hamilton, G.S. Smith, Physica B **173** (1991) 121.

[29] X.L. Zhou and S.H. Chen, Phys. Rev. E **47** (1993) 3174.

[30] P. Verkerk, A.A. van Well and M.Th. Rekveldt, Physica B **156** & **157** (1989) 544;
A.A. van Well, V.O. de Haan and M.Th. Rekveldt, Neutron News **3** (1991) 28;
A.A. van Well, Nucl. Sci. Engineer. **110** (1992) 10.

[31] V.O. de Haan, W.H. Kraan, A.A. van Well, Nucl. Instrum. Methods in Phys. Res. A **289** (1990) 17.

[32] A.A. van Well, Physica B **180** & **181** (1992) 959.

[33] O. Schaerpf, N. Stuesser, Nucl. Instrum. Methods in Phys. Res. A **284** (1989) 208.

[34] O. Schaerpf, Physica B **156** & **157** (1989) 639.

[35] J.R.D. Copley, Journ. of Neutron Research **1** (1993) 21.

[36] P.T. Por, W.H. Kraan, M.Th. Rekveldt, Nucl. Instrum. Methods in Phys. Res. A **339** (1994) 550.

[37] R. Kurz, R. Reinartz, S. Widdau, J. Schelten, A. Scholz and W. Schaefer, Nucl. Instrum. Methods in Phys. Res. A **273** (1988) 273.

[38] I.Naday and W. Schaefer, 'A new processing method and gain stabilization for scintillation position-sensitive detectors', (Academic Press, London, 1983).

[39] J. de Blois, P. van der Ende, V.O. de Haan, E.A. Osterholt and M.N. Schipper, 'The electronic system of the IRI neutron reflectometer ROG', report IRI-132-94-12 (Delft, 1994).

[40] J. de Blois, J. Alberts, E.A. Osterholt and M.N. Schipper, 'VME data handling module (VME-DHM)', report IRI-132-93-12 (Delft, 1993); J. de Blois, J. Alberts, V.O. de Haan, E.A. Osterholt and M.N. Schipper, 'A VME Position Sensitive Detector input module for a 64 Mb dual ported memory (PSDinp)', report IRI-132-94-09 (Delft, 1994).

[41] C.L. Thaper, P.S. Goyal and B.A. Dasannacharya, Pramāna **23** (1984) 313.

[42] D.J. Hughes, B.A. Magurno and M.K. Brussel, 'Neutron Cross Sections', (Brookhaven National Laboratory, New York, 1960).

[43] M.S. Sambridge and G.G. Drijkoningen, Geoph. J. Ind. **109** (1992) 323.

[44] N.R. Draper, H. Smith, 'Applied Regression Analysis', 2nd edition, (John Wiley & Sons, New York, 1981).

[45] J.H. Holland, Scientific American, July 1992.

[46] D. E. Goldberg, 'Genetic Algortihms in Search Optimization & Machine Learning', (Addison-Wesley Publ., USA, 1989).

[47] C.M. Messelaar, 'Calibration samples for ROG', (report IRI 132-92-04, Interfacultair Reactor Instituut, Delft University of Technology, Delft, 1992).

[48] B.R. Martin, 'Statistics for Physicists', (Academic Press, London and New York, 1971).

[49] G.J. Fleer, M.A. Cohen Stuart, J.M.H.M. Scheutjens, B. Cosgrove and B. Vincent, 'Polymers at Interfaces', (Chapman & Hall, London, 1993).

[50] A. Ulman, 'Ultrathin organic films', (Academic Press, INC., San Diego, 1991).

[51] P.G. de Gennes, J. Phys. (Paris) **37** (1976) 1445; P.G. de Gennes, Macromolecules **13** (1980) 1069.

[52] J.M.H.M. Scheutjens, G.J. Fleer, Phys. Chem. **83** (1979) 1619; J.M.H.M. Scheutjens, G.J. Fleer, J. Phys. Chem. **84** (1980) 178.

[53] C.M. Wijmans, 'Copolymers at the Solid-Liquid Interface', (Ph. D. Thesis Wageningen, 1994); C.M. Wijmans, Macromolecules **25** (1992) 2567.

[54] Z. Hruska, G. Hurtrez, S. Walter and G. Riess, Polymer **33** (1992) 2447.

[55] G.L. Gaines Jr.,'Insoluble monolayers at liquid-gas interfaces', (Interscience Publishers, John Wiley & Sons, New York, 1966).

[56] B.B. Sauer and H. Yu, Macromolecules **22** (1989) 786.

[57] J.E. Glass, J. Phys. Chem. **72** (1968) 4459.

[58] J.A. Henderson, R.W. Richards, J. Penfold, R.K. Thomas and J.R. Lu, Macromolecules **26** (1993) 4591.

[59] R.W. Richards, B.R. Rochford and J.R.P. Webster, Faraday Discuss. **98** (1994) (in press).

[60] M. Mellema, (MSc. Thesis Wageningen, 1995).

[61] M. Meszaros, A. Eisenberg and R.B. Lennox, Faraday Discuss. **98** (1994) (in press).

[62] V.O. de Haan, J. de Blois, P. van der Ende, H. Fredrikze, A. van der Graaf, M.N. Schipper, A.A. van Well and J. van der Zanden, Nucl. Instrum. Methods in Phys. Res. A (accepted).

[63] A. van der Graaf, (Ph. D. Thesis Delft, 1996) (in preparation).

[64] G.E. Bacon, 'Neutron diffraction', third edition, (Oxford 1975).

[65] M.Th. Rekveldt, P. Verkerk and A.A. van Well, Nucl. Instrum. Methods B **34** (1988) 285.

[66] A.A. van Well, V.O. de Haan and H. Fredrikze, Physica B **198** (1994) 217.

Appendix A

Flight path determination

To determine the wavelength of the neutrons detected with the time-of-flight system, the length of the flight path of the neutrons must be known. The flight path is determined by the position of the short frame relative to that of the long frame and by the positions of the chopper, monitor and detector on these frames. ROG is constructed in such a way that the positions of the short and long frame can automatically be adjusted to manipulate the neutron beam. For the positioning of the long frame in its extreme positions two screw jacks are used. Here the essential dimensions for the determination of the flight path of the neutron over the short and long frame are described. The relations between the different dimensions are given and the flight path is calculated.

In figure A.1 a schematic view of ROG is shown. Left the short frame on legs 1 (EE') and 2 (DD') and right the long frame on legs 3 (AA') and 4 (BB') are shown. The origin of the coordinate system is chosen to be at O. The short

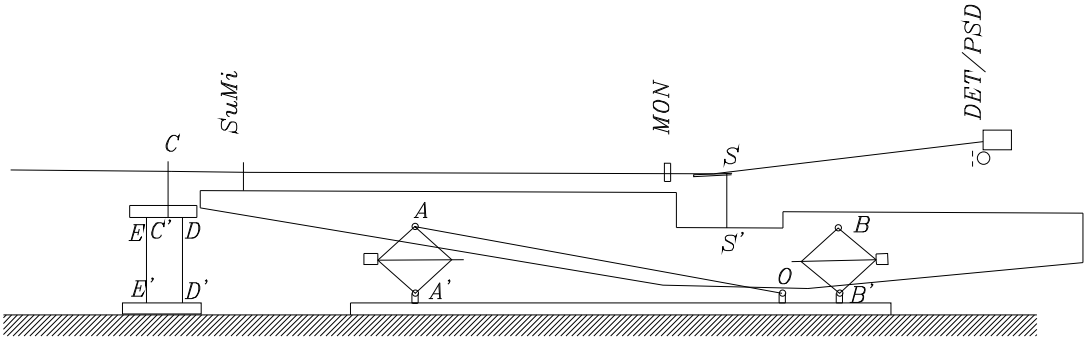

Figure A.1: Schematic view of ROG

frame supports the chopper. E is the point the table of the short frame rotates around. D is the other support point. E' and D' are the projections of E and D on the line $y = 0$. The position of the hole in the chopper determining the beginning of the flight path is denoted as C. C' is the projection of C on the line ED. The lengths of leg 1 (EE') and 2 (DD') can be adjusted using a DC-motor. The directions of leg 1 and 2 are always vertical. The angle of the short frame with the horizontal is denoted as α. The long frame is supported by leg 3

(AA') and 4 (BB'). Legs 3 and 4 can be varied in length using a DC-motor and rotate around A and A' and B and B' respectively. Legs 3 and 4 are constructed using a diamond construction. The length of the sides of the diamond, $L_\diamond$ are fixed, so by changing the length of one diagonal the length of the other diagonal is also changed. The bar between O and A is used to fix the position of the frame and rotates around O and A. S denotes the position of the sample. S' is the projection of S on AB. SuMi denotes the position of the super mirror, which is used to reflect the neutron beam with glancing angle γ. MON and DET denote the positions of the monitor and the detector respectively. The angle of the long frame with the horizontal is denoted as ν. The relation between the angles mentioned above is (see also fig. A.2)

$$\alpha = \nu - 2\gamma \tag{A.1}$$

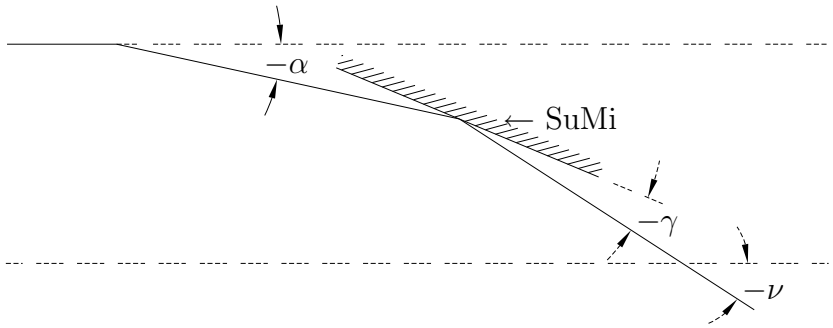

Figure A.2: Definition of and relation between used angles.

In the calculations described here the following symbol convention is used

- x_P : x coordinate of point P
- y_P : y coordinate of point P
- PQ : Distance between points P and Q
- H_i : Length of leg i (e.g. H_3 = AA'), 'vertical' diagonal
- D_i : Length of motor axis of leg i, 'horizontal' diagonal

For the short frame the next equations hold:

$$H_1 = y_E \qquad H_2 = y_D \tag{A.2}$$

$$x_C = -OE' + EC' \cos\alpha - CC' \sin\alpha \tag{A.3}$$

$$y_C = y_E + EC' \sin\alpha + CC' \cos\alpha \tag{A.4}$$

$$y_D = y_E + E'D' \tan\alpha \tag{A.5}$$

For the long frame:

$$H_3 = \sqrt{4L_\diamond^2 - D_3^2} \qquad H_4 = \sqrt{4L_\diamond^2 - D_4^2} \tag{A.6}$$

$$x_A = \frac{H_3^2 - AO^2 - A'O^2}{2A'O} \qquad y_A = \sqrt{AO^2 - x_A^2} \tag{A.7}$$

$$k_1 = \frac{B'O - x_A}{y_A} \qquad k_2 = \frac{H_4^2 + AO^2 - AB^2 - B'O^2}{2y_A} \tag{A.8}$$

$$A = 1 + k_1^2 \qquad B = 2(k_1 k_2 - B'O) \qquad C = B'O^2 + k_2^2 - H_4^2 \tag{A.9}$$

$$x_B = \frac{-B + \sqrt{B^2 - 4AC}}{2A} \qquad y_B = k_1 x_B + k_2 \tag{A.10}$$

$$x_B = x_A + AB\cos\nu \qquad y_B = y_A + AB\sin\nu \tag{A.11}$$

$$x_S = x_A - SS'\sin\nu + AS'\cos\nu \qquad y_S = y_A + SS'\cos\nu + AS'\sin\nu \tag{A.12}$$

$$x_{\mathrm{SuMi}} = x_S - L_{\mathrm{SuMiSAM}}\cos\nu \qquad y_{\mathrm{SuMi}} = y_S - L_{\mathrm{SuMiSAM}}\sin\nu \tag{A.13}$$

L_{SuMiSAM} is the distance along the long frame between the super mirror and the sample position. For the length of the flight path of the detector L_{TOFDET} and monitor L_{TOFMON}, the distance between the chopper and the super mirror, L_{ChopSuMi} must be calculated

$$L_{\mathrm{ChopSuMi}} = \sqrt{(x_{\mathrm{SuMi}} - x_C)^2 + (y_{\mathrm{SuMi}} - y_C)^2} \tag{A.14}$$

Also the distance between sample and detector L_{SAMDET} and the distance between sample and monitor L_{SAMMON} must be known. Then:

$$L_{TOFDET} = L_{\mathrm{ChopSuMi}} + L_{\mathrm{SuMiSAM}} + L_{\mathrm{SAMDET}} \tag{A.15}$$

$$L_{TOFMON} = L_{\mathrm{ChopSuMi}} + L_{\mathrm{SuMiSAM}} - L_{\mathrm{SAMMON}} \tag{A.16}$$

L_{SAMDET} depends on the position of the detector or PSD and is given by

$$L_{SAMDET} = \sqrt{\mathrm{DetTz}^2 + (\mathrm{DetTx} + \Delta\mathrm{DetTx})^2 + \Delta\mathrm{DetTy}^2}, \tag{A.17}$$

where DetTz equals the distance along the frame between sample and detector, DetTx equals the distance perpendicular to the frame between sample and the middle of the diaphragm in front of the detector and ΔDetTx and ΔDetTy equal the offsets due to the detection position on the PSD.

Short frame

Name	Value [mm]	Description
OE'	5117	Horizontal distance between leg 1 (EE') of short frame and axis of stabilizer rod (AO)
EC'	203	Horizontal distance between leg 1 of short frame and middle of beam in chopper, when short frame is horizontal
CC'	320	Distance from middle of beam in chopper to plane through supporting points (E and D) of short frame
E'D'	290	Horizontal distance between leg 1 and 2 of short frame

Long frame

Name	Value [mm]	Description
$L_{\diamond}$	400	Length of side of diamond supporting long frame
AO	3000	Length of stabilizer rod (AO)
A'O	2940	Horizontal distance between leg 3 (AA') and axis of stabilizer rod
B'O	460	Horizontal distance between leg 4 (BB') and axis of stabilizer rod
AB	3400	Distance between points where leg 3 and 4 support frame
SS'	431	Distance from sample to plane through support points long frame
AS'	2400	Distance along long frame between sample and point where leg 3 supports frame
L_{2S}	405	Distance between Dia2 and middle of sample
L_{SuMiSAM}	3740	Distance between middle of SuMi and sample
L_{SAMMON}	340	Distance between middle of monitor and sample
L_{SAMDET}	variable	Distance between detector and sample
X_{source}	-7138	x-position of assumed neutron source
Y_{source}	1013	y-position of assumed neutron source

Table A.1: Dimensions of ROG

Appendix B

Falling neutrons in reflectometers

The effect of gravity on neutrons is in general taken into account only for very cold neutrons with wavelength larger than 100 nm. However, in the case of neutron reflection experiments in horizontal geometry, this effect becomes important for neutrons with wavelengths down to 1 nm. This is due to the fact that neutron reflection experiments are performed at small angles. It will be shown that the position where the neutron beam hits the sample depends on the wavelength of the neutrons. For standard geometries this shift is typically of the order of centimeters for neutrons of 2.5 nm. Also the position where the neutrons hit the detector varies with wavelength.

The schematic geometry for a horizontal neutron reflectometer is shown in fig. B.1. Two diaphragms (Dia1 and Dia2), with very narrow slits, are positioned at distances, x_1 and x_2 from the middle of the sample. Note that x_1 and x_2 are negative. The height of the diaphragms is given by $y_i = a_d x_i$, where a_d is the slope of the line through the two diaphragms and the middle of the sample. The sample is positioned with a slope a_s. The distance between the middle of the sample and the detector (DET) is x_d. In the calculations we assume perfect angular resolution, i.e. we will ignore the finite height of the slit diaphragms. Two trajectories of neutrons that can pass the diaphragms are shown in fig. 1. The straight line is the trajectory of neutrons without gravity effect. Before

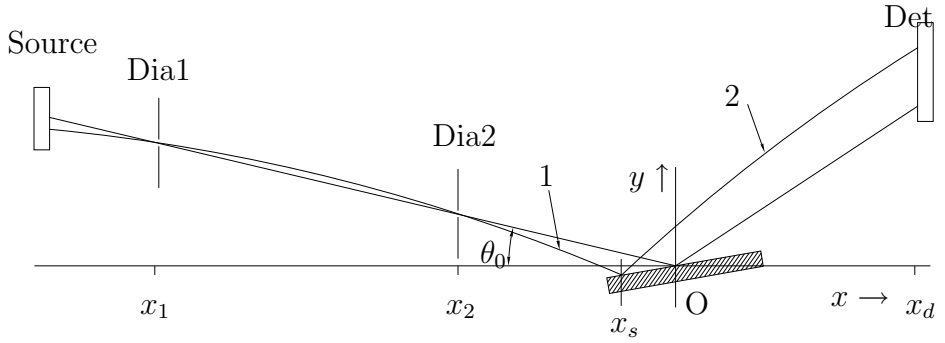

Figure B.1: Geometry of a horizontal reflectometer.

interaction with the sample the neutrons follow trajectory 1

$$y = -\frac{x^2 + x_1 x_2 - (x_1 + x_2)x}{4H} + a_d x \ , \tag{B.1}$$

and after reflection from the sample the neutrons follow trajectory 2

$$y = -\frac{(x - x_s)(x - 3x_s + x_1 + x_2)}{4H} + (2a_s - a_d)(x - x_s) + a_s x_s \ , \tag{B.2}$$

where $H = v^2/2g$, with v the (horizontal) velocity of the neutron and g the acceleration of gravity. H is equal to the maximum height a neutron with velocity v can reach in a constant gravity field and depends on the wavelength of the neutrons

$$H = H_o(\frac{\lambda_o}{\lambda})^2 \ , \tag{B.3}$$

with $H_o = 8$ km and $\lambda_o = 1.0$ nm. The position where the neutrons hit the sample is given by

$$x_s \approx -\frac{x_1 x_2}{4H(a_s - a_d)} \ , \tag{B.4}$$

assuming

$$\frac{4H \mid a_d - a_s \mid}{\mid x_1 + x_2 \mid} >> 1 \ . \tag{B.5}$$

In this first order approximation x_s is inversely proportional to the nominal glancing angle ($\theta_0 \approx a_s - a_d$). For the glancing angle is obtained

$$\theta \approx a_s - a_d - \frac{x_1 + x_2}{4H} \ , \tag{B.6}$$

which shows that to first order the gravitation effect introduces an increase $\Delta\theta$ of the glancing angle, independent of the nominal glancing angle. For the difference of detection position is obtained

$$\Delta y_d \approx -\frac{x_d^2 + x_d(x_1 + x_2) - x_1 x_2}{4H} \ . \tag{B.7}$$

For ROG x_1, x_2 are -3405, -405 mm respectively, x_d varies between 1000 and 2000 mm. The effects are summarized in table B.1.

From table B.1 it is concluded that for ROG the gravitation effect is of minor importance, because of the relatively fast neutrons that are used (usually only neutrons up to 1 nm are used). For small samples ($\approx$ 20 mm) the effect may be significant, if the collimation is matched to the size of the sample. For reflectometers using larger wavelengths this effect becomes considerably larger and should be accounted for. The difference in height in detection position can be neglected.

			$\theta_0 = 5$	$\theta_0 = 10$	$x_d = 1000$	$x_d = 2000$
λ / nm	H / km	$\Delta\theta$	x_s	x_s	Δy_d	Δy_d
0.10	800	0.0	-0.09	-0.05	0.0013	0.0016
0.15	355	0.0	-0.21	-0.11	0.0029	0.0035
1.0	8.00	0.1	-9.7	-4.7	0.13	0.16
1.5	3.55	0.2	-21.	-11.	0.29	0.35
2.5	1.28	0.7	-61.	-29.	0.82	1.0

Table B.1: List of the effects of gravity at ROG; angles are given in mrad and distances in mm.

Appendix C

Comparison between a time-of-flight and a monochromatic neutron reflectometer at a continuous neutron source[†]

In neutron reflection experiments the reflectivity, R as a function of the component of the wavevector perpendicular to the sample plane is measured. This component is given by

$$q = \frac{2\pi\theta}{\lambda} \quad , \tag{C.1}$$

where θ is the angle of incidence and λ the neutron wavelength. The wavevector can be changed by varying θ or λ. To determine the reflectivity the number of reflected neutrons is divided by the number of incident neutrons. The number of incident neutrons depends on the neutron source and the resolution of the instrument. The thermal neutron flux of a reactor is distributed according to a Maxwell spectrum given by [64]:

$$\psi(\lambda)d\lambda = 2\Phi_0 \frac{\lambda_T^4}{\lambda^5} \mathrm{e}^{-(\lambda_T/\lambda)^2} d\lambda \ , \tag{C.2}$$

with $\lambda_T = \sqrt{h^2/2m_n kT}$ where h is Planck constant, k Boltzmann constant, m_n the neutron mass and T the temperature of the moderator. λ_T varies between 0.12 nm (hot source) and 0.35 nm (cold source). Φ_0 is the total thermal neutron flux. Usually a neutron filter has to be used to reduce the fast neutron and gamma

[†]This appendix is published as: 'Comparison between a time-of-flight and a monochromatic neutron reflectometer at a continuous source', V.O. de Haan and A.A. van Well, J. Neutron Research (accepted).

fluxes. Also the divergence of the neutron beam has to be taken into account, resulting in an extra transmission factor for the slow neutron flux, $\Xi(\lambda)\Delta\theta(\lambda)$. If we consider a reflectometer with horizontal sample, $\Delta\theta(\lambda)$ is the vertical divergence of the beam accepted by the instrument downstream of the neutron filter. $\Xi(\lambda)$ comprises the horizontal divergence of the beam and if as filter a neutron guide is used [31],[65] (favourable for both instruments), is approximately proportional to λ.

According to equation (C.1) the resolution of the instrument is given by the spread in the incident angle $\Delta\theta$ and the spread in the wavelength $\Delta\lambda$:

$$(\frac{\Delta q}{q})^2 = (\frac{\Delta\theta}{\theta})^2 + (\frac{\Delta\lambda}{\lambda})^2. \tag{C.3}$$

In the following calculations the relative resolution, $\rho = \Delta q/q$ was kept constant. Both resolution contributions of the above equation were matched to get the best performance regarding the resolution-intensity relation, so $\Delta\theta/\theta = \Delta\lambda/\lambda = \rho/\sqrt{2}$. In this case the same shape of the resolution is assumed for both instruments.

For a monochromatic neutron reflectometer the wavelength λ_m is constant and θ is varied. The wavelength is determined by Bragg reflection from a crystal with reflectivity $R_c(\lambda)$ given a spread in wavelength of $\Delta\lambda_m$. In the following $R_c(\lambda_m)$ is assumed to be 1. The effect of the filter to be used to suppress higher order Bragg reflections is neglected. For each angle $\theta_m(i)$ during some period $t_m(i)$ the number of reflected neutrons, $C_m(i)$ is counted. Each angle corresponds to a specific wavevector $q_m(i)$. For each measurement the divergence of the incident beam $\Delta\theta_m(i)$ is adjusted proportional to the angle accepted by the instrument. Then,

$$C_m(i) = \psi(\lambda_m)\Delta\lambda_m\Xi(\lambda_m)\Delta\theta_m(i)A_m(i)R(q_m(i))t_m(i) \quad , \tag{C.4}$$

where $A_m(i)$ is the cross section of the beam, proportional to $\Delta\theta_m(i)$. In this comparison it is assumed that the sample is larger than the footprint of the beam.

For a time-of-flight neutron reflectometer the incident angle and its spread is constant (given by θ_t and $\Delta\theta_t$ respectively) and the wavelength is varied. The continuous beam emerging from the neutron source is pulsed by a double disk chopper. In this comparison it is explicitly assumed that a double-disk chopper [32] is used to produce the pulsed neutron beam. Then, the burst time is proportional to the wavelength and does not depend on the rotational speed of the chopper. The transmission of this chopper is given by [32]:

$$T_c(\lambda) = f z_0 \frac{m_n}{h}\lambda \quad , \tag{C.5}$$

where f is the pulse frequency and z_0 the distance between the disks. The upper limit of f is given by the effect of duty-cycle overlap. If duty-cycle overlap occurs slow neutrons of the previous pulse are counted as fast neutrons in the current pulse. It can be shown that the upper limit of the frequency is given by $f_{max} =$

$h/(m_n(\lambda_{max}-\lambda_{min})L)$, with L the length of the flight path and λ_{min} and λ_{max} the minimum and maximum wavelength of the neutrons present in the beam. λ_{min} and λ_{max} can be adjusted freely by appropriate filters (e.g. by mirrors used in reflection and transmission geometry respectively [66].) to select the q-range. The wavelength resolution of the chopper is proportional to the wavelength, $\Delta\lambda_c = \lambda z_0/L$. Hence, for the transmission is found

$$T_c(\lambda) = \frac{\Delta\lambda_c}{\lambda_{max} - \lambda_{min}} \quad . \tag{C.6}$$

The reflected neutrons are detected in a multi-channel analyzer. Each channel i corresponds to the time-of-flight of the detected neutron, and through its wavelength, $\lambda_t(i)$ to a specific wavevector $q_t(i)$. During some period t_t the number of reflected neutrons in each channel, $C_t(i)$ is counted. The width of the time-of-flight channels gives rise to a spread in the wavelength $\Delta\lambda_t(i)$, but as long as $\Delta\lambda_t(i) \ll \Delta\lambda_c$ this can be ignored. Then,

$$C_t(i) = \psi(\lambda_t(i))\Delta\lambda_t(i)\Xi(\lambda_t(i))\Delta\theta_t T_c(\lambda_t(i))A_t R(q_t(i))t_t \quad , \tag{C.7}$$

where A_t is the constant beam cross section.

The comparison made here concerns the reflectivity for a finite q-range measured with both methods. The interesting quantity is the ratio between the total measuring time for each method given the same resolution and accuracy of the measurement. Matching the resolution gives for the monochromatic instrument $\Delta\theta_m(i) = \rho\theta_m(i)/\sqrt{2}$, $\Delta\lambda_m = \rho\lambda_m/\sqrt{2}$ and $A_m(i) = A_t\theta_m(i)/\theta_t$. For the time-of-flight instrument this gives $\Delta\theta_t = \rho\theta_t/\sqrt{2}$ and $\Delta\lambda_c = \rho\lambda/\sqrt{2}$. An advantage of a monochromatic instrument is that the relative standard deviation of the reflectivity, determined by $C_m(i)$, can be made the same for each q value by adjusting the measuring time accordingly. However, with a reflection experiment $C_t(i)$ does not change very much, because when the neutron flux decreases for larger wavelengths, the reflectivity increases. The accuracy of the reflectivity is determined by the total number of reflected neutrons counted. Matching the accuracy gives:

$$C_m(i) = C_t(i) \quad . \tag{C.8}$$

The ratio of the total measuring times is calculated using this condition and eqs. (C.4) and (C.7), keeping in mind that $q_m(i) = q_t(i)$:

$$\frac{t_m}{t_t} = t_t^{-1}\sum_{i=1}^{n} t_m(i) = \frac{(\lambda_{max} - \lambda_{min})^{-1}\sum_{i=1}^{n}\psi(\lambda_t(i))\Xi(\lambda_t(i))\lambda_t(i)^3\Delta\lambda_t(i)}{\psi(\lambda_m)\Xi(\lambda_m)\lambda_m^3} \quad , \tag{C.9}$$

where n is the total number of time-of-flight channels. If $\Delta\lambda_t(i)$ is small then the sum in this equation can be replaced by an integral over the wavelength range, giving an average:

$$\frac{t_m}{t_t} = \frac{<\Pi(\lambda)>}{\Pi(\lambda_m)} \quad , \tag{C.10}$$

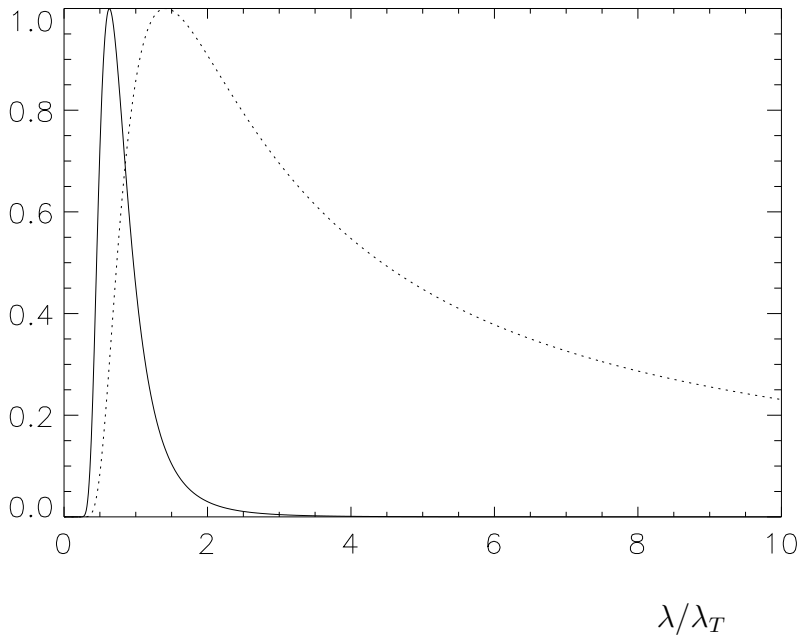

Figure C.1: The functions $\psi(\lambda)/\psi_{max}$ (full line) and $\Pi(\lambda)/\Pi_{max}$ (dashed line) as a function of λ in units of λ_T.

where $\Pi(\lambda) = \psi(\lambda)\Xi(\lambda)\lambda^3$. It follows from equation (C.10) that, when for λ_m the wavelength yielding a maximum in $\Pi(\lambda)$ is chosen, the sum of measuring times of the monochromatic method is always smaller than the measuring time of the time-of-flight method. If $\Xi(\lambda)$ is proportional to λ the maximum of $\Pi(\lambda)$ occurs for $\lambda = \sqrt{2}\lambda_T$. In fig. C.1 both $\psi(\lambda)$ (full line) and $\Pi(\lambda)$ are shown. Note that $\Pi(\lambda)$ is much broader than $\psi(\lambda)$.

In fig. C.2 the ratio t_m/t_t is shown as a function of λ_{min} and λ_{max}. This ratio becomes 1 if λ_{min} and λ_{max} are equal to $\sqrt{2}\lambda_T$. Then the time-of-flight reflectometer is used as a monochromatic beam reflectometer. For a large range of λ_{min} and λ_{max} ($\lambda_{min} \approx \lambda_T$ and $\lambda_{max} \leq 10\lambda_T$) this ratio is larger than 0.5.

This shows that at continuous sources one should carefully consider the possibility of a time-of-flight based instrument, instead of a-priori discard it in favour of a monochromatic instrument. One should keep in mind that both types of reflectometer discussed here are assumed to be ideal. Only resolution losses are taken into account. For instance mostly λ_m can not be taken $\sqrt{2}\lambda_T$, because the filter used to cut-off the higher order Bragg reflections has a larger cut-off wavelength. For the time-of-flight reflectometer the filter for λ_{max} has a transmission less than 1. However, the deviations of the 'real' instruments from the 'ideal' instruments do not significantly influence the comparison made here.

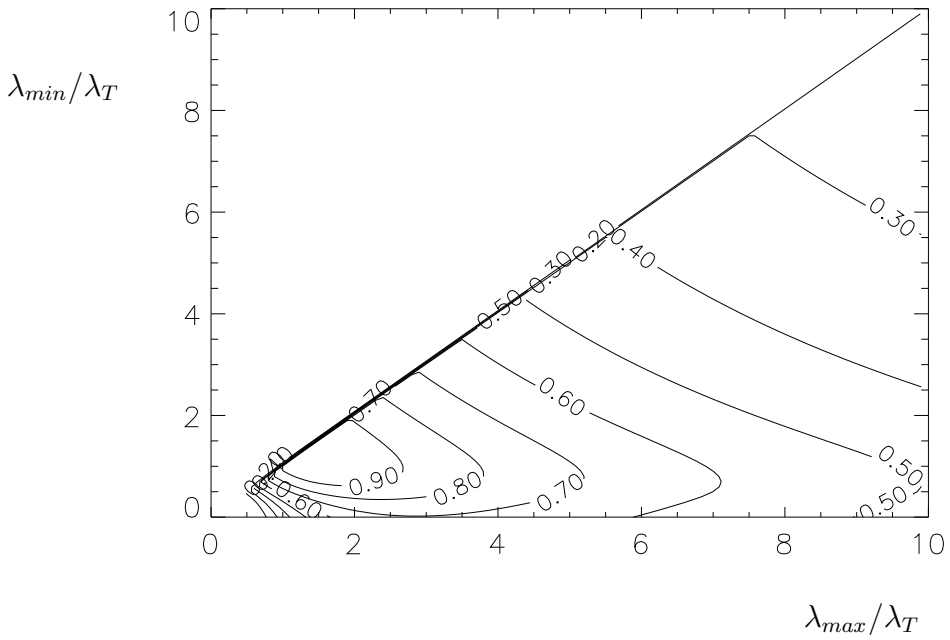

Figure C.2: Ratio of the total measuring time of the monochromatic method to the total measuring time of the time-of-flight method, as a function of λ_{max} and λ_{min} in units of λ_T.

Summary

In the last few years there has been a significant effort in the academic and industrial communities to characterize the behavior of atoms and molecules at surfaces and interfaces. A host of new techniques have been devised. Direct imaging techniques, like electron microscopy, scanning tunneling microscopy and scanning force microscopy, give the local structure at the surface only. Reflection techniques, like ellipsometry, neutron or X-ray reflection are complementary and give global information on the structure of the surface or interface over some depth into the material. This thesis describes the neutron reflection technique, the design, construction and testing of a newly-built neutron reflectometer. The ins and outs of ROG, (acronym of 'Reflectometer voor oppervlakte- en grenslaagonderzoek', Dutch for 'Reflectometer for surface and interfacial studies') and special features, indispensable for the performance, are highlighted.

Although neutron reflectivity is an established technique, there are still some unsolved problems regarding the interpretation of neutron reflectivity data. A principal problem is the inversion of the reflectivity data into the depth-profile. With a normal reflection experiment only the amplitude of the reflection coefficient is measured. If the phase information were available it is in principle possible to calculate the depth-profile. Because of the lack of phase information, this is in principle impossible. Knowledge of the sample and physical restrictions (like the maximum possible scattering length density as occurring in nature) provide extra information and most of the time only one depth-profile will correspond to the data. If these restrictions are not known, or not sufficiently, it is not possible to give a unique depth-profile. It is shown that with a carefully designed experiment it is possible to retrieve the phase information of an unknown layer, from which a unique depth-profile can be calculated. Another problem is caused by the lateral structure of the sample at the interface or surface. Usually the reflectivity is measured in the specular direction. This means that the angle of incidence is equal to the angle of reflection. The lateral structure gives rise to off-specular reflection and a reduction in the specular reflectivity. This reduction depends on the lateral height-height correlation function of the surface.

ROG offers the possibility to measure the off-specular reflectivity. To facilitate this a position-sensitive detector is applied. The basic electronics, the calibration measurements and the method used to reduce the background countrate due to gamma radiation are described.

The discussion on data handling describes the correction procedures for the

measured reflectivity data, calibration measurements and fit procedures. To invert the measured reflectivity data to a scattering length depth profile model a fit procedure is needed. Due to the high non-linearity and the non-unique character of the calculations involved, simple fit procedures using gradient methods are only useful to apply if a solution is (almost) known. A more robust way to find a good set of parameters for a fit is to apply Genetic Algorithms. These and correlations between fit parameters of the model, are discussed.

The report on the investigation performed on ROG of the adsorption of diblock copolymers at the air-water interface elucidates that the neutron reflectivity measurements give quantitative information about the volume fractions of polymer at the interface. The self-consistent field theory is able to describe the adsorption within the statistics of the measurement.

ROG een neutronen reflectometer bij het IRI

door Victor-Otto de Haan

Samenvatting

In de laatste jaren wordt er in de wetenschap en industrie belangrijk onderzoek gedaan om het gedrag van atomen en moleculen aan oppervlakken en grenslagen te karakteriseren. Veel nieuwe technieken zijn ontwikkeld. 'Direct imaging' technieken zoals electronen microscopie, 'scanning tunneling' microscopie en 'scanning force' microscopie bepalen alleen de locale structuur van het oppervlak. Complementair hieraan zijn reflectie technieken zoals ellipsometrie en neutronen- of röntgenreflectie. Hierbij wordt de globale structuur bepaald over een zekere indring diepte in het materiaal. Dit proefschrift beschrijft de neutronenreflectie techniek en het ontwerp, de constructie en het testen van een nieuw gebouwde neutronen reflectometer. De toeters en bellen van de ROG (acroniem van 'Reflectometer voor oppervlakte- en grenslaagonderzoek') en speciale onderdelen noodzakelijk voor de prestaties, worden toegelicht.

Hoewel de neutronen reflectie techniek reeds enige tijd wordt gebruikt, zijn er toch nog een aantal onopgeloste problemen met betrekking tot de interpretatie van de resultaten van neutronenreflectie metingen. Een principieel probleem is de inversie van de reflectiedata naar het diepteprofiel. Bij een normaal reflectie experiment wordt alleen de amplitude van de reflectiecoefficient gemeten. Doordat de fase van de reflectiecoefficient ontbreekt is het in principe onmogelijk om het diepteprofiel uit te rekenen. Kennis van het preparaat en de natuurlijke grenzen (zoals de maximaal voorkomende verstrooiingslengtedichtheid in de natuur) geven extra informatie, zodat meestal slechts één diepteprofiel overeenkomt met de meetgegevens. Het is niet mogelijk om een uniek diepteprofiel te berekenen, indien deze beperkingen onbekend, of onvoldoende bekend, zijn. Indien ook de fase van de reflectiecoefficient bekend zou zijn, kan het diepteprofiel wel worden

uitgerekend. Er wordt aangetoond dat, met behulp van een nauwkeurig uitgevoerd experiment, het mogelijk is om de fase van een onbekende laag te achterhalen, zodat een uniek diepteprofiel kan worden uitgerekend. Een ander probleem wordt veroorzaakt door de laterale structuur van het preparaat aan het grens- of oppervlak. Gewoonlijk wordt de reflectiviteit in de speculaire richting gemeten. Dat betekent dat de invalshoek gelijk is aan de reflectiehoek. De laterale structuur veroorzaakt niet-speculaire reflectie en een reduktie van de speculaire reflectiviteit. Deze reduktie hangt af van de laterale hoogte-hoogte correlatiefunctie van het oppervlak.

ROG geeft de mogelijkheid om de niet-speculaire reflectiviteit te meten. Om dit te realiseren wordt een positiegevoelige detector gebruikt. De basis electronica, de calibratiemetingen en de methode die gebruikt wordt om de achtergrond telsnelheid ten gevolge van gamma straling te reduceren, worden besproken.

De discussie over 'data handling' beschrijft de correctie procedures voor de gemeten reflectiviteitsdata, calibratiemetingen en fitprocedures. Een fitprocedure is nodig voor de inversie van de gemeten reflectiviteitsdata naar een verstrooiingslengtedichtheid diepteprofiel. Door het niet-lineaire en niet-unieke karakter van de betreffende berekeningen zijn simpele fitprocedures, gebaseerd op gradientmethoden, alleen bruikbaar indien de oplossing (bijna) bekend is. Een robustere manier om een goede set van parameters voor een fit te vinden is gebaseerd op Genetische Algoritmes. Deze en de correlatie tussen de fitparameters worden besproken.

Een verslag over het onderzoek uitgevoerd op de ROG naar de adsorptie van diblock copolymeren aan het lucht-water oppervlak verduidelijkt dat neutronenreflectiviteitsmetingen kwantitatieve informatie geven over de aan het oppervlak geadsorbeerde volumefractie polymeer. Met behulp van de 'self-consistent field' theorie kunnen de metingen van de adsorptie binnen de meetnauwkeurigheid worden beschreven.

Acknowledgements

For the realization of this thesis I am indebted to many people who supported or inspired me. I know that without some of them this work would have been impossible and without any of them it would have been different.

Thank you Ad van Well, for having been my boss and powwow. Thank you Leo de Graaf, for being my promotor. Thank you Jan Alberts, for soft-, hard- and mind-ware. Thank you Jan de Blois, for the design of electronic hardware. Thank you Piet van der Ende, for being tidy and more. Thank you Gian Felcher, for our fruitful collaboration. Thank you Henk Fredrikze, for the numerous discussions. Thank you Ard de Graaf, for your valuable contributions to chapter 6. Thank you Christel Messelaar, for calibration samples and friendship. Thank you Martijn Schipper, for design and creation of software. Thank you Ed Osterholt, for the runs. Thank you Hans Perre, for mechanical hardware. Thank you Jurgen de Wolf, for testing motors and chopper. Thank you Jan van der Zanden, for design of mechanical hardware.

Chapter 6 was made possible by fruitful collaboration with the Wageningen Agricultural University. Thank you Henri Bijsterbosch, Frans Leermakers and Martien Cohen Stuart.

Further I would like to thank all my other colleagues, who kept my work lively and amusing. My work here has also been made possible by many people of the institute workforce, for which I thank them.
To my Lord more thank you's than I can ever express are summarized as a citation of the last sentence of these acknowledgements:

> To my Lord more thank you's than I can ever express are summarized as a citation of the last sentence of these acknowledgements:
>
> > To my Lord more thank you's than I can ever express are summarized as a citation of the last sentence of these acknowledgements:
> >
> > > To my Lord more thank you's than I can ever express are summarized as a citation of the last sentence of these acknowledgements:
> > >
> > > > .....
> > > > .....

List of Publications

1. 'Fast sound in a helium-neon mixture determined by neutron scattering', W. Montfrooij, P. Westerhuijs, V.O. de Haan and I.M. de Schepper, Phys. Rev. Lett. **63** (1989) 544.

2. 'Testing a multilayer mirror system in use for polarized neutrons', V.O. de Haan, W.H. Kraan and A.A. van Well, Nucl. Instrum. Methods in Phys. Res. A **289** (1990) 17.

3. 'The avarage number of reflections in a curved neutron guide', A.A. van Well, V.O. de Haan, D.F.R. Mildner, Nucl. Instrum. Methods in Phys. Res. A **309** (1991) 284.

4. 'Stacked neutron guides at IRI, Delft', A.A. van Well, V.O. de Haan and M.Th. Rekveldt, Neutron News **2 no. 3** (1991) 28.

5. 'Performance of an area scintillator detector', V.O. de Haan and A.A. van Well, SPIE **1737** (1992) 264.

6. 'A quasi-elastic neutron scattering study of the ammonium ions in $CsNH_4$-Y zeolite', W.P.J.H. Jacobs, V.O. de Haan, R.A. van Santen and L.A. de Graaf, J. Phys. Chem. **98** (1994) 2180.

7. 'Genetic algorithms used in model finding and fitting for neutron reflection experiments', V.O. de Haan and G.G. Drijkoningen, Physica B **198** (1994) 24.

8. 'ROG, the new neutron reflectometer at IRI, Delft', A.A. van Well, V.O. de Haan and H. Fredrikze, Physica B **198** (1994) 217.

9. 'Comparison between a time-of-flight and a monochromatic neutron reflectometer at a continuous source', V.O. de Haan and A.A. van Well, J. Neutron Research (accepted).

10. 'ROG, the neutron reflectometer at IRI, Delft', V.O. de Haan, J. de Blois, P. van der Ende, H. Fredrikze, A. van der Graaf, M.N. Schipper, A.A. van Well and J. van der Zanden Nucl. Instrum. Methods in Phys. Res. A (accepted).

11. 'On the Retrieval of phase information in Neutron Reflectivity', V.O. de Haan, A.A. van Well, S. Adenwalla and G.P. Felcher, Phys. Rev. B (submitted).

12. 'Adsorption of diblock copolymers at the air-water interface', V.O. de Haan, H.D. Bijsterbosch, M.A. Cohen Stuart, A.W. de Graaf, F.A.M. Leermakers and A.A. van Well (in preparation).

Curriculum Vitae

On August 13, 1965 Victor-Otto de Haan was born in Dordrecht as part of a twin. Highschool (H.A.V.O. '77-'82) was not too hard for him. He studied applied physics at the Dordrecht technical school (H.T.S. '82-'86), finishing with the design and construction of a nitrogen-molecule laser.

After a 'sabbatical year' serving his country as a soldier in Seedorf (B.R.D. '86-'87) he found a job as research assistant at the Interfacultair Reactor Instituut of the Delft University of Technology. In the following three years he studied in the evenings and was rewarded with a masters degree in applied physics (T.U. Delft '87-'91). During this period he took care of the 'spiegel polarimeter' and the 'roterend kristal spectrometer'. These instruments use neutrons to investigate the magnetic or dynamic structure of materials. He also investigated the applications of super-mirror systems used for polarization of neutron beams and as neutron beam filters.

Since March 1991 he is involved in the design, construction and testing of a neutron reflectometer which has been built at IRI. His work and research were supervised by Dr. ir. Ad A. van Well and Prof. dr. ir. Leo A. de Graaf.

Much of his work is described in this thesis, much more is not.